

From pnCCD to pnCCD + CsI(Tl) scintillator: characterizations and applications

DISSERTATION
zur Erlangung des Grades eines Doktors
der Naturwissenschaften

vorgelegt von
M. Sc. Mohammad Mahdi Shokr

eingereicht bei der Naturwissenschaftlich-Technischen Fakultät
der Universität Siegen
Siegen 2019

Gutachter der Dissertation:
Prof. Dr. Ullrich Pietsch
Prof. Dr. Lothar Strüder

Datum der mündlichen Prüfung:
26. Juli 2019

Gedruckt auf alterungsbeständigem holz- und säurefreiem Papier.

Zusammenfassung

Der pnCCD ist ein spezieller Type eines *Charge Coupled Devices* welches für Anwendungen in der Spektroskopie und Abbildungen mit Röntgenstrahlen entwickelt wurde. Er unterscheidet sich von anderen CCD Konzepten durch seine vierdimensionale Datenaufzeichnung: Das Datenvolumen bildet sich in zwei räumlichen, einer Energie und einer Zeitkoordinate ab, die mit einer Wiederholungsrate von bis zu 1000 Bildern/Sekunde, einer hohen Energieauflösung, geringem elektronischen Rauschen und einer exzellenten Quanteneffizienz im weichen Röntgenbereich aufgenommen werden kann. Unter Berücksichtigung dieser Parameter wurde die pnCCD bisher für Einkristall Strukturanalysen im Weichen Röntgenbereich zwischen 5 und 35 keV eingesetzt. In dieser Arbeit demonstrieren wir Ergebnisse von Einzelkornanalysen an polykristalline Proben mittels energiedispersiver Laue Diffraction (EDLD) unter Verwendung von harter Röntgenstrahlung im Energiebereich zwischen 35 und 130 keV. Speziell untersuchten wir das Deformationsverhalten von Einzelkörnern unter Zugbelastung. Zusätzlich zu den vielen Vorteilen der Nutzung der pnCCD für Anwendungen in den Materialwissenschaften erlaubt die Nutzung des Detektors im harten Röntgenbereich die Untersuchung einer großen Zahl von Einzelkörnern, da die harte Röntgenstrahlung tief in das Material eindringen kann. Allerdings ist die Detektion von hochenergetischen Photonen in Silizium basierten Detektoren infolge der geringen Quanteneffizienz in diesem Spektralbereich begrenzt. Dieser Nachteil kann durch die Kombination eines kolumnaren Szintillators mit einem pixillierten pnCCD überwunden werden. In dieser Arbeit berichten wir über die Charakterisierung einer pnCCD im harten Röntgenbereich, die mit einem kolumnaren CsI(Tl) Szintillator verbunden wurde. Die Leistungsfähigkeit des Detektionssystems wurde am Beispiel eines Laue Experiments im Energiebereich zwischen 40 keV und 130 keV getestet. Speziell wurden dazu mehrerer gegeneinander verdrehte GaAs Einkristalle gleichzeitig mit harter Röntgenstrahlung bestrahlt und Lauebilder aufgenommen. Die erste kristallographische Anwendung des neuen Systems erfolgte über eine Kristallstrukturanalyse an einem tetragonalen SrLaAlO₄ Kristall, für den die Gitterkonstanten und die Orientierung der Einheitszelle mit einer Genauigkeit besser als 0.7 % bestimmt werden konnte. Zusätzlich wurden die Strukturfaktoren aus den Intensitäten der Lauespots mit einer Standardabweichung von weniger als 2.5% bestimmt.

Abstract

The pnCCD is a special type of a charge coupled devices developed for spectroscopy and imaging of X-rays. Different from other CCD concepts, pnCCD is a four-dimensional detector, in which the data volume is spanned over two spatial, one energy, and one time coordinates, with fast frame rates up to 1000 images/sec, high energy resolution, low electronic noise and an excellent quantum efficiency at soft X-ray energy range. Considering these parameters, the pnCCD has been used for single crystal structure analysis in the soft X-ray energy range (5-35 keV) so far. In this thesis we demonstrate single grain analysis of a polycrystalline sample by means of an energy-dispersive Laue diffraction (EDLD) using white X-ray radiation in the hard energy range (35-130 keV). In particular we investigate the deformation behavior of individual grains under tensile loading. In addition to many other advantages of the pnCCD in material science applications, the use of hard X-ray radiation penetrates deeply inside the samples and examine a largest possible number of grains within the specimen. However, the detection of the high energetic photons by silicon-based detectors is limited by the detector quantum efficiency. This drawback can be overcome by combining a columnar scintillator with a pixelated silicon-based pnCCD detector. In this thesis we report on the characterization of a low noise, fully depleted pnCCD coupled to a columnar structure CsI(Tl) scintillator in hard X-ray range. The performance of the detection system in the energy range between 40 keV to 130 keV was tested by means of a Laue type X-ray diffraction experiment. Realized at the EDDI beamline of the BESSY II synchrotron we recorded Laue pattern of a set of several GaAs single crystals irradiated by white synchrotron radiation. The first application of this new system in crystallography is demonstrated by a crystal structure analysis of a tetragonal SrLaAlO₄ crystal in which the lattice parameters and the cell orientation has been determined with an accuracy better than 0.7%. In addition, the structure factors moduli have been determined from the intensities of the Laue spots with a standard deviation of less than 2.5%.

Table of Contents

1	Introduction	8
2	Concept of solid state radiation detectors	12
2.1	Interaction of X-rays with matter	12
2.2	Attenuation coefficients of Si and CsI	15
2.3	Solid state detectors	17
2.3.1	Semiconductor radiation detectors	18
2.3.2	Pn-junction	20
2.3.3	Scintillators	24
2.4	Detection of the Scintillation Light	31
3	PnCCD detector	36
3.1	Concept and structure of PnCCD	36
3.2	Quantum efficiency	39
3.3	Read out	42
3.3.1	Generation of charges and collection	42
3.3.2	Frame store	44

3.3.3	Charge transfer process	46
3.3.4	Signal amplification and readout electronics	47
3.4	Spatial resolution	49
3.5	Energy resolution	51
3.6	Time resolution	52
4	Application of pnCCD in material science: single grain analysis of polycrystalline nickel	54
4.1	Energy-dispersive Laue diffraction	56
4.2	Indexation and grains identification	61
4.3	Determination of grain orientation and Schmid factor	64
4.4	Grain selective structural changes under a tensile load	67
4.5	Discussion	73
5	PnCCD coupled to CsI(Tl) scintillator	75
5.1	Spectroscopic imaging of hard X-rays	75
5.2	Configuration of the combined system and the detection process	77
5.3	Laue Diffraction Experiment	79
5.4	Detection and conversion efficiency of X-rays in Si and CsI(Tl)	80

5.5	Energy resolution for direct and indirect events	84
5.6	Potential of pnCCD + CsI(Tl) for hard X-ray structure analysis	87
6	Structure analysis of SrLaAlO₄ by means of EDLD using ultra-high X-ray radiation	94
6.1	Experiment setup and data collection	95
6.2	Spectral analysis	97
6.3	Calculation of lattice parameters	99
6.4	Structure factors	103
7	Summary and Conclusions	106
	Bibliography	109
	Acknowledgments	120

1 Introduction

At modern synchrotron radiation facilities, there is an increasing demand for experiments in hard X-ray energy range. For example, the use of hard X-rays for Laue diffraction experiments profits from the fact that the part of the Ewald sphere cutting by the detection plane is rather flat, accessing a large reciprocal-space volume simultaneous [1, 2]. In this way, the number of Laue spots to be collected by the relatively small pnCCD detector area is significantly enhanced compared to previous experiments performed with soft X-ray radiation. Furthermore, hard X-ray radiation has the ability to penetrate deeply into the investigated sample as well as it generates less radiation damage in materials due to the lower photoelectric interaction [3]. Using ultra-high X-ray energy in an energy-dispersive Laue diffraction experiment (EDLD) has helped to elucidate the structure and mechanics of polycrystalline solids in the context of a wide range of problems. Using pnCCD, Abboud et al. 2017 [4] has calculated the deviatoric and hydrostatic components of the elastic strain and stress tensors in a copper sample after probing it using microbeam and a single shot exposure. Philips et al. [5] have investigated the stress distribution in a polycrystalline Aluminum film on a Si substrate during cyclic thermal loading. The presence of a stress gradient from the whisker root to the Sn parent material that drives the whisker growth has been confirmed by Choi et al [6].

In EDLD, variations in the spot shape can be observed during plastic deformation. While a sharp Bragg spots with Gaussian distribution can be observed for a perfect crystal, a streaking of these spots can be observed when a strain is applied. This streaking is related to the presence of net lattice mis-orientation and curvature in the scattering volume, which, in turn, has been linked to the evolution of geometric necessary dislocations (GND) [7, 8]. Using monochromatic beams one is able to map the lattice response and the deformation of ductile polycrystalline material under an external load with high angular resolution. Laue diffraction with white micro-beams provides a powerful and efficient tool for the study of intra- and intergranular lattice distortions at the microscale. Three dimensional spatially resolved polychromatic X-ray diffraction can resolve the local crystal structure of deformed polycrystalline and other complex material systems [9]. As example of this capability we show in chapter 4 of this thesis a study of the deformation behavior

of individual grains in a polycrystalline Nickel wire under tensile loading by means of EDLD. 38 Laue spots have been identified in the Laue pattern which originate from 9 individual grains. The simultaneous measurement of the Laue spots position and energy allows for tracking the evolution of the 9 grains through multiple stages of deformation. Angular and spectral elongation (streaking) of the Laue spots increases as tensile loading is increased and is attributed to macroscopic changes in texture and strain due to defect accumulation. On the single grain level, a correlation between crystallographic orientation and strain has been found. Moreover, within a single grain a spatially resolved anisotropic deformation is measured with increasing amount at the grain boundaries. Comparison of the grain specific responses allows for the development of a deformation scenario for the whole specimen. The presented experiment demonstrates an alternative protocol for the investigation of deformation mechanisms in polycrystalline materials using a white hard X-ray beam and a 2D energy dispersive detector (2DED).

However, the low quantum efficiency (QE) of silicon at high energies limits the use of silicon based charged coupled devices for applications that require ultra-hard X-rays. While the photo attenuation at low photon energies ($E < 55$ keV) is dominated by photoelectric effect the most dominated process at higher energies is Compton scattering. Therefore, the development of new detectors or extension of present detectors has high priority. This needs to consider additional physical effects. One way of improvement is the coupling of a columnar structured CsI(Tl) scintillator to the pnCCD improving the QE of the system to a value of around 50% at 100 keV instead of 1% for the naked pnCCD [10].

In chapter 5 we will show the characterization of a combined system which has been developed by PNSensor GmbH in Munich. A micro-columnar Thallium doped Caesium Iodide (CsI(Tl)) scintillator with an area of $12 \times 12 \times 0.7$ mm³ and a density of 4.5 g/cm³ was attached to the back side of a 0.45 mm thick pnCCD with 128×128 pixels and a pixel size of 75×75 μm². The CsI(Tl) is coupled to the pnCCD with a 50 μm thin silicone protection pad covered with optical grease. Using front-illuminated geometry (pixelated side) the low energetic photons (below 10 keV) are absorbed nearly completely by the pnCCD as the QE of Si in this energy range is close to 100%. This type of detection is denoted by “direct detection”. As the incident photons energy is above 10 keV the QE of the silicon in the pnCCD decreases and hence more photons can traverse the Si chip and reach the CsI(Tl) scintillator at the backside. The stopping power of the scintillator material is

close to 100% at energy up to 40 keV, 90% at 60 keV and 50% at 100 keV [11,12]. The interaction between the X-ray photons and the scintillator results in the generation of optical photons where 90% of them are back reflected and absorbed by the pnCCD. This detection process is denoted by “indirect detection”. The spectroscopic performance of pnCCD in combination with scintillator in the hard X-ray range was tested by means of energy dispersive Laue diffraction experiment. It will be shown that the energy resolution of the directly detected Laue peaks with energies ranging between 40 and 90 keV is in the order of 0.7% and 0.9% while the energy resolution of the indirect detection of these peaks is between of 16.5% and 18.5% [13]. But the high quantum efficiency of the combined system leads to a highly accurate X-ray structure analysis compared to the bare pnCCD. It will be shown that the error in the calculation of the Bragg peak intensity is in the order of 1.5% when its evolution is based on the indirect peak in contrast to an average error of 30% if one make use of the direct detection of the peaks. Such large difference in the accuracy was expected due to the high statistics of the high energetic photons detected indirectly with the help of the highly efficient scintillator in contrast to the poor statistics of the directly detected photons.

As an application in crystallography, the combined system has been utilized for X-ray structure analysis of a SrLaAlO₄ crystal by means of an EDLD experiment in the energy range between 40 and 130 keV. Exploiting the achieved high quantum efficiency of this combined detection system for hard X-rays a large number of Bragg reflections could be recorded by the relatively small detector area allowing for accurate and fast determination of the crystal structure. The experiment was performed at the energy-dispersive diffraction (EDDI) beamline of BESSY II synchrotron using a pnCCD with 128x128 pixels. Since the Laue peak energies and peak positions can be recorded simultaneously by the system, the tetragonal structure of the investigated specimen was determined without any prior information. The lattice parameters and the unit cell orientation were evaluated with an accuracy of better than 0.7%. As a result of the accurate calculations of the Laue spots intensities the structure factor moduli have been calculated with a standard deviation between 0.9% and 2.5% for all Bragg reflections recorded in the energy range between 40 and 130 keV. The obtained results demonstrate the potential of pnCCD + CsI(Tl) detector system and make it favorable for structure analysis in the hard X-ray range.

It's worth mentioning that chapters 4 to 6 are based on recent publications as following:

- Chapter 4 based on: *shokr et al., 2019*, In situ observations of single grain behavior during plastic deformation in polycrystalline Ni using EDLD. *submitted*.
- Chapter 5 based on: *shokr et al., 2017*, Applications of a pnCCD detector coupled to columnar structure CsI(Tl) scintillator system in ultra-high energy X-ray Laue diffraction. *Journal of Instrumentation*.
- Chapter 6 based on: *shokr et al., 2019*, Structure analysis of SrLaAlO₄ crystal by means of EDLD using ultra-hard X-ray synchrotron radiation with pnCCD detector coupled to CsI(Tl) scintillator. *Journal of Synchrotron Radiation*.

2 Concept of solid state radiation detectors

In this chapter the physical background of solid state detectors like silicon drift detectors SSDs and charge coupled device CCDs will be demonstrated. Since the interaction between photons and matter is the fundamental notion behind the detection process, we will show the different types of interactions of X-rays in the energy range $E = [1-150 \text{ keV}]$, the range utilized in the following chapters, with Si and CsI(Tl) as well as interaction between visible light $E = [1.6-3.5 \text{ eV}]$ and Si. Only the essential phenomenological and mathematical description of photon interactions that are needed in this work will be discussed while the details one can read in standard literature such as [14], [15] and [16].

2.1 Interaction of X-rays with matter

The most important quantity characterizing the penetration and diffusion of X-rays radiation in extended media is the probability per unit path length that a photon will interact with the medium which is commonly known as the attenuation coefficient, μ . This quantity depends on the photon energy E and on the atomic number Z of the medium. When the atom is exposed to radiation in the energy range $1 \sim 1000 \text{ keV}$, two types of interactions can occur: the photoelectric absorption and the Compton Scattering. At higher energy $E > 1022 \text{ keV}$, a pair production process can take place. However, such energy level is out of our interesting range in this thesis. For Si, the photoelectric process dominates at energy $E < 55 \text{ keV}$. As the energy increases the main contribution to the attenuation coefficient comes from Compton scattering.

- **Photoelectric effect:** When the incident photon energy E is larger than the binding energies B_e of atomic electrons, photons can be completely absorbed by the atom, accompanied with ejection of an electron raised into a state of the continuous spectrum. This process is called photoelectric effect. The ejected electron is emitted with a kinetic energy equal to the difference between the incident photon energy and the binding energy of the electron:

$$K_e = E - B_e \quad (2.1)$$

In the non-relativistic region, the Born approximation can be used to calculate the K-shell total photoelectric cross section for incoming photon-energies larger than the binding energy of the K-shell electrons:

$$\sigma_{ph} = \sigma_{th} 4\sqrt{2} \frac{Z^5}{137^4} \left(\frac{m_e c^2}{E} \right)^{7/2}, \quad (2.2)$$

Where σ_{th} is the classical Thomson scattering cross section, with r_e the electron radius. m_e is the electron mass, c the velocity of light, Z the atomic number [17, 18]. For heavy elements or for incoming photon energies close to those of absorption edges, the Born approximation is no longer valid and exact wave functions must be used [19].

- **Compton effect:** When the incident photon energy E is much larger than the binding energy of the K-shell electron B_e such that the ratio B_e / E can be neglected, Compton scattering becomes the dominant process. The Compton effect is an incoherent scattering process based on the corpuscular behaviour of the incident photons on individual atomic electrons. In this process the binding energies of these electrons do not affect the interaction and can be neglected in calculations. Furthermore, it is considered as an inelastic process, although the kinematic description of the reaction is that of an elastic collision. This effect has been observed for the first time by Compton (1922), who provided its theoretical explanation. When the incoming photon with energy E is scattered by a quasi-free electron, it emerges at an angle θ with energy E' :

$$E' = \frac{E}{1 + \epsilon(1 - \cos \theta)}, \quad (2.3)$$

with $\epsilon = \frac{E}{mc^2}$. The Compton electron recoils at an angle θ' with energy $E'_e = E - E'$ that may adapt any value between 0 and the so-called Compton edge, the backscattering energy. As a result of secondary interactions with other atoms, for both the Compton electrons and the scattered photons, a continuous energy spectrum is measured within the detector.

The cross section for Compton scattering of a photon interacting on a quasi-free electron is given by Klein-Nishina equation:

$$\sigma_{c,e} = 2\pi r_e^2 \left\{ \left[\frac{1+\epsilon}{\epsilon^2} \right] \left[2 \frac{(1+\epsilon)}{1+2\epsilon} - \frac{\ln(1+2\epsilon)}{\epsilon} \right] + \frac{\ln(1+2\epsilon)}{2\epsilon} - \frac{1+3\epsilon}{(1+2\epsilon)^2} \right\}. \quad (2.4)$$

The Compton scattering cross section per atom can be obtained by multiplying equation (2.4) by the atomic number, Z , i.e:

$$\sigma_c = Z \cdot \sigma_{c,e}. \quad (2.5)$$

For low X-ray energies ($\epsilon \ll 1$), σ_c can be expanded to [20]:

$$Z\sigma_{th} \left(1 - 2\epsilon + \frac{26}{5}\epsilon^2 \dots \right). \quad (2.6)$$

As the photoelectric and Compton effects are the only processes occurring in energy range mentioned above, the total cross section for a photon interacting with matter is:

$$\sigma = \sigma_{ph} + \sigma_c \quad (2.7)$$

2.2 Attenuation coefficients of Si and CsI(Tl)

The mass attenuation and mass energy-absorption coefficients are extensively used in calculations for X-ray transport in matter and for photon energy depositions in materials. The energy and Z -dependence of the mass absorption coefficients, (μ/ρ) , are mainly determined by the total cross section given in equation (2.7) and it is expressed by:

$$\frac{\mu}{\rho} = \frac{N_A \sigma}{M} [cm^2/g] \quad (2.8)$$

with μ is the linear absorption coefficient with a unit cm^{-1} and ρ is the density of the material. N_A is the Avogadro number and M the molar weight. For compounds and mixtures like CsI, the total mass absorption coefficient is:

$$\frac{\mu}{\rho} = \sum_i W_i \left(\frac{\mu}{\rho}\right)_i \quad (2.9)$$

where W_i is the weight fraction and $\left(\frac{\mu}{\rho}\right)_i$ the mass absorption coefficient of each element in the compound [21]. As can be seen from equations (2.2), (2.5) and (2.8), elements with high atomic number, Z , and high density, ρ , have high stopping power for X-rays. Such elements are favourable for detectors materials.

Fig. 2.1 shows the mass absorption coefficient of Si and CsI in term of incident photons energy in the range between 1 and 200 keV. The values in the plots were obtained using the web database

XCOM [22]. This database provides photon cross sections for scattering, photoelectric absorption and pair production, as well as total attenuation coefficients, for any element, compound or mixture ($Z \leq 100$), at energies from 1 keV to 100 GeV.

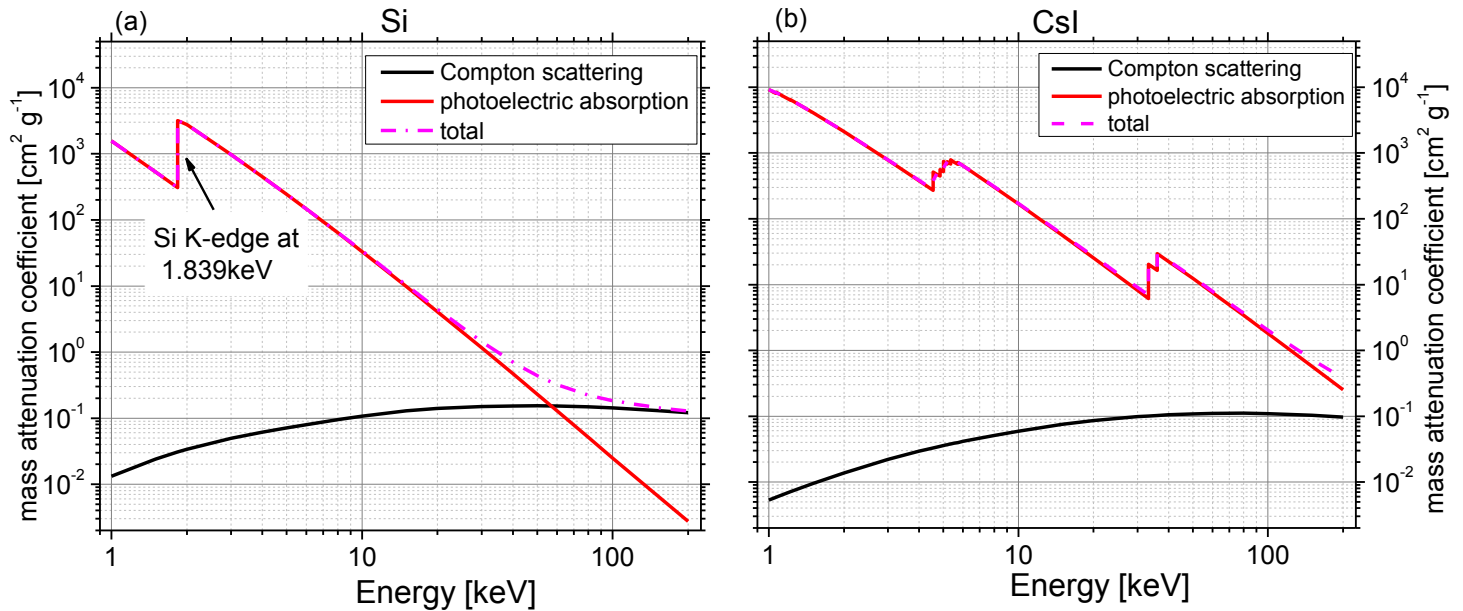


Figure 2.1: Mass attenuation coefficient for (a) Si and (b) CsI as a function of the incoming photon energy in the range [1, 200] keV. At 100 keV the photo attenuation coefficient for CsI is higher by more than 100 times than that for Si.

As can be seen in fig. 2.1(a), below 55 keV, the photoelectric effect is the dominant interaction in Si. The strong decay of the mass absorption coefficient above the Si K-absorption edge at 1839 eV entails limitations in detection capabilities of hard X-rays. At an energy of 55 keV, the probability of photoelectric effect equals the probability of Compton scattering. Towards 200 keV, the total absorption cross section of Si is mainly determined by Compton scattering.

CsI material contains high Z elements ($Z=53$ for I and $Z=55$ for Cs), and this leads, as discussed along this section, to high absorption coefficients comparable to Si ($Z=14$). Unlike the Si case, the photoelectric effect in CsI is the main contributor to the total attenuation coefficient in the whole range between 1 and 200 keV (fig. 2.1(b)). The jumps in the mass attenuation coefficient curve of CsI in fig. 2.1(b) refer to the L-edges of I and Cs between 4.55 and 5.72 keV and K-edges between 33 and 36 keV.

A beam of photons with energy E and intensity I_0 traversing an absorber with thickness x exhibits a characteristic exponential reduction of the number of its own photons such that each photon is individually removed from the incoming beam with a probability given by the cross section of the interactions shown above. In the passage through a differential thickness dx of a medium, the number of removed photons $-dI$ per unit of time is proportional to the photon beam intensity I' at depth x' and to the number of target atoms per unit of volume n_A of the traversed material, i.e.,

$$-dI = I' n_A \sigma dx', \quad (2.10)$$

where the term $n_A \sigma dx'$ is the probability for a photon removal in the thickness dx' with $n_A \sigma = \mu$ the linear attenuation coefficient in (2.8). Consequently:

$$\frac{dI}{I'} = -\mu dx' \Rightarrow \ln \frac{I}{I_0} = -\mu x, \quad (2.11)$$

hence, the attenuated intensity after traversing the absorber with thickness x is given by:

$$I = I_0 e^{-\mu x} \quad (2.12)$$

2.3 Solid state detectors

Solid state detectors SSDs are typically formed from semiconductor materials exploiting their small energy gap between their valence and conduction bands. Therefore, a small energy deposition can move electrons from the valence band to the conduction band, leaving holes behind. Applying an external electric field, the electrons can drift and produce a signal proportional to the number of the generated electrons. Therefore, the passage of an ionizing particle can be detected by collecting all the charge carriers liberated by the energy deposition in the semiconductor.

Besides commonly used elements of the carbon group with four valence electrons like Si and Ge, special III-V and II-VI compounds like GaAs or CdTe have been tested [23, 24]. In comparison to gas detectors and scintillators, semiconductor detectors provide a larger ionization yield in the X-ray regime. Additionally, with respect to the significantly higher mass density of solids compared to gases, semiconductor X-ray detectors can be fabricated in the form of compact systems with relatively small volumes.

In gas detectors the ionization of gas molecules by incident X-rays created by electron-ion pair production gives rise to measurable output signals. For typical gases, the energy required to create an electron-ion pair is in the range of 30 eV [25]. Electronic excitations of heavy atoms takes place in scintillation counters due to the deposition of X-ray energy. As a following process scintillation photons are emitted in the optical spectral regime when these atoms return back to their electronic ground state. These optical photons can be recorded by means of photomultipliers. Crystalline solids like (NaI(Tl), CsI(Tl)) and organic liquids have been used as standard materials for scintillators. In the case of CsI(Tl), an optical yield of 52 optical photons per 1 keV of deposited energy is obtained [20]. Due to their high attenuation coefficients in comparison to the standard semiconductors at high incident energies, proportional counters and scintillation counters are also suitable detector systems for gamma spectroscopy.

2.3.1 Semiconductor radiation detectors

The principle of semiconductor detectors is based on the small energy gap between the valance and the conduction bands. In the case of silicon, the gap energy is $E_g = 1.12$ eV at room temperature ($T = 300$ K) rising up to 1.17 eV as $T \rightarrow 0$ K [26]. The necessary gain in energy can be either thermally induced or caused by an X-ray interaction. For this reason, semiconductor radiation detectors are usually cooled down below room temperature in order to avoid the so-called thermal noise caused by the unwanted contribution to the current generated by thermal excitation of electrons. Once a X-ray photon is absorbed by photoelectric effect within the semiconductor, the photon energy transfers to a single electron. The remaining kinetic energy of the liberated electron as well as the emitted fluorescence energy are then available for the excitation of other electrons by means of secondary interaction processes, predominantly electron-electron collisions.

In case of indirect band gap materials like silicon (fig. 2.2), the minimum energy of the conduction band in k-space does not coincide at the momentum of the maximum energy of the valence band. This means that for an electron to be promoted to the conduction band, a phonon must also be created to conserve the momentum. Hence, the average energy required to generate one electron-hole pair (exciton) in Si is larger than E_g and it is equal to 3.67 eV at room temperature and 3.73 eV at $T = 10$ K [31].

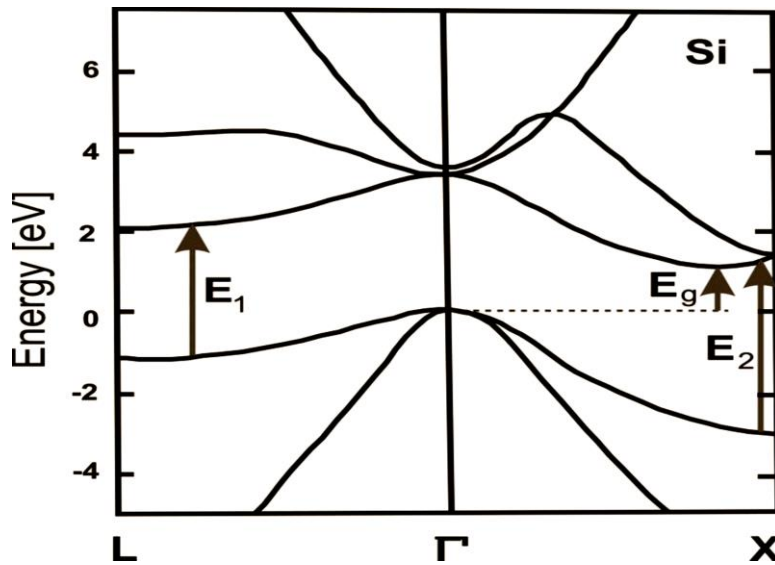


Figure 2.2: Bandscheme of silicon. [30]

The positive charge carriers (holes) formed in the valence band move in a direction opposite to that of electrons in the conduction band. That means, the current of the holes is the counterpart of electrons current. In order to avoid recombination of electrons and holes, the charges are separated from each other by means of an externally applied electric field, E , in which the electrons and holes are drifting through the semiconductor opposite to each other with velocity

$$v_e = \mu_e E , \quad (2.13)$$

for electrons, and

$$v_h = \mu_h E , \quad (2.14)$$

for holes. μ_e and μ_h are the electron and hole mobility, respectively. In silicon, $\mu_e = 1350 \text{ cm}^2\text{V}^{-1}\text{s}^{-1}$ and $\mu_h = 450 \text{ cm}^2\text{V}^{-1}\text{s}^{-1}$ [27]. The high mobility of electrons in Si leads to a charge collection times in the order of 10 ns for typical detector geometries and electric field strengths in the range of 1 kV cm^{-1} .

2.3.2 Pn-junction

The n-type and p-type conductivity semiconductors are semiconductors with an excess of electrons and holes, respectively, resulting from the introduction of electrically active donor and acceptor impurity atoms. The product of concentrations of electrons n and holes p is equal to the square of the intrinsic carrier concentration, n_{ins} , which is constant for a given semiconductor at a given temperature T :

$$np = n_{int}^2 . \quad (2.15)$$

For silicon, the temperature dependence of n_{ins} is given by [28]:

$$n_{ins} \approx 4.1056 \times 10^{21} \times (k_B T)^{3/2} e^{-E_g/2k_B T} , \quad (2.16)$$

where $E_g = 1.12$ eV as defined above is the energy gap in silicon, $k_B = 8.617 \times 10^{-5}$ eV/K is the Boltzmann constant and T is the temperature in Kelvin. At $T = 300$ K, $n_{ins} \approx 1.45 \times 10^{10} \text{ cm}^{-3}$.

When an n-type semiconductor is set in a spatial contact with a p-type semiconductor, a so-called p-n junction is formed (fig. 2.3 (a)). In practice, such a junction is built by diffusing holes into an n-type silicon crystal and electrons into a p-type silicon crystal remaining ionized acceptors and donors in the p- and n-type materials. A pn-junction results from the equilibrium of the diffusion current and the drift current where the later one is originated by the electric field between ionized acceptors and donors.

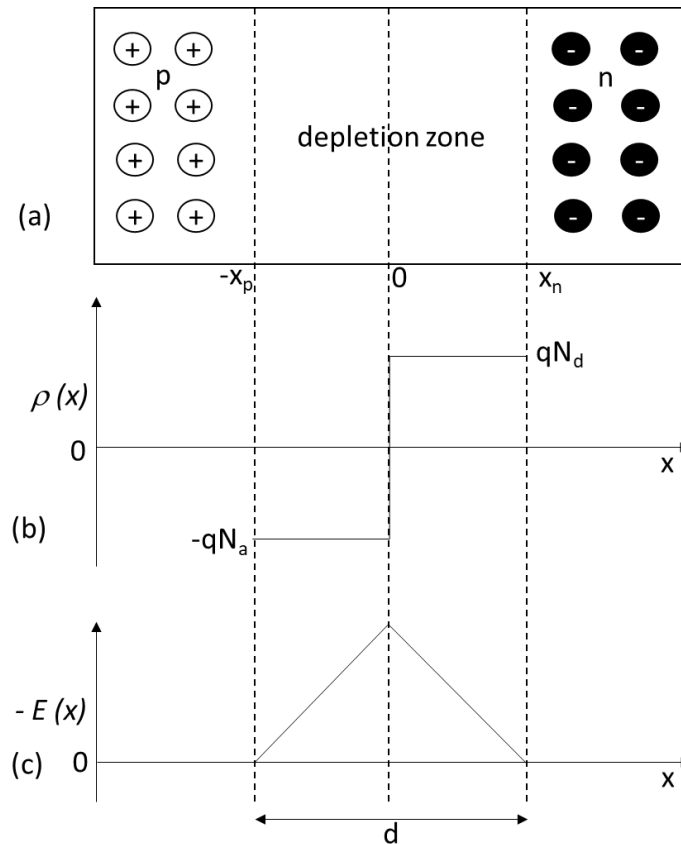


Figure 2.3: Schematic representation of a pn – junction. The applied bias voltage V_b creates a depletion depth d . (a) represents the junction, (b) the charge distribution $\rho(x)$ and (c) the electric field $E(x)$

As result a charge depleted region is created at the interface between the p- and n-type regions. Since diffusion is the motion of carriers from regions of high charge density to regions of low density, it is responsible for the existence of a space-charge region with two zones, one zone made of filled electron acceptor sites not compensated by holes and other zone made of positively charged empty donor sites not compensated by electrons. If, for instance, the density of donors in the n-type region is much higher than acceptors in the p-type region, the space-charge region extends much deeper into the p-region than into the n+-region. The net result is the formation of a space-charge region with acceptor centers in the p-region, filled with donor electrons from the n-region and not compensated by holes. This space-charge region is called the *depletion region*. The charge density $\rho(x)$ in the depletion area is given by:

$$\rho(x) = \begin{cases} -qN_a & \text{for } -x_p \leq x \leq 0 \\ qN_d & \text{for } 0 \leq x \leq x_n \end{cases} \quad (2.17)$$

where x_p and x_n are the depletion length on *p*-side and *n*-side, respectively, as shown in fig. 2.3. N_a and N_d are the acceptors (*p*-type region) and donor (*n*-type region) impurity concentrations on each side of the junction, respectively. The charge density is zero outside the depletion region (fig. 2.3 (b)). As $N_a x_p = N_d x_n$, the net total charge in the depletion area vanishes.

The electric field E resulting from the charges separation is a function of the depth inside the depletion zone such that:

$$E(x) = \begin{cases} E_n(x) = q(N_d/\epsilon)(x - x_n) & \text{for } 0 \leq x \leq x_n \\ E_p(x) = -q(N_a/\epsilon)(x + x_p) & \text{for } -x_p \leq x \leq 0 \end{cases} \quad (2.18)$$

where ε electric permittivity. Consequently, the built-in voltage V_0 can be obtained by integration of the electric field E over the depletion layer [29]:

$$V_0 = - \int_{-x_p}^{x_n} E(x) dx = \frac{k_B T}{q} \left(\frac{N_a N_d}{n_{int}^2} \right). \quad (2.19)$$

As soon as the built-in voltage is determined, the depth of the depletion zone, d_0 , can be obtained:

$$d_0 = \sqrt{\frac{2\varepsilon V_0}{q} \left(\frac{1}{N_a} + \frac{1}{N_d} \right)}. \quad (2.20)$$

However, d_0 is typically in the order of a few microns which limits the capability of the pn-junction for particle detection. Therefore, an external voltage, V_b , has to be applied between the n and p regions such that $-V_b < 0$ on the p-side of the junction and hence equation (2.20) becomes [29]:

$$d = \sqrt{\frac{2\varepsilon(V_0 + V_b)}{q} \left(\frac{1}{N_a} + \frac{1}{N_d} \right)}, \quad (2.21)$$

which gives rise to a relatively thick depletion layer that can serve as sensitive volume for incident X-rays in semiconductor radiation detectors. If the polarity of the external voltage V_b is reversed so that it is applied contrary to V_0 , the electric field within the depletion layer drops and a current flow across the pn-junction becomes possible. In this case, the diode is forward-biased.

Typically, energy-dispersive point detectors used for X-ray diffraction experiments in the white-beam mode are realized as diodes with reverse-biasing. Moreover, the pn-junction is the basic component of a pnCCD detector and its amplifying on-chip electronics is formed by special arrangements of field effect transistors (FET). More details about pnCCD structure will be discussed in the next chapter.

2.3.3 Scintillators

Scintillators are materials in which large fractions of incident striking particles or radiation are absorbed and transformed into detectable visible or near visible light photons, later converted into an electric signal. They are used in many applications especially those require high energetic particles or hard X-rays that are not directly detectable by semiconductor detectors.

Depending on the forming material and light emission mechanism, there are two different types of scintillators, organic and inorganic [32]. While organic scintillators are aromatic hydrocarbon compounds containing a benzenic cycle like anthracene ($C_{14}H_{10}$) and naphthalene ($C_{10}H_8$) [33], inorganic scintillators are ionic crystals doped or not with an activator such as NaI(Tl), CsI(Tl), $Bi_4Ge_3O_{12}$ and BaF_2 [34]. The mechanism of light emission in organic scintillators, is a molecular effect. It proceeds by excitation of molecular levels in a primary fluorescent material, in which during de-excitation, bands of ultraviolet (UV) light is emitted. This UV light is absorbed in most organic materials with an absorption length of a few mm. A wavelength shifter formed by a second fluorescent material is then required to convert the UV light into visible light. The wavelength of the emitted light is a characteristic of the activator and it is possible to modify the final wavelength by varying the activator.

Rather than the molecular effect, the mechanism of inorganic scintillators is a lattice effect. The electrons in the valence band are bound at the lattice sites, while those in the conduction band are free to move throughout the crystal. If the incoming radiation transfers sufficient energy to the electrons in the valence band to move into the conduction band (leaving holes in the valence band), the passage of a charged particle through the crystal may ionize the crystal. If the incoming energy is not sufficient, the electron of the valence band will not reach the conduction band and will form a bound state, called exciton, with the hole. The excitons are located below the conduction band

in so-called exciton band (fig. 2.4). Finally, the passage of charged particle through the scintillator medium generates a large number of free electrons, free holes and electron-hole pairs which move around in the crystal lattice until they reach an activator center that exists in the scintillator and occupy energy levels in the gap between the conduction and valence bands. They then transform the activation center into an excited state. The subsequent decay of this excited state to the activator center ground state produces emission of light.

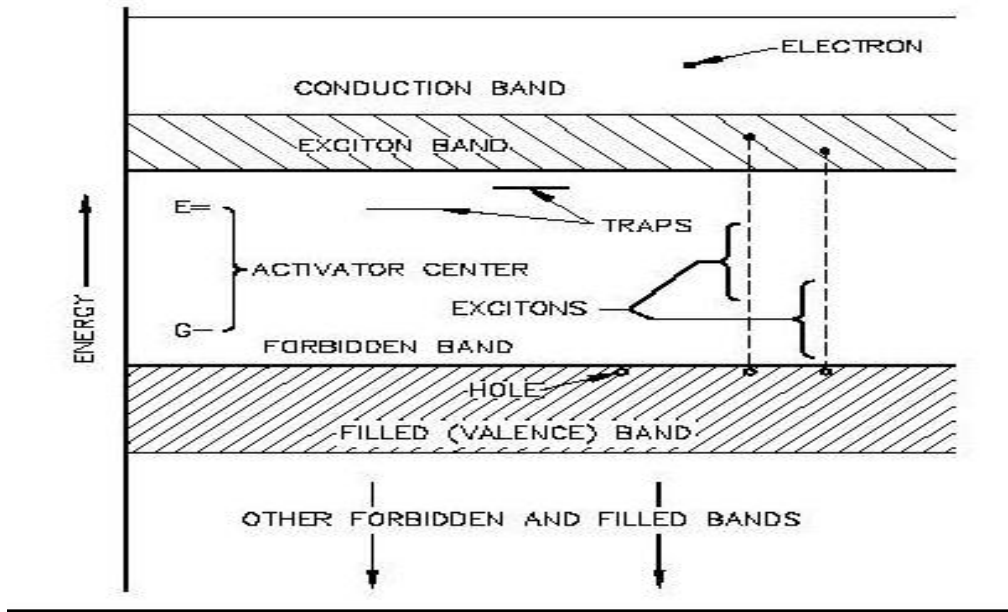


Figure 2.4: Electronic Energy Band of an ionic (inorganic) scintillator doped with an activator.

In comparison to organic scintillators, inorganic scintillators have high density and high atomic number giving rise for high absorption of charged heavy particles, γ and X-rays. In addition, for moderate resolution requirements, plastic scintillators are adequate, for which energy resolutions of the order of 1% have been obtained for light particles of about 100 MeV energy [35]. NaI(Tl) and CsI(Tl) are the most commonly used inorganic scintillators with radiation detectors and they usually contain about 0.1% of Tl as activator. Because the color of the emitted light (table 2.1) is well matched to the spectral sensitivity of silicon photodiodes, which show excellent long term stability, CsI(Tl) is widely used for detecting both light charged particles and gamma rays and is

also used in this thesis. Excellent energy resolution has been reported for relatively small detectors using CsI crystals [36-38], as well as a good energy resolution for selected larger detectors [39].

<i>Properties</i>	<i>CsI(Tl)</i>	<i>NaI(Tl)</i>
<i>Density [g/cm³]</i>	4.53	3.67
<i>Short decay time [ns]</i>	>1000	230
<i>Long decay time</i>	>200 [ms]	150 [ms]
<i>Peak emission [nm]</i>	550	415
<i>Refractive index</i>	1.8	1.85
<i>Light yield [photon/MeV]</i>	5 x 10 ⁴	4 x 10 ⁴

Table 2.1: properties of the inorganic scintillators, CsI(Tl) and NaI(Tl). [41]

Particle detectors using NaI(Tl) scintillators have a number of disadvantages. Since the crystal is hygroscopic such detectors may deteriorate with time when they are not hermetically sealed or if they are stored in air. The use of thick entrance windows for well sealing of the detectors leads to higher detection thresholds and a loss of resolution. The detectors usually employ photomultipliers for photon detection. However, they exhibit poor long term stability when operating in vacuum. Despite the possibility to monitor gain drifts with high accuracies, the procedures used are rather time consuming. In contrast, CsI(Tl) scintillators promise to overcome some of the difficulties shown above. They have superior thermal and mechanical properties. Since they are only slightly hygroscopic they do not have to be hermetically sealed. Furthermore, their spectral response is well matched to that of silicon photodiodes [40].

Scintillators are characterized by their scintillation efficiency, R_s , scintillation yield, R_r , and photoelectric efficiency, R_{pe} . The scintillation efficiency is the ratio of the average number of emitted photons $\langle N_{ph} \rangle$ to the energy E_i of the incident radiation absorbed by the scintillator:

$$R_s = \frac{\langle N_{ph} \rangle}{E_i}. \quad (2.22)$$

The scintillation yield is defined as the ratio of the total energy of the emitted light, $\langle N_{ph} \rangle h\nu$, to the incident energy, E_i :

$$R_r = \frac{\langle N_{ph} \rangle h\nu}{E_i} = R_s h\nu. \quad (2.23)$$

The ratio of the number of the incident radiation (e.g. X-rays) that have been absorbed by the material, N_{ab} to the total number of photons that have been detected, N_{det} is defined as the photoelectric efficiency:

$$R_{pe} = \frac{N_{ab}}{N_{det}}. \quad (2.24)$$

R_{pe} is maximal for X-rays of energy lower than 100 keV, where the interactions with the crystal (high-Z) are largely dominated by the photoelectric effect, $R_{pe} \approx 1$. For higher energies, the photoelectric efficiency depends on various factors such as the incident energy, the absorption coefficients of the various interaction processes in the crystal, the mechanisms of energy deposition in the scintillator, the geometry of the experimental setup and the geometrical size of the detector.

The shape of the scintillation pulse of the inorganic scintillator is characterized by a fast rise time of a few tens of nanoseconds and a decay which has two components: a short (fast) exponential decay, whose decay time constant, τ_s , lies between a few and a few hundreds of nanoseconds which governs the main part of the pulse, and a long (slow) delayed component with a decay constant, τ_l , of few hundred nanoseconds up to milliseconds [41]. The fast decay component determines the

time response of the scintillating material. The decay components define the number, N , of the photons emitted at time t , such that

$$N = A_s e^{-t/\tau_s} + A_l e^{-t/\tau_l}, \quad (2.25)$$

where A_s and A_l are the relative magnitude of the short and long components, respectively. For CsI(Tl), the short decay constant $\tau_s > 1000 \text{ ns}$ is in contrast to $\tau_s \approx 230 \text{ ns}$ for NaI(Tl) (table 2.1), where 80% of the light intensity is emitted in $1 \mu\text{s}$. The long decay constants for both materials are in the order of hundreds milliseconds. The existence of triplet states that contribute to the emission of scintillation light in CsI(Tl) with partially allowed transitions from the excited into the ground state of luminescence centers, leads to a slow decay time ($\sim 1000 \text{ ns}$) relative to other inorganic scintillators such as LaBr₃(Ce) where the decay time is around 30 ns at room temperature [42].

During the absorption and emission in the scintillators, lattice vibrations take place which alter and broaden the shape of absorption and emission bands without changing the overall transition probability. The shape of absorption and emission bands can be determined from photoluminescence measurements in which the medium is excited by photons with energy E_{ph} [43]. The luminescence caused by ionizing radiation is called radioluminescence and leads to several emission bands, because of the existence of several luminescence centers. Furthermore the absorption and emission spectra are shifted in energy against each other by a value called Stokes Shift, E_{Stoke} , (fig. 2.5). This shift gives rise to minimize overlap and reducing the self-absorption, for an increasing coupling of the electronic states with lattice vibrations. In other expression, the Stokes Shift is specified as the energy difference between the absorption and emission band maximum and can be expressed by the Hyang-Rhys parameter, H [44]:

$$E_{Stoke} = (2H - 1)E_{ph}. \quad (2.26)$$

Generally the larger Stokes Shift is a result of a stronger coupling between electronic states and lattice vibrations (phonons). For CsI(Tl), $E_{ph} \approx 11$ meV resulting in a Stokes Shift $E_{Stokes} = 1.13$ eV where $H = 52$ [45].

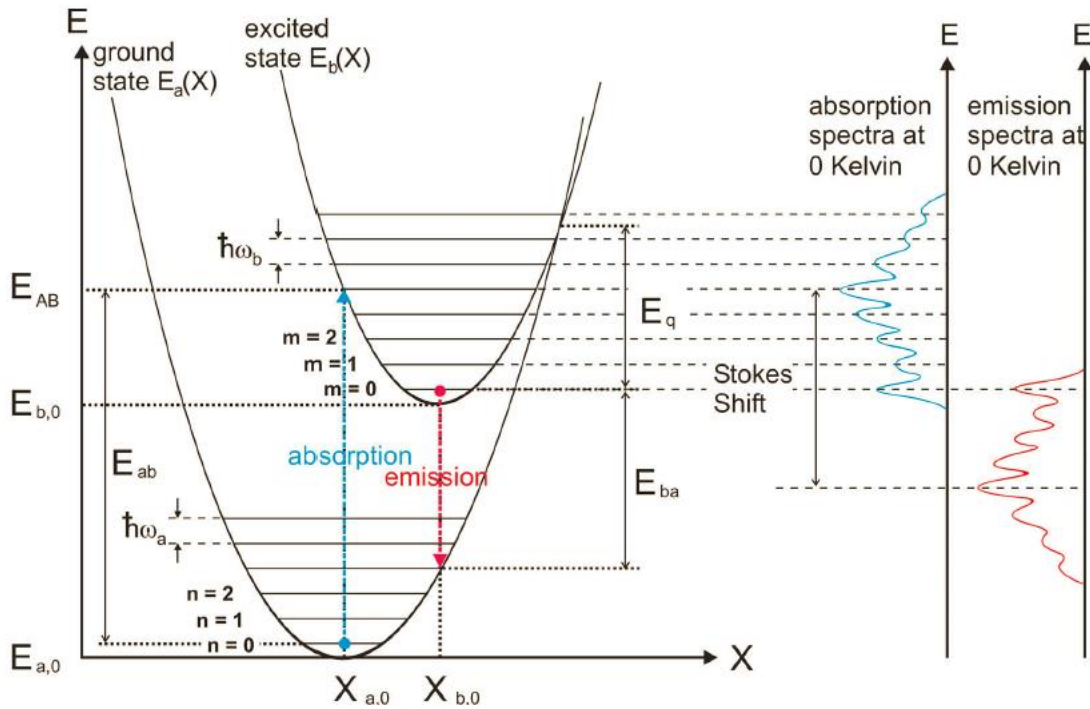


Figure 2.5: Configurational diagram in the harmonic approximation for a luminescence center in the ground and excited state [44].

The temperature dependent absorption and emission (luminescence) bandwidth can be described by:

$$\Gamma(T) = 2.35E_{ph} \sqrt{H \cdot \coth\left(\frac{E_{ph}}{2k_B T}\right)}, \quad (2.27)$$

where k_B and T are as defined for eq. (2.16). The activator material play a main role in the phonon and emission energy, and hence, it defines the shape and the maximum position in the scintillation spectra. As an example, figure 2.6 shows the normalized scintillation spectra of undoped CsI, CsI(Tl) and CsI(Na) at room temperature. CsI(Tl) shows its maximal emission at the wavelength 550 nm in contrast to 420 nm for CsI(Na) and 315 nm for undoped CsI.

The decay time of CsI(Na) is faster than that of CsI(Tl), so that it is suitable for detector applications, which have to resolve high count rates. In contrast, CsI(Tl) has a larger Stokes Shift [45] which make the self-absorption lower than that in other scintillators like CsI(Na) and LaBr₃(Ce).

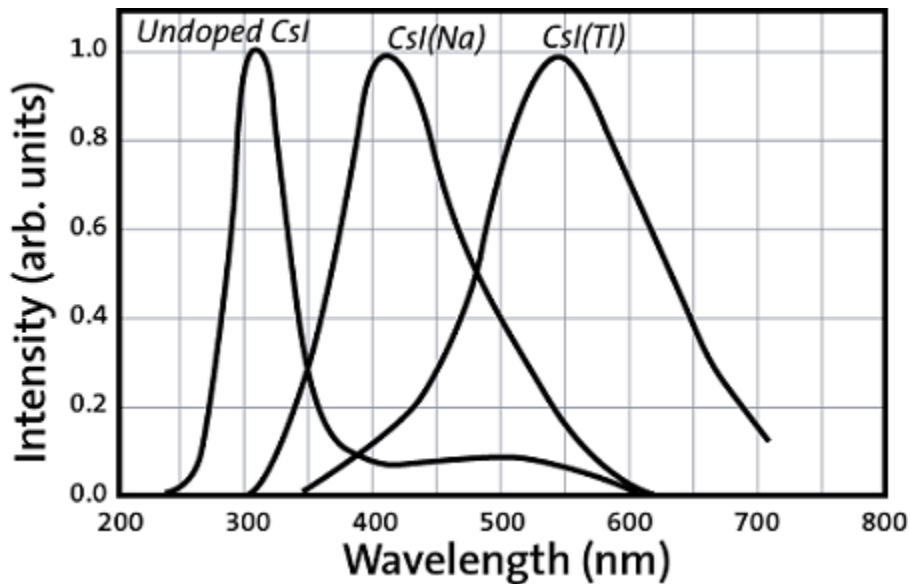


Figure 2.6: Normalized scintillation spectra of undoped CsI, CsI(Tl) and CsI(Na). CsI(Tl) shows its maximum emission at the wavelength 550 nm in contrast to 420 nm for CsI(Na) and 315 nm for undoped CsI [36].

2.4 Detection of the Scintillation Light

As shown in chapter 5, a CsI(Tl) scintillator with an optimized thickness (700 μm) has been coupled to a pnCCD detector has an excellent quantum efficiency at the energy of the signal generated by CsI(Tl) scintillation light. The maximum intensity of the scintillation spectra of most of the scintillators are in the near ultraviolet and visible (UV–Vis) range. At the same time the detection area of pnCCD is formed by the silicon chip. In this section, the interaction between UV–Vis radiation with silicon will be discussed.

To understand the optical properties of silicon, one needs to analyze its band structure, shown in figure 2.2. Photon absorption through electronic transitions between different bands can occur only if the total energy and momentum of the system is conserved. As discussed in section 2.1, the interaction of photons with silicon mainly occurs by the excitation of electrons from the valence band or impurity states into higher available energy states. But there is also the probability for excitations within the same band [47]. For certain photon energies the joint density of states of the conduction and valence band becomes maximum. This leads to the so called Van Hove singularities in the joint density of states. Two regimes with an excitation energy E_1 and E_2 (see fig 2.2), give rise to Van Hove singularities, hence to characteristic points of the absorption of silicon at $E = E_1$ and E_2 .

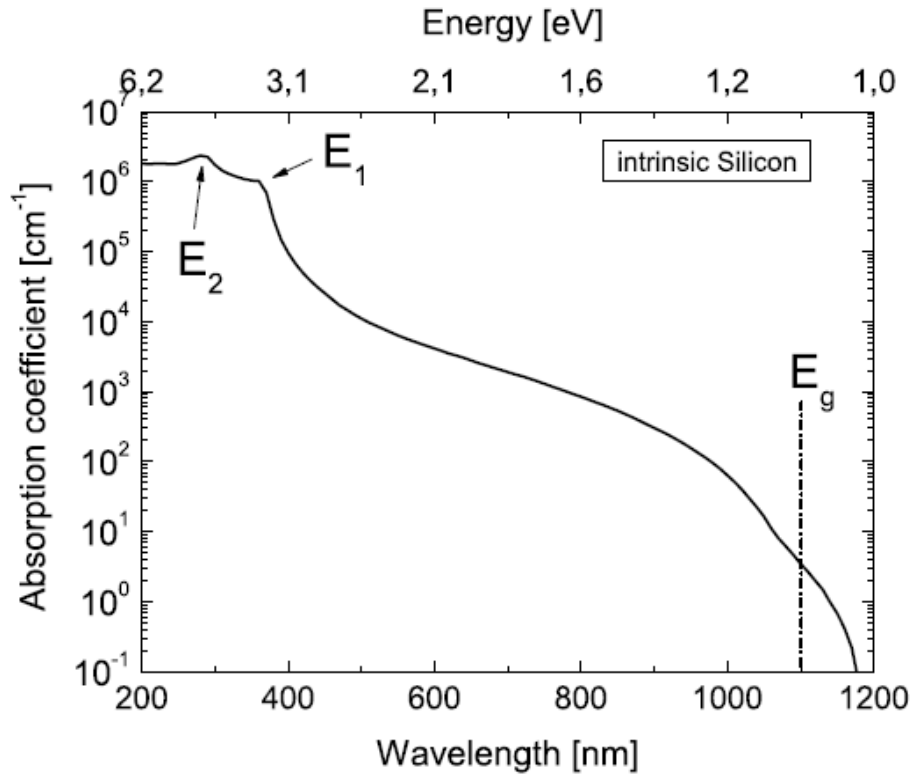


Figure 2.7: Absorption coefficient of intrinsic silicon at room temperature. Data are taken from [48].

Since silicon is an indirect semiconductor, phonon has to participate in the absorption process when the incident photon energy is close to the energy gap E_g . Thus the excitation of an electron from the valence into the conduction band by photons with energies around the energy gap of silicon, E_g , is a second order process with a lower absorption coefficient compared to the first order direct transitions for photon energies ≥ 3.3 eV. The absorption coefficient of intrinsic silicon is shown in figure 2.7.

When silicon is doped with impurities, the so called Mott transition occurs at doping concentrations of about 10^{18} cm^{-3} [47]. With increasing doping concentrations electrons or holes localized on the donors or acceptors become free carriers. Due to a narrower energy gap in heavily doped semiconductors, their absorption coefficient becomes larger [49]. Moreover, at high doping levels the high density of charge carriers enables an additional absorption process, where a charge carrier transfers the suitable momentum to the excited electron instead of a phonon. A

third absorption process in heavily doped semiconductors can also occur which is the free carrier absorption, where electrons or holes are excited within the same band. These three processes lead to an increase of the absorption coefficient in doped silicon compared to intrinsic silicon in the energy range below 3.3 eV. The absorption coefficients of intrinsic and heavily doped silicon are displayed in figure 2.8.

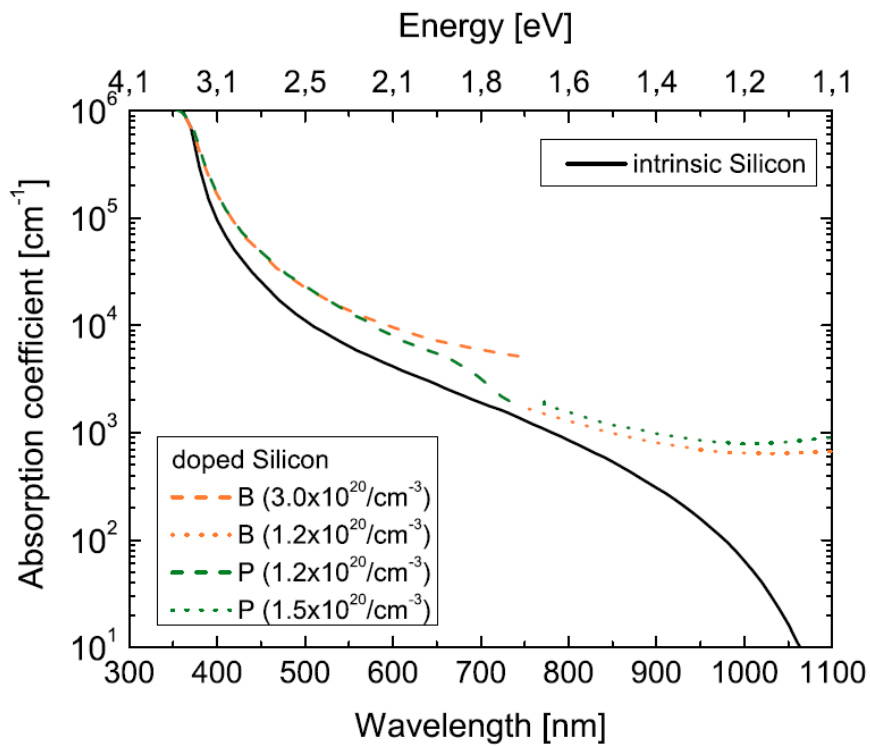


Figure 2.8: Absorption coefficient of intrinsic and phosphor or boron doped silicon at $T=300$ K. Figure is adapted from [50].

As can be seen in fig. 2.8, the absorption coefficient in boron and phosphor doped silicon at the wavelength of 400 nm is about twice as in intrinsic silicon, increasing to triple at 700 nm. This difference continues to increase for longer wavelengths such that at 1000 nm the absorption coefficient of the heavily doped silicon is larger by a factor of more than 10 times as that in intrinsic silicon. In pnCCD entrance window, the maximal doping concentration of silicon is at least one

order of magnitude lower than the doping concentration of silicon shown in Fig. 2.8. Hence, the absorption coefficient inside the p-doped part of the pnCCD entrance window is approximated by that of intrinsic silicon in the considered range from 300 to 1000 nm here. Intrinsic silicon becomes transparent for photon energies below $E = E_g - E_{ph} = 1.12 - 0.05 \text{ eV} = 1.07 \text{ eV}$ ($\lambda = 1160 \text{ nm}$), whereas for heavily doped silicon the absorption coefficient increases slowly to longer wavelengths, due to free carrier absorption.

The number of generated electron-hole pairs by absorbed UV-Vis photon is another important property one should consider for silicon. Figure 2.9 demonstrates the number of generated signal electrons in pnCCD per absorbed photon in the range 150 to 1050 nm. The data in this figure has been taken from [51].

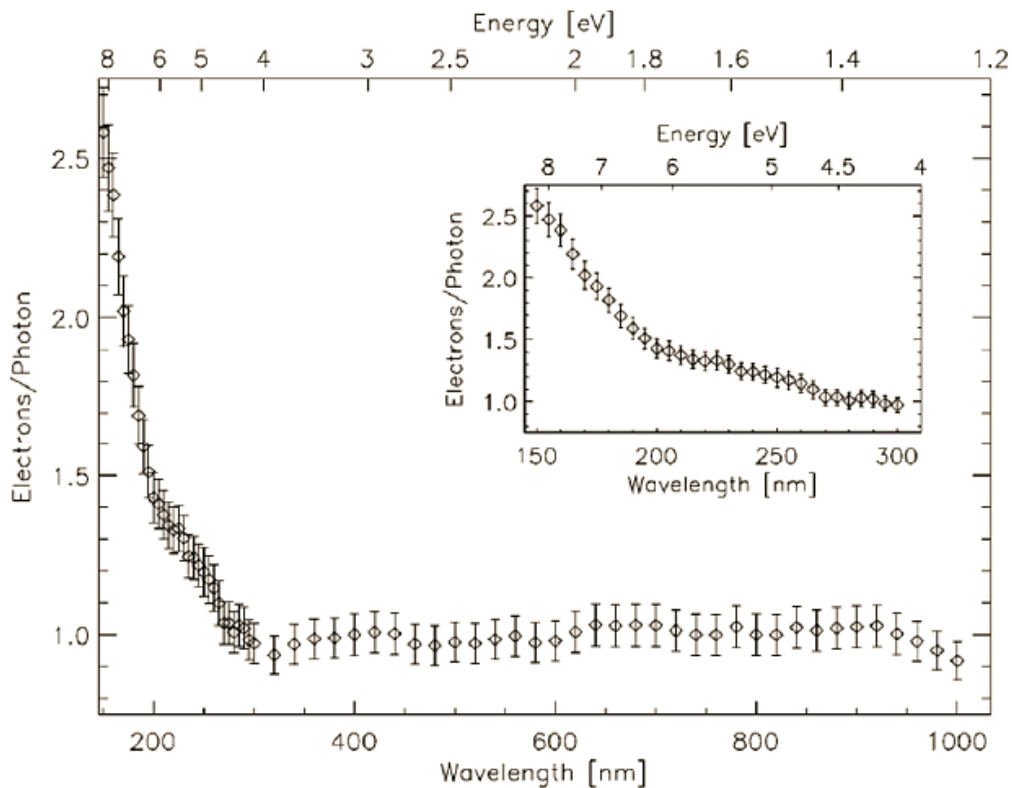


Figure 2.9: Number of signal electrons generated in pnCCD by absorbed photons in the range 150 to 1050 nm [51].

For incident photons with wavelength between 300 and 1000 nm which refers to the energy range from 4.1 to 1.2 eV, the number of measured signal electrons is almost constant and counts to 1. As the photon energy increased above 4.1 eV ($\lambda < 300$ nm), the number of the generated electrons starts to increase up 2.5 electron/photon at $E = 8.2$ eV ($\lambda = 150$ nm) .

3 pnCCD detector

P-n junction charge coupled device (pnCCD) is a solid-state detector and was initially designed and used for X-ray astronomy applications at European Photon Imaging Camera (EPIC) on the XMM-Newton satellite [52]. Due to its high sensitivity, good radiation hardness, high readout speed and many other advantages over other detectors, pnCCD has been utilized -along with its applications in space- for many synchrotron radiation applications such as crystallographic and material science applications [53-55]. Moreover, the pnCCD allows for energy dispersive Laue diffraction (EDLD) in the white-beam mode giving rise to a four-dimensional data volume output which is often not possible with other detectors used by conventional techniques and performed in the monochromatic mode. In this chapter, the concept and basic operation of the pnCCD as well as its physical properties are described. In particular, it will show how and with what energy and special resolution incident X-rays can be detected.

3.1 Concept and structure of pnCCD

PnCCD is a special type of CCD equipped with the p-n structure. While the depletion area of typical CCD is few microns near the surface, the full detector thickness of pnCCD is depleted in which it allows to find the proportionality between photon energy and size of the generated charge cloud. The charge cloud created by ionization of the detector material is stored as a function of energy of the incident radiation in individual pixels and then shifted from one pixel to the next one by applying and changing a voltage difference, until they reach a single readout node. The readout details will be shown later in a separate section of this chapter. In comparison with other CCDs where the shift registers are made up of metal oxide semiconductors (MOS), pnCCD with its p-n structure has the advantage to show a less risk of radiation damage due to ionizing radiation that cause accumulation of positive charges close to the oxide structure.

The sideward depletion which is the main peculiarity feature of pnCCD detector is a concept that was initially proposed by Gatti and Rehak in 1983 [56]. With this principle the detector is

considered as depleted field effect transistor (DEPFET). This structure can be achieved by setting up two heavily doped p^+ contacts separated by a weakly n-doped region, in addition to small but highly n-doped contact, n^+ , on the front side as shown in figure 3.1 to create an Ohmic contact to the Si bulk and serve as a readout node for the generated charge. This “ $p-n-p$ ” structure is considered as 2 p-n junctions with a common n bulk. The depletion of the bulk is achieved when an external high reverse bias V_b is applied such that the p-sides are connected to the same negative electric potential and the n^+ contact at the positive potential (fig. 3.1 (b)). If the same voltage is applied on both sides of p^+ , the potential minimum lies in the middle of the wafer. In case of pnCCD, different voltages are applied between the front and back side in a way that the potential minimum is shifted toward the front side. Hence, when x-rays hit the depleted region the generated electrons are shifted towards the potential minimum which is at the front side of pnCCD.

The vertical extension of the depletion area can be derived from (2.21) with a condition of $N_D \ll N_A$:

$$d = \sqrt{\frac{2\varepsilon(V_0 + V_b)}{qN_d}}. \quad (3.1)$$

The sensitive volume of pnCCD is typically, as the one used in this work, formed of a double-sided polished silicon wafer of 450 μm thickness. The whole sensitive volume is fully depleted by means of an external voltage in the range between 200 and 250 V.

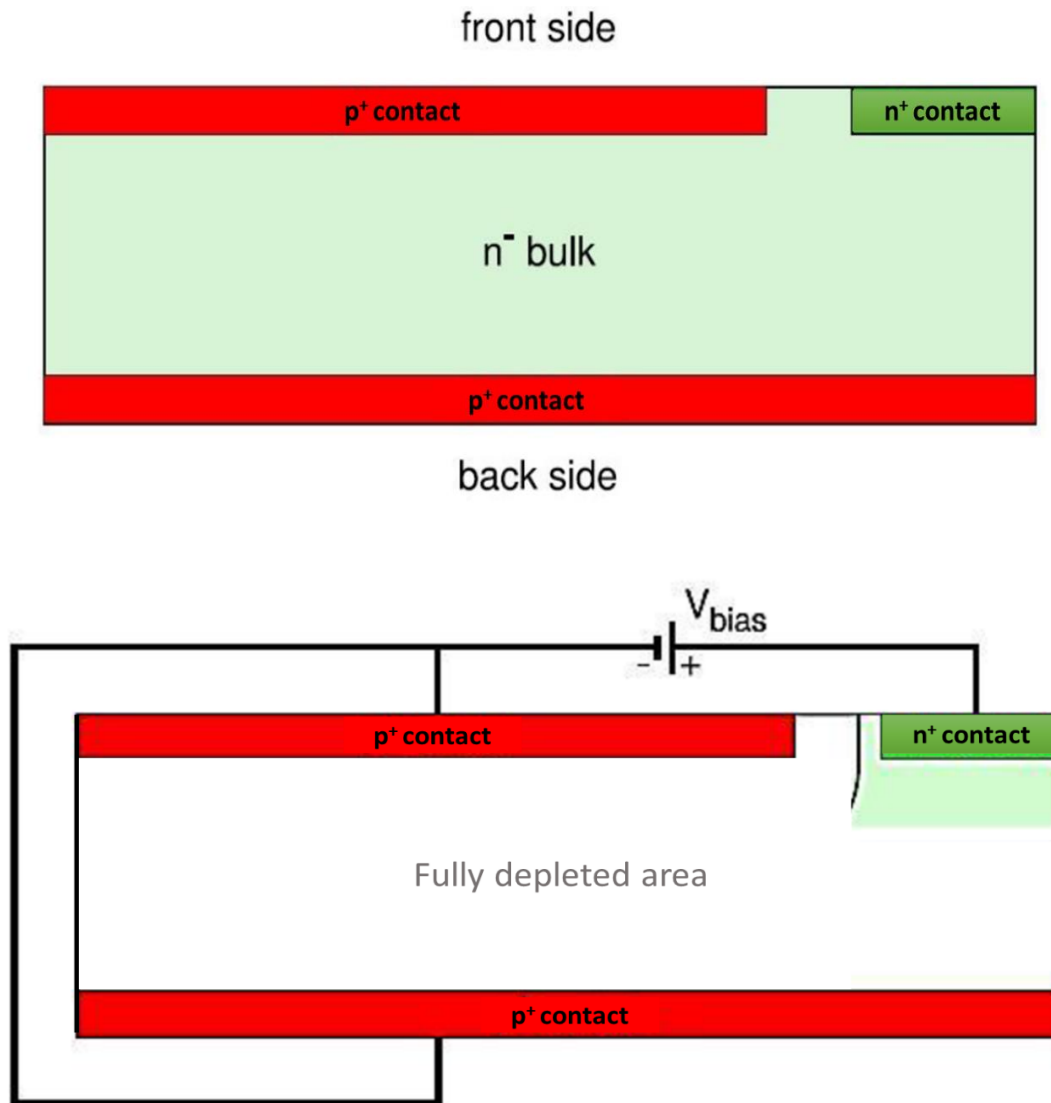


Figure 3.1: Principle of sideward depletion according to Gatti and Rehak [42]. (a) Only the intrinsic depletion zones of “p-n-p”-junctions have developed when no reverse voltage is applied. (b) For enhanced reverse voltage, the depleted region within the bulk is extended starting from the pn-junctions on the wafer surfaces

The pnCCD is an energy-, position- and time resolved detector, and hence its front side where the signal charges are collected need to be pixelated. The pixel geometry of the front side is achieved by means of p^+ boron implants in a form of parallel stripe patterns, while the unstructured back side is doped with homogeneous p^+ concentration (fig. 3.2). The potential under the stripe-like patterns alter with a periodic form allowing for charges to transfer toward the readout anode. Each

strip forms a channel of the detector which defines one dimension of the position coordinates, while the second position dimension is defined by the time taken by the charge signal to be transferred along the channel (strip) from its stored gate to the readout anode. The readout process will be discussed in the section 3.3.

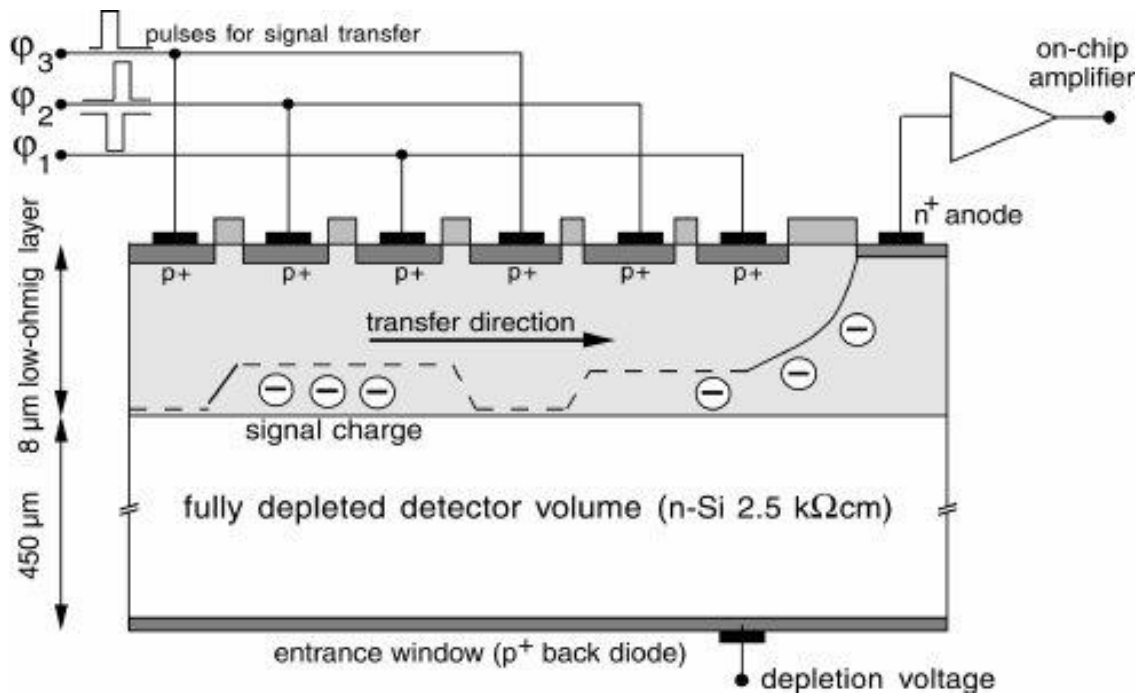


Figure 3.2: Cut through a fully sideward depleted pnCCD along one transfer channel. X-rays enter the detector unit from the back side and create electron-hole pairs within the Si bulk. The electrons drift to the front side, which has a pixel structure, and stored in potential minima and then transferred to the readout anode. Figure is adapted from [38].

3.2 Quantum efficiency

The quantum efficiency ε of semiconductor radiation detector defines its sensitivity to the incident radiation. In other term, ε tells how many photons will be stopped by the detector sensitive area

when irradiated by an incident beam. It can be described as the fraction of the detected photons intensity I_{det} to the incident photons intensity I_0 , i.e.

$$\varepsilon = I_{det}/I_0. \quad (3.2)$$

At the same time the number of interacting photons equals to the difference between the intensity of incident photons and those traversing the active area as defined in equation (2.12):

$$I_{det} = I_0 - I = I_0(1 - e^{-\mu x}). \quad (3.3)$$

μ and x are as defined in (2.12). By inserting (3.3) in (3.2) the quantum efficiency can be written as:

$$\varepsilon = (1 - e^{-\mu x}). \quad (3.4)$$

In real experiments, the silicon chip of pnCCD is equipped within an evacuated chamber with an entrance window with an attenuation coefficient μ_w and thickness t_w (for eROSITA pnCCD, which is used in this work, the entrance window consists of a 200 μm Kapton foil, 70% carbon and 30% oxygen, in addition to a 10 μm thick graphite coating and 20 μm aluminum foil). The incident beam reaches the detector plane under an angle 2θ (fig. 3.3) making a path length through the active Si layer with thickness t_{Si} equal to $t_{Si}/\cos 2\theta$. These conditions add more contributions to the quantum efficiency, and equation (3.4) becomes:

$$\varepsilon(E, \theta) = (1 - e^{-\mu_{Si}t_{Si}/\cos 2\theta})e^{-\mu_w t_w/\cos 2\theta}. \quad (3.5)$$

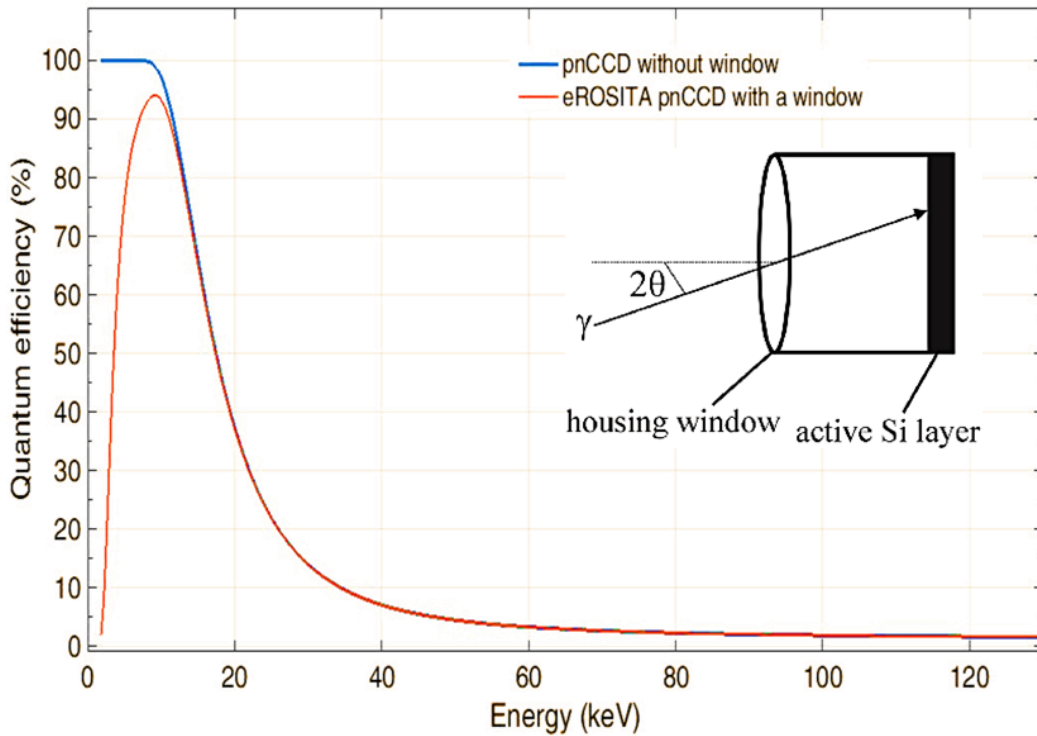


Figure 3.3: Quantum efficiency of pnCCD vs. Energy. The housing window causes a loss in the quantum efficiency in the energy range below 15 keV.

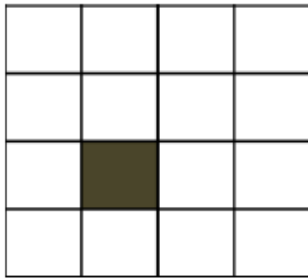
Figure 3.3 shows the simulated quantum efficiency of pnCCD detector of $450\ \mu\text{m}$ thickness in two cases: an ideal case without housing window and with incidence at $2\theta = 0$ (blue curve), and real experiment with entrance window (red curve). The geometrical condition of the real experiment is illustrated in the figure. In the ideal case, the detector has almost 100% sensitivity for X-ray photons below 10 keV. Above this energy the efficiency starts to diminish exponentially due to the finite thickness of the sensitive volume. It reaches a value of 4.5% at 45 keV and less than 2% at 100 keV. Furthermore, the existence of the housing window in eROSITA pnCCD affects the soft X-ray photons. Photons with energy below 2.5 keV are totally absorbed before they reach the detector silicon chip, leading to almost 0% quantum efficiency in this energy range. The maximum quantum efficiency of this case is around 95% at 10 keV. The entrance window with the thickness mentioned above has no stopping power for photons with energy above 15 keV, and subsequently, the quantum efficiency of eROSITA system is the same as of the ideal pnCCD.

In order to improve the quantum efficiency for hard X-rays, a novel type of pnCCD detector system has been developed. The new system is based on the coupling of CsI(Tl) scintillator to the silicon chip of pnCCD. It has been shown in 2.2 that the attenuation coefficient of CsI material for high energetic X-ray photons is larger than that of Si. On the other hand, Si shows a high sensitivity to the optical photons generated by the scintillators. Both gives rise to a high quantum efficiency in the order of 50% at 100 keV when the scintillator is coupled to the back side of pnCCD. The structure and properties of pnCCD + CsI(Tl) will be discussed in details in chapter 5.

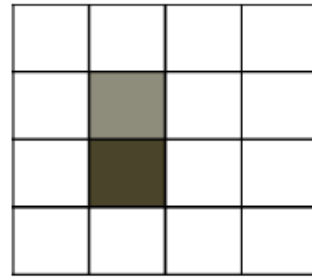
3.3 Read out

3.3.1 Generation of charges and collection

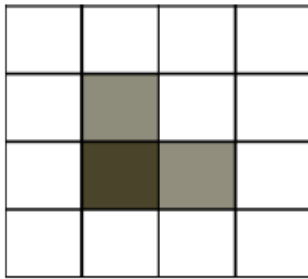
When a photon interacts with the silicon chip, it is converted into a cloud of electrons. This cloud is then drifted toward the pixels located at the front side. Depending on the position of the incident photon this charge cloud may not be stored within one single pixel (fig. 3.4(a)) [53]. Rather, it may impact with the boundary between two adjacent pixels and spread its charge over both. In such case the event is called "double "(fig. 3.4(b)). In the case of distributing over three or four pixels, the event is called "triple" or "quadruple" event, respectively (fig.3.4(c) and (d)). In order to distinguish real from parasitic impacts, only specific split events are valid, i.e. for the double event, the charge cloud generated by one X-ray photon can spread only over two adjacent vertical or horizontal pixels but not diagonally. For a valid triple event, the most intense pixel is positioned at the corner. In the quadrupole case the maximum and the minimum signals lies at the diagonals and not vertically or horizontally [54]. Some examples of invalid events are shown in figure 3.5. Such events are ignored in the data analysis.



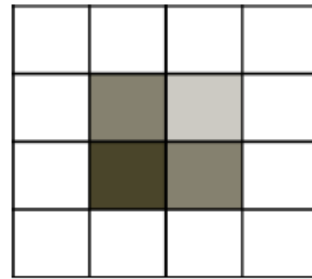
(a) Single



(b) Double



(c) Triple



(d) Quadrupel

Figure 3.4: Four possible events can take place at the of pixels level. Depending on its size, the charge cloud can be collected completely inside just one pixel (Single event), or it may spread over two, three or four adjacent pixels. In such cases the event is called double, triple or quadruple, respectively.

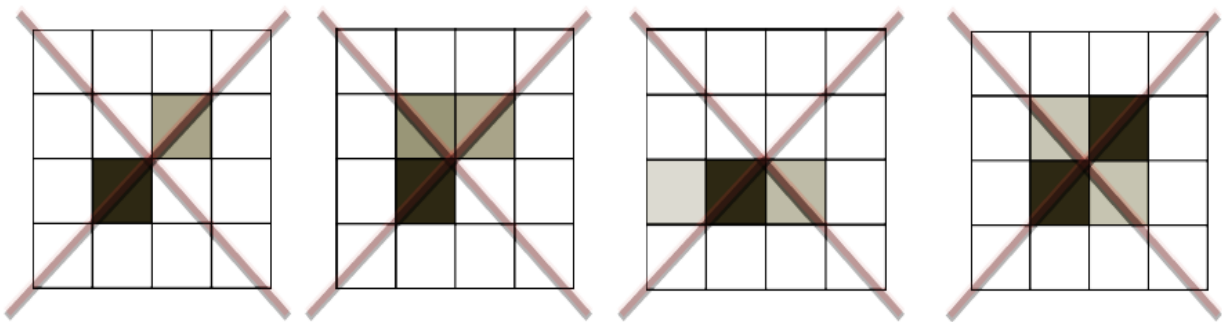


Figure 3.5: Examples of invalid events

The type of the event depends on the photon conversion position and on the charge cloud size which in turn depends on the converted photon energy. According to the discussions in chapter 2,

a 10 keV incident photon can produce about 3600 signal electrons, assuming that this photon undergoes a photoelectric interaction with silicon. This prediction has been justified with a good agreement by experiments performed by [54] in which 1750 signal electrons has been measured after a conversion of 6.4 keV photon and 4800 electrons for 17.5 keV photon. The size (rms) of these charge clouds were found to be between 8 and 10 μm , respectively. Generally, the possibility for an event to split over more than one pixel increases when the incident photon energy increases. The pixel size of pnCCD is $75 \times 75 \mu\text{m}^2$, and hence, if an incident photon with energy in the order of 100 keV is converted into a charge signal which is typically in the order of 20 μm size, at a position aligned below a pixel center, there is no chance for splitting and the event will be "single". Once the conversion process take place near the pixels border by a distance less than the radius of the charge cloud, the event will spread over the common-border pixels.

3.3.2 Frame store

If an X-ray photon interacts within the sensitive volume area during a charge transfer of a previous event, the position information of the new event can be lost. Such events are called "out-of-time events" [55]. In order to overcome this problem, a new pnCCD-based detector denoted as "frame store pnCCD" was designed and employed in 2002 for ROSITA satellite mission [56]. With this new design the detector is denoted as a frame store pnCCD. In this type, the total area of the detector is divided into two parts: the image area (IM) and the shielded frame store area (FS). The IM contains 384×384 pixels of dimension $75 \times 75 \mu\text{m}^2$ distributed over $28.8 \times 28.8 \text{ mm}^2$. The FS area has the same number of pixels as in IM but with pixel size of $75 \times 51 \mu\text{m}^2$ (fig.3.6).

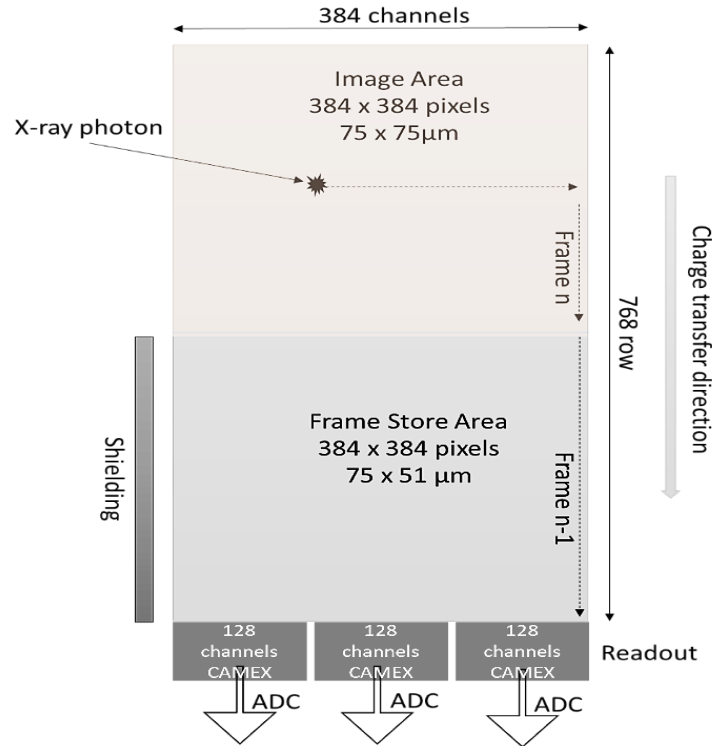


Fig.3.6: Scheme of eROSITA frame store pnCCD. The total detector area is divided into two parts: image area (IM), and frame store area (FS). The frame store area is shielded against any radiation exposure. While interaction of a photon is taking place at IM, the charge signal of the previous frame is stored temporarily in the FS before it proceeds to the CAMEX.

By this way, the radiation can be detected and integrated at the image area and transferred quickly to the frame store area relative to the readout time taken for charge transfer from FS to the readout node. The signal, which is now stored in the frame store area, is transferred relatively slow to the CAMEX. The number of "out-of-time events" is reduced significantly when the detector is operated in the frame store mode. In this mode, the detection of photons in frame 'n' can be processed in the IM independently from the signal readout from the previous frame 'n-1' in the FS. The sensitive area of the frame store pnCCD can be extended to a double size by un-shielding the frame store area. The operation mode in this case is denoted as full frame mode. Despite the large sensitive area provided by this mode which is useful in many cases, it has a disadvantage for synchrotron radiation applications due to the high flux exposure and longtime readout which is twice as that in frame store mode. If the new event is detected during this longtime charge transfer then the position information is likely to be wrong or the resulting image is smeared.

3.3.3 Charge transfer process

After the charges are integrated inside the pixels as signal electrons, these signals are transferred toward the readout node. Three shift registers with varying voltages ϕ_1 , ϕ_2 and ϕ_3 in a specific sequence are needed to move the signals from one pixel to the next until they reach the CAMEX chip (fig. 3.7). The procedure of moving one integrated charge by one row is as follow: After the collection of the electrons, more positive voltage is applied to the registers ϕ_1 and ϕ_2 compared to ϕ_3 which makes the potential for the electrons lower below registers ϕ_1 and ϕ_2 , forcing the electrons to be trapped there. Next, ϕ_1 is operated at lower voltage and ϕ_3 at higher which drive the electrons away from the first register toward the second and third. Applying a higher voltage at ϕ_1 and ϕ_2 of the next pixel and lower voltage for ϕ_3 of the current pixel drives the charges toward the pixel of the next row. This step by step procedure is shown in figure 3.7. The time taken for one shift of the voltage is 100 ns. For the movement of the signal charge from one pixel to another, six phase shifts are required which are equivalent to 600 ns. This leads to 230 μs for signal charge to travel 384 pixels. The voltage of the applied pulses is typically between -20V and -15V relative to the substrate contact.

During charge transfer process, a part of the moving electrons might be lost due to defects in the silicon crystal [57]. Another factor that can cause a loss of transferred charges is the imperfection in the potential structure of the shift registers. The fraction of the charges shifted to a given pixel is denoted by " Charge Transfer Efficiency (CTE)" and defined as:

$$CTE = \frac{q_i + 1}{q_i} \quad (3.6)$$

where q_i and q_{i+1} are the numbers of charges before and after shift from row i to $i+1$, respectively.

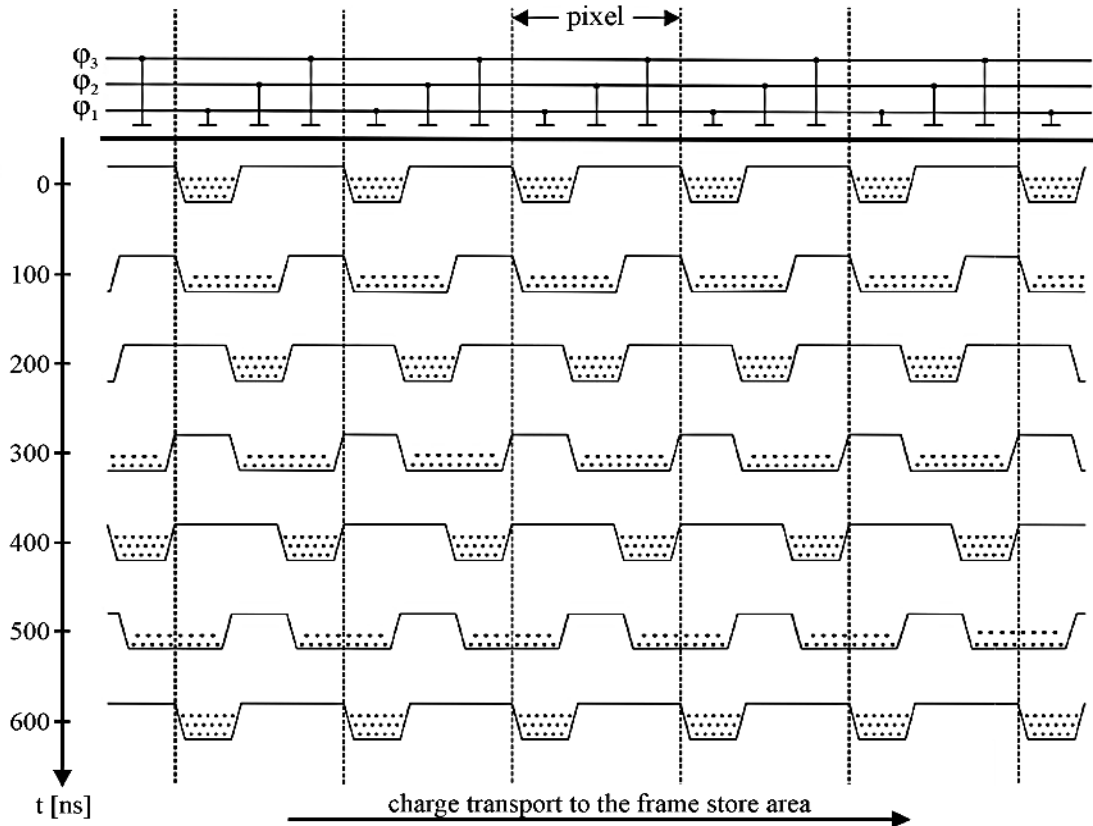


Figure 3.7: Three-phase voltage sequence used to transport signal electrons from the image area to the frame store area. The charge transfer is performed within spatially and temporally varying potential wells. In the case of charge storage below one register, the electrons can be transferred by one pixel unit within 600 ns. In an alternative operation mode of the pnCCD, the charge is collected below two registers. Figure is taken from [43]

The complement of CTE is denoted as charge transfer inefficiency $CTI = 1 - CTE$, and gives the relative number of electrons which are captured by traps and fed to subsequent pixels. The CTI value of pnCCD measured by means of a monochromatic X-ray source is in the order of 10^{-5} [57].

3.3.4 Signal amplification and readout electronics

Once the charge signals leave the channels and arrive the readout anode, they enter the Junction Field Effect Transistor (JFET). At this stage, the signals are amplified and the signal to noise ratio increases. The readout anode is connected with a Reset-FET gate which removes the collected charges and switch to a new frame by applying a steady voltage at the anode. The signals are

transferred to the First-FET which acts as preamplifier (fig. 3.8). Particularly, for high count rates at which many electrons are shifted to the anode, an incomplete reset may occur. This leads to charge avalanches at the first FET gate, constricting the transistor channel entirely and short-circuiting the supply voltages of the first FET. Further sampling and processing then take place at the CAMEX.

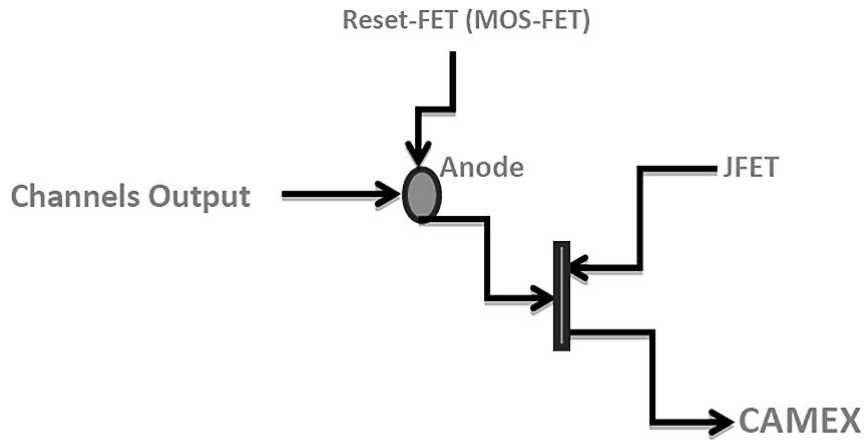


Figure 3.8: Schematic view of on-chip electronics at the readout anode. Charge signals coming at the readout anode are amplified by the n-JFET and cleared by the MOSFET after each readout

CAMEX is a special electronic chip designed for pnCCD to amplify and sample the signals received from the parallel channels. In pnCCD used by eROSITA, three CAMEX are located at the endpoints of 384 channels (each CAMEX connected to 128 channels). The input of CAMEX is connected to the JFET current source as shown in figure 3.8. It receives the absolute analog signals [58]. These signals are proportional to the charge clouds arrived to the readout anode. The different stages of the CAMEX are shown in figure 3.9.

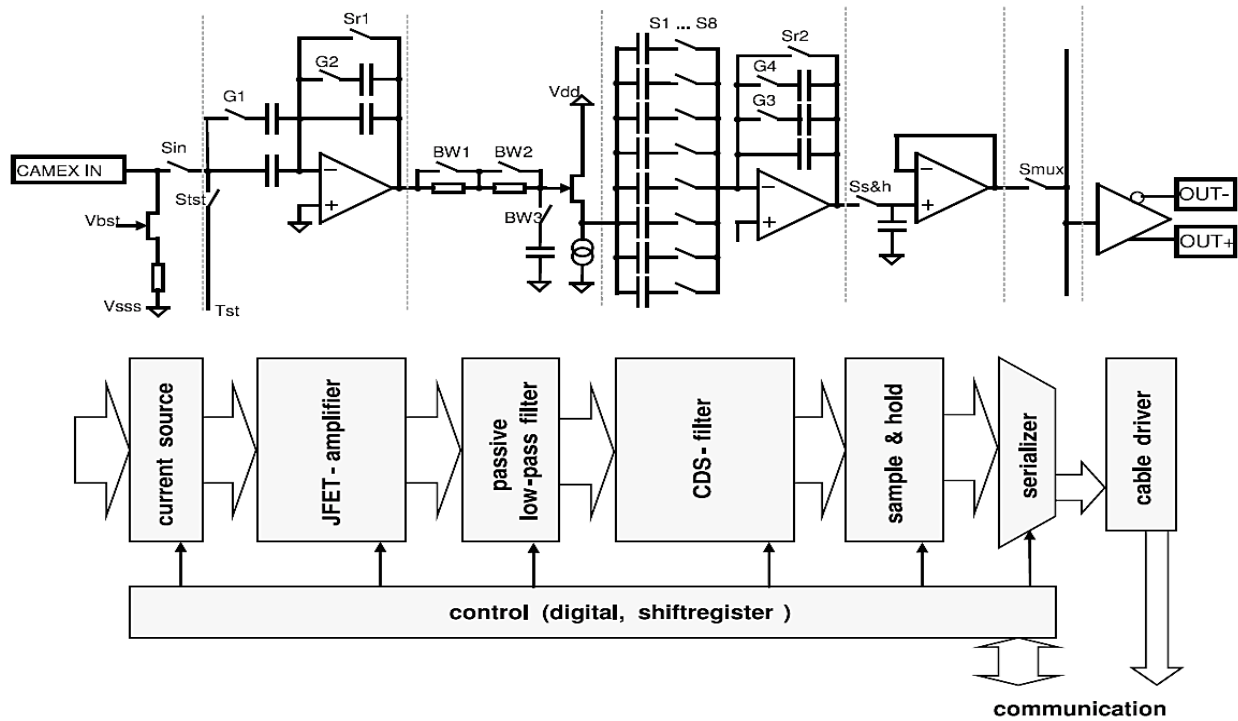


Figure 3.9: CAMEX diagram. Different stages for the signal processing: After pre-amplifying at JFET, the signals filtered by passive low-pass and CDS filters before sampling and digitalizing and then serialized to the cable driver. Figure is taken from [32]

The maximum detection of X-ray radiation can be achieved by controlling two voltage amplifier stages on JFET and CAMEX and using CDS-filters to prevent the low-noise signals from entering the sample and hold gate. The baseline signals are measured before the charge signals reach the anode which separates the collected signals from the noise. After the electronic processing, the signals are re-amplified and transported to PC by means of analog-to-digital converter (ADC).

3.4 Spatial resolution

The spatial resolution of the pnCCD mainly depends on the pixel size. Other factors related to the experimental conditions including frames rate, energy range and incident angles have to be taken into account. As the detector works on the principle of photon-charge conversion, the volume of the created charge cloud strongly contributes to the spatial resolution. Depending on the charge

cloud diameter and the conversion position with respect to the pixel borders, the cloud may split over more than one pixel (see section 3.3.1). At the same time the size of the charge cloud is proportional to the photon energy in which a 6 keV photon creates a cloud of diameter about 8 μm , and about 12 μm for 25 keV photon [54]. This implies that for soft x-rays, the spatial resolution is much better than that in case of hard x-ray where the electron cloud size may exceed the pixel size.

However, according to [59], the collected events can be localized with a subpixel resolution. The information about charges cloud size and their distribution over the pixels served as input to determine the 2D center of mass coordinates of the charges cloud. With this approach, a spatial resolution of 2 μm could be obtained for triple and quadruple events [54].

The scattering angle 2θ of the incident photon with respect to the CCD normal influences the retrieved event position. The created charges at this point are drifted in the direction of the electric field (E) which is parallel to the normal (fig. 3.10). This phenomenon is so called *Parallax effect* [57]. The position of such events needs to be corrected by taking into account the chip thickness and on the interaction point in depth. For high energetic photons the conversion of photons take place near the store registers (in case of back illuminating detectors). Consequently, the deviation from the real position is smaller compared to those interacting near the back side.

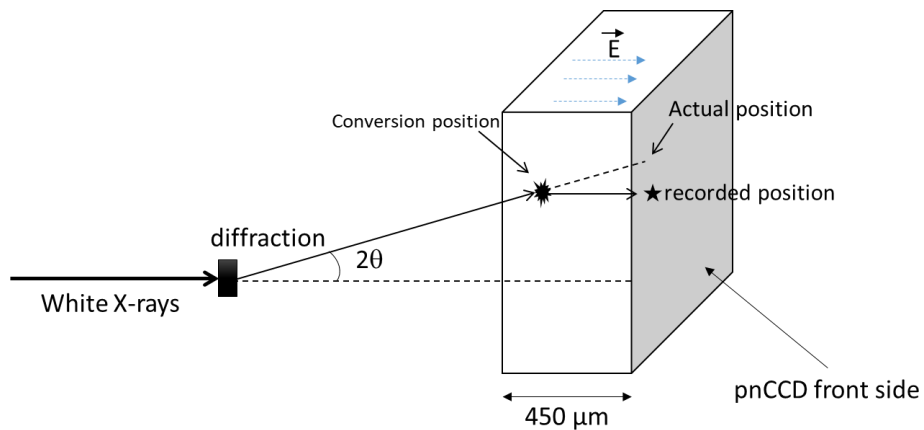


Figure 3.10: Parallax effects within pnCCD. The recorded position is usually different from the actual position due to the drifting of the generated charge cloud in a direction parallel to the applied electric field toward the pixel structure side.

Furthermore, during the readout process of a given frame, more photons keep hitting the sensitive area producing “out-of-time” events that causes a smearing of the image and results in wrong position information. In order to reduce the influence of this phenomenon, the detector is operated at fast frame rate and the radiation flux is often reduced as low as possible to a level commensurate with experiment requirements.

It’s worth mentioning that for the pnCCD combined with scintillator, the light generated in the scintillator and detected by pnCCD is often spread over more than 5 pixels which makes the spatial resolution of the combination system worse compared to the case of the naked pnCCD [13]. This case will be discussed later in chapter 5.

3.5 Energy resolution

The energy resolution of registered electrons can be determined by measuring the FWHM of the Gaussian energy distribution of a spectral peak centered at energy E of a monoenergetic X-ray line. In addition to the peak energy, the CCD material and equivalent noise charge (ENC) play a main role in determining the energy resolution of the detector. This can be explained by the following relation [60]:

$$FWHM(E) = 2.355w \sqrt{\frac{FE}{w} + ENC^2}$$

where $F=0.115$ is the Fano factor for Si [61]. $w=3.65$ eV is the electron-hole pair creation energy in Si and 2.355 is the conversion factor between the standard deviation of a Gaussian and the FWHM. ENC includes the different noises that are produced at different positions of electron (on-chip electronics, amplifiers, CAMEX and the leakage current due to thermal conditions). Such noises are unavoidable for real detector. It can be reduced by cooling the detector to a low temperature (~ -30 °C). Furthermore, the low energetic photons such as optical photons affect the energy resolution and suitable materials are usually used as chamber entrance window to filter out

such noisy photons and prevent them from entering the pnCCD chamber. The FWHM for pnCCD was measured experimentally by [53] in term of energy using various X-ray fluorescence lines. With a signal threshold of 6σ ($\sigma = 9.3 e^-$), the FWHM was found to be between 200 eV and 280 eV within the energy range between 6.4 and 17.4 keV. The measured lines with their respective FWHM are summarized in table 3.1.

Emission line	Fe-Kα	Fe-Kβ	Cu-Kα	Cu-Kβ	Pb-Lβ	Rb-Kα	Rb-Kβ	Mo-Kβ
E (keV)	6.4	7.05	8.03	8.9	12.6	13.3	14.9	17.4
FWHM (eV)	212	210	218	221	243	249	260	280

Table 3.1: Energy resolution of the pnCCD for different fluorescence energies at a signal threshold of 6σ described by the FWHM of the individual peaks containing only single events. Data has been taken from [53].

3.6 Time resolution

The sum of the integration time (exposure time), charge transfer and readout times form the cycle time and the frame rate. This rate varies from one pnCCD model to another and from one mode of operation to another. For example, for pnCCD with 384x384 pixels operating in the frame store mode, the complete cycle time is 11.28 ms while for 256x256 modules this time is reduced to 7.5 ms. Raising the exposure time leads to more integrating events. But at same time, this causes more out-of-time events. The frame rate and consequently the time resolution of pnCCD can be improved by means of pixel binning (timing mode). By this mode, the charges of several adjacent pixels are integrated together as they belong to one “large pixel”. The integrated charges are then transferred to the next “large pixel” and so on. For example, for 2-fold pixel binning, the charges from two rows are merged together and are transferred into the next two pixels and so on until they reach the readout node. 4,8,16 and more-fold binning is possible and this leads for a proportional reduction of the cycle time (half of the original time in case of 2-fold and quarter time for 4-fold binning) [62]. However, mixing of several pixels together distorts the position resolution of the

produced image. Hence, the timing mode is advantageous for the applications with time resolved process where spatial resolution is of less importance.

4 Application of pnCCD in material science: single grain analysis of polycrystalline nickel

Industrial components ranging from micron to a few meters in size are mainly composed of polycrystalline materials. Improving their mechanical properties requires better understanding of the material response during service, such as mechanical loading and deformation behavior of the collective and individual grains. Due to the specifics of the processes of manufacture polycrystalline materials may show a sharp distribution of orientation (texture), variety of crystallographic structure (phases) and grain sizes (size effects). As a result, structure analysis of polycrystalline materials is required to understand the complexity of the system. For example, during plastic deformation (mechanical loading) each grain responds differently to the external force due to its initial orientation. On the other hand, interaction with the surrounding grains play a role in which the response of an embedded grain is different from what is expected from an isolated grain [63]. Since inter- and intragranular interactions occur at the same time, an experimental technique is required to separate the individual response of each grain [64, 65].

Today, the dominant set of tools for characterizing the microstructure of polycrystalline materials is electron microscopy (EM). However, despite its versatility, EM lacks the capability of probing the temporal evolution of orientation and strain fields in the bulk of micrometers to millimeters sized specimen. Recent advances in synchrotron-based X-ray imaging and diffraction techniques offer interesting possibilities for non-destructive 3D grain characterization of polycrystalline materials such as crystallographic structure, orientation and strain of individual grains [66].

The pnCCD has been previously used to study perfect single crystals and to determine the crystalline structure and 3D strain [13, 67, 68]. In this chapter the benefits of utilizing pnCCD in energy-dispersive Laue diffraction experiments (EDLD) for the analysis of polycrystalline materials will be shown. The feasibility of resolving single grains from the polycrystalline matrix will be exhibited. Using ultra high energy X-rays and a broad X-ray beam, a large number of grains can be exposed simultaneous providing a reasonable number of Laue spots with sufficient intensity. The proposed method is fast and requires no sample rotation, hence, well suited for *in situ* experiments. It allows for probe large areas of heavily deformed samples and it is not limited

to grains located at the sample surface. The second advantage is the relatively flat Ewald sphere with a very low curvature which allows measuring complete crystallographic zones. As material system to probe the lattice strain distribution we used polycrystalline Nickel wires with an average grain size of 50 μm . The possibility of extracting both local and global statistical information to gain deep insights into load partitioning in complex polycrystalline microstructures will be demonstrated.

EDLD experiment using ultra-high X-ray energy has helped to elucidate the structure and mechanics of polycrystalline solids in the context of a wide range of problems. Abboud et al. 2017 [4] has studied to determine the full strain tensor from an experiment with single shot x-ray exposure using two-dimensional energy dispersive detector (pnCCD). They have calculated the deviatoric and hydrostatic components of the elastic strain and stress tensors in a copper sample. Phillips et al. 2004 [5] have investigated the stress distribution in a polycrystalline Al film on a Si substrate during cyclic thermal loading. The presence of a stress gradient from the whisker root to the Sn parent material that drives the whisker growth has been confirmed as well by Choi et al 2003 [6].

Using diffraction-contrast microscopy with mono-energetic x-rays, the mapping of lattice response and deformation of ductile polycrystalline material under an external load could be evaluated with high angular resolution [69, 70]. Energy dispersive Laue diffraction experiment using micro-sized beam has been used as an effective method to study the intra- and intergranular lattice distortions at the micro-scale [71]. With this method, many local grains can be irradiated at the same time by collimating a polychromatic X-ray beam to a spot size that can cover a specific number of grains. The diffraction pattern arising from the gauge region consists of a number of diffraction spots from each grain. From the location of these spots, the grain orientation and the deviatoric elastic strain within the illuminated gauge volume can be deduced. Fast acquisition rates of pnCCD and automated algorithms for the processing of data (diffraction patterns) allows for rapid mapping of relatively large areas [72, 73].

4.1 Energy-dispersive Laue diffraction

A polycrystalline Nickel wire of high purity (99.9 %) and of 0.5 mm in diameter and 20mm in length has been prepared and placed into a glass tube filled with Argon gas in order to reduce the number of grains by a heat treatment. The specimen was subjected to an annealing at 850°C (65 percent of melt temperature) for up to 20 hours resulting in a residual mean grain size of 50 μm . Finally, the wire was etched close to the center of specimen in order to further reduce the number of grains within the probing area and to control the breaking point during application of external mechanical stress. For the electrochemical etching we used a solution of 95% methanol and 5% HClO_4 as electrolyte and Al and Sn as anode and cathode material, respectively. The etching did create a waist of about 80 μm in diameter. The samples were loaded in steps using a small-scale tensile device [74] and were investigated at displacements of 0, 40, 80, 120 and 200 μm .

The EDLD experiment was performed at the energy-dispersive diffraction (EDDI) beamline of BESSY II in Berlin with white synchrotron radiation generated by a 7 T multipole wiggler. The experimental setup is shown in figure 4.1. The sample equipped at a straining device is installed on a translational stage for alignment. The pnCCD was equipped on a translation stage 78(2) mm behind the sample. A lead beam stopper was placed in front of the detector. A 25 mm thick aluminum plate was placed in between the exit window and sample in order to absorb the highly intense low energy part of the white incident spectrum. As a result, the applicable synchrotron spectrum was tailored to a band pass ranging between 30 to 130 keV. The size of the incident beam was reduced to $200 \times 200 \mu\text{m}^2$ by means of pinholes directed onto the gauge section.

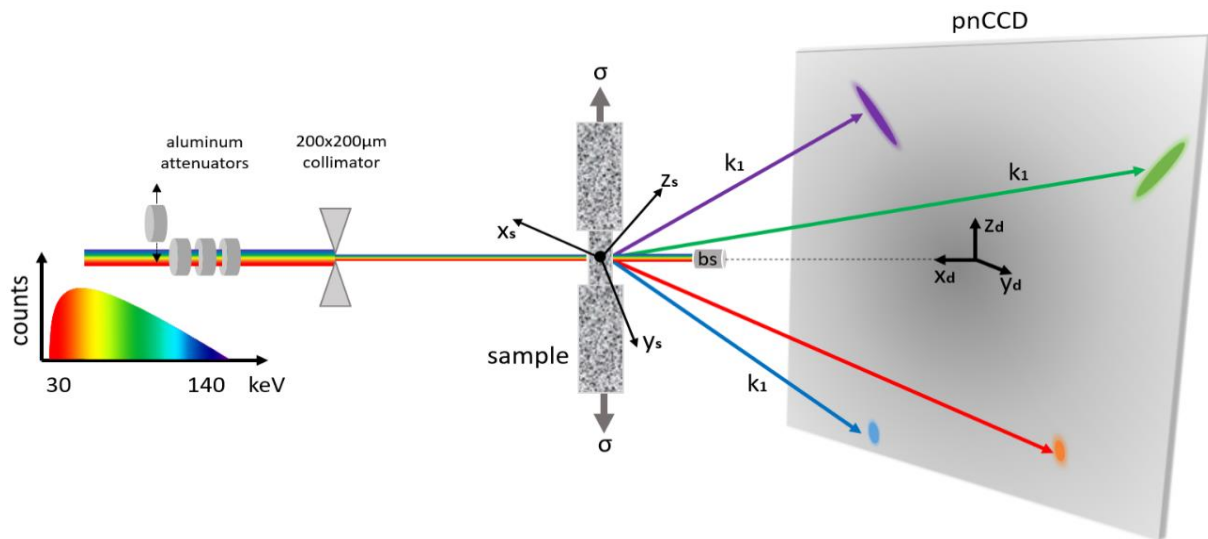


Figure 4.1: EDLD experimental setup at EDDI beamline of BESSY II. The Ni sample was measured in transmission geometry using the pnCCD. The incident spectrum is tailored by inserting a 2.5 cm Aluminum cylinder on the beam path between sample and detector.

An eRosita type pnCCD module with a pixel dimension of $75 \times 75 \mu\text{m}^2$ and an energy resolution of 0.13 keV at 6 keV and 0.470 keV at 100 keV was used. The expected lattice strain resolution (d-value) depends on the spatial and spectral resolution of a diffraction peak. In this particular experiment the detector was placed in the forward scattering direction at a distance of 78(2) mm behind the sample, the corresponding accuracy in the measured Bragg angle (2Θ) is in the order of 1×10^{-3} degrees resulting in a resolution in d-value in the order of $\Delta d/d = 10^{-3} - 10^{-4}$ ($< 0.1\%$). Due to the small active area of the sensor chip ($2.88 \times 2.88 \text{ cm}^2$), the available 2Θ range is limited to $\pm 10.8^\circ$.

Laue patterns were recorded in transmission geometry using the pnCCD operating in the single photon counting mode. However, the gauge section shows signs of residual strain as the Laue spots are spatially extended. Figure 4.2 (a) represent the Laue image from the bulk part, while 4.2 (b) is the thinned part. The recorded data sets consist of 300 dark frames (noise and offset correction) and 50,000 frames (at a frame rate of 100 Hz). The Ni fluorescence line (k-alpha peak) was used to correct for gain fluctuations between different detector channels as discussed in details in [72]. The streaks shown in figure 4.2 used for further analysis are identified by ellipses and numbers.

Other reflections with very low or much too high intensity (pixel saturation) were excluded from further data treatment.

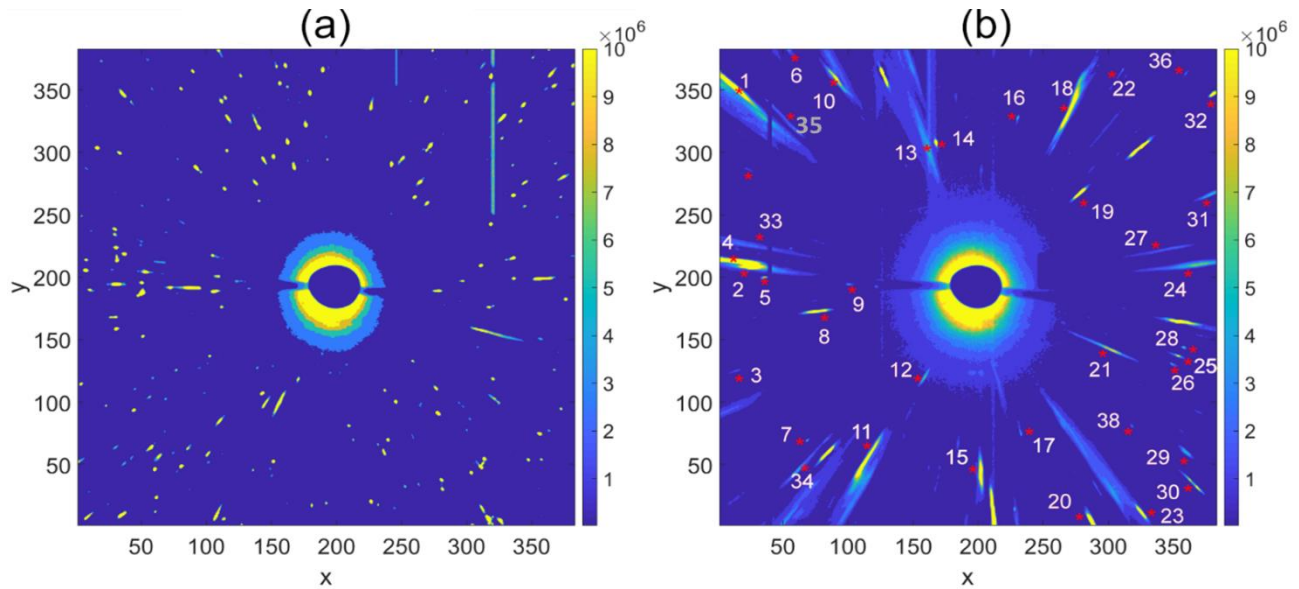


Figure 2.2: Laue pattern of the as-prepared sample (a) sample bulk, (b) gauge section. The circular shadow at the center is due to the use of lead beam stop between the detector and the sample.

During data analysis of the recorded Laue patterns, one should keep in mind the consequences of a forward scattering experiment where variations in the Laue spots are influenced by experimental setup parameters: firstly, the active area of the detector used is relatively small, limiting the accessible size of the reciprocal space (2θ) which is in close vicinity to the primary X-ray beam. Secondly, the incident X-ray beam energy spectrum ranges between 30 to 130 keV, and therefore, the accessible diffracting planes are nearly parallel to the incident X-ray beam corresponding to Miller indices ranging between $(-4 < h, k, l < 4)$. In figure 4.3 the geometric diffraction condition (Ewald sphere) is presented. A reciprocal

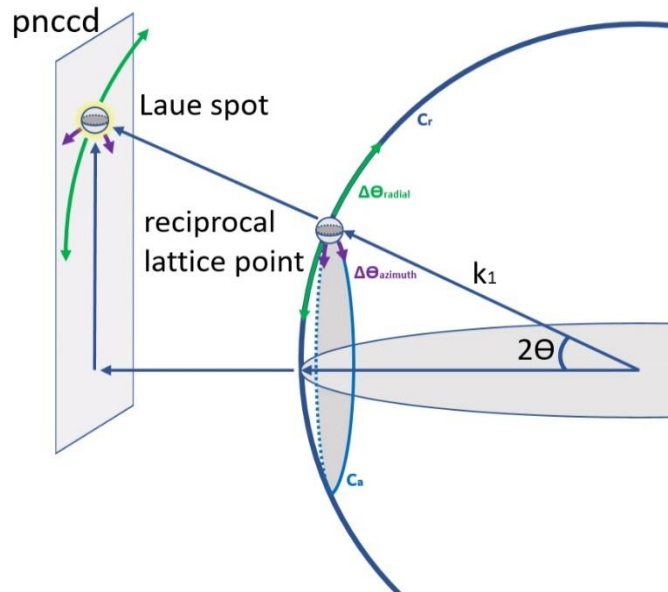


Figure 4.3: A representation of the diffraction geometry. A movement of the reciprocal lattice point along the radial direction dominates the movement along the azimuthal direction.

lattice point which fulfills the diffraction condition is shown. The Laue spot which corresponds to the associated lattice planes is the perspective projection (along the diffracted k_1 vector) of this reciprocal lattice point on the detector. While the crystal is stationary the Laue spot on the detector is seen as a single point. A crystal rotation (around an arbitrary axis) by an angle Θ corresponds to a variation of $\Delta\theta_{radial}$ and $\Delta\theta_{azimuth}$ around the circumference of circles C_r or C_a . As a result, the perspective projection of the reciprocal lattice point would also move on the detector with a value equivalent to either $S_{c_r} = R_{c_r} * \Delta\theta_r$, $S_{c_a} = R_{c_a} * \Delta\theta_a$ or both. However, since $R_{c_a} \ll R_{c_r}$ the Laue spot on the detector moves preferable towards one direction $S_{c_a} \ll S_{c_r}$ therefore, the trace of the reciprocal lattice point due to deformation is always maximum along the radial direction but small in azimuthal direction. Laue microdiffraction streaking analysis as proposed by Ice and Barabash [8], hence, makes no sense for the used energies and experimental geometry of our experiment.

To highlight on the subject further, a simulation was performed in which we generate a Laue pattern of a Ni crystal with the same conditions as in the experiment. The Laue pattern from perfect Ni single crystals is shown in figure 4.4 (a). The actual detector size is marked with a dashed gray box. The angular position ' θ ' of each Laue spot depends on the relative orientation of the corresponding lattice plane with respect to the incident beam as stated by Bragg's Law. If the crystal rotates around the (x, y, z) axis by (α , β , γ) degrees, the angular position of Laue spots at the detector plane will follow the direction indicated by arrows as seen in figure 4.4 (b). Streaking is formed in case of a continuous rotation of the lattice plane because each pixel along the streaking fulfills the Bragg's condition for a slightly different X-ray energy.

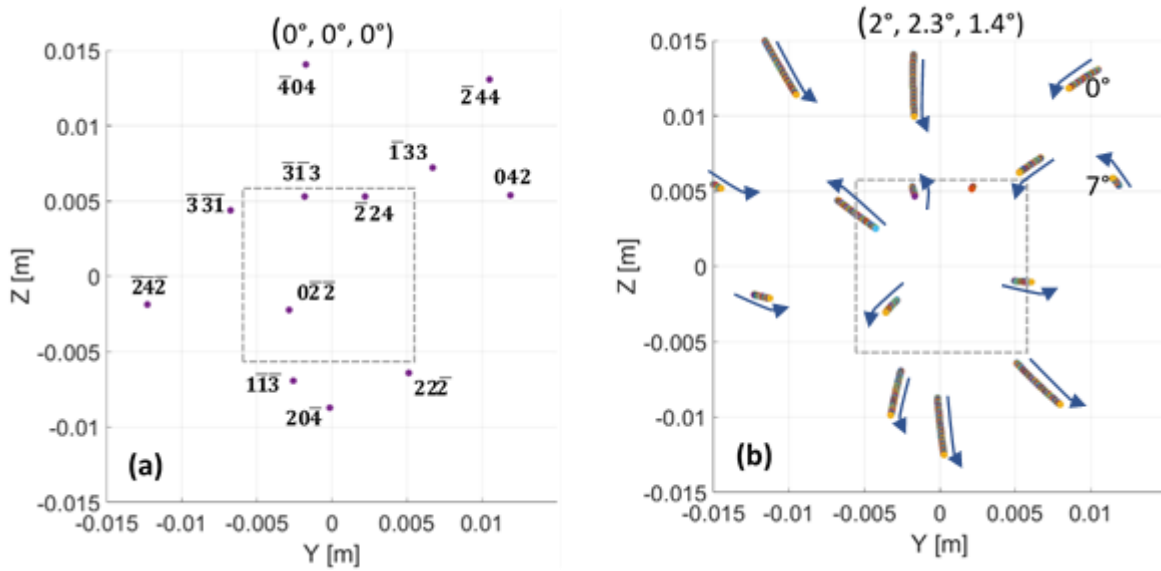


Figure 4.4: simulation of Laue pattern generated by Ni crystal with white X-ray beam ranging between 30 and 130 keV where in (a) the crystal is perfect while in (b) the crystal is randomly rotated from $(0^\circ, 0^\circ, 0^\circ)$ to $(2^\circ, 2.3^\circ, 1.4^\circ)$ in a step of 0.01° .

Comparing the simulation shown in figure 4.4 and the experimental Laue patterns shown in figure 4.2 (b) one can say that the grains in the gauge section of the as-prepared sample were already deformed and every individual grain may be split into sub-grains rotated randomly with respect to each other. Supposing the interplanar distance, d , is constant across the reflection plane i.e. $\Delta d/d = 0$, E and θ over the streak should follow Bragg's law as $E \sim 1/d \sin \theta$ while in case d is changing by a value of Δd at a specific position on the lattice plane, then a deviation from Bragg law will occur such that $E \sim 1/(d + \Delta d) \sin \theta$. As an example, figure 4.5 shows (a) the change of E along streak 22 indicated in figure 4.2 and (b) the resulting d -values. The reference point has been chosen at $\theta = 5.71^\circ$ where the respective d -value at this position satisfies a set of integer values of Miller indices using the lattice parameter of undeformed Nickel. At this point, the reference d -value was found to equal 1.285 \AA . Between angles 5.6° and 5.68° , figure 4.5 (a) shows a constant deviation of energy by $\Delta E \approx -150 \text{ eV}$ less than what was expected according to Bragg's law (red graph). This behavior could be explained by the constant aberration in d from its reference value by $\Delta d = 0.006 \text{ \AA}$ within this angular range as shown in (b). In the range $5.71^\circ < \theta < 5.82^\circ$, ΔE fluctuate between 0 and -250 eV, accumulate with a fluctuation of Δd between 0

and 0.01 \AA . In the third part of the streak ranging between 5.82° and 5.95° , ΔE increased from about -100 eV to 300 eV while Δd decreased from 0.005 \AA to -0.02 \AA .

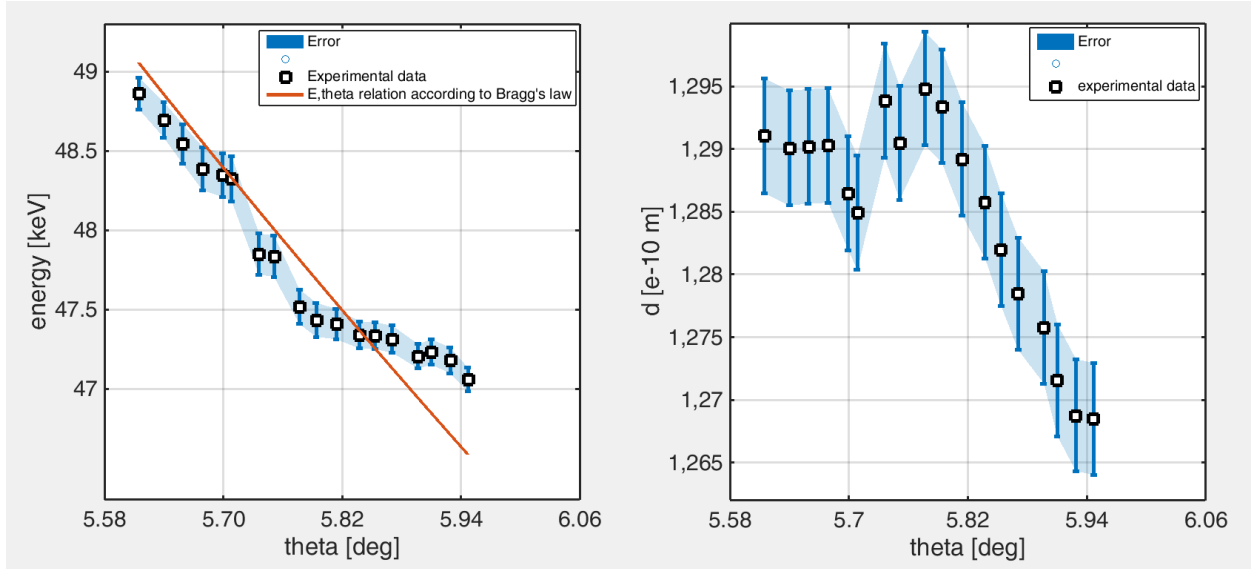


Figure 4.5: (a) Change of energy with angle along streak 22 where the red plot is how should be the change of energy with angle according to Bragg's law. (b) Is the interplanar distance d along the streak calculated from the measured energies and angles given in (a)

4.2 Indexation and grains identification

Using the pnCCD, Laue spots were characterized by intensity $I(y, z, E)$ given in terms of the horizontal and vertical peak position within the detector plane (y, z) and the peak energy, E . The pixel position $(y_0, z_0) = (192, 192)$ indicates the primary beam incident parallel to the y axis. The Bragg angle, θ , is determined by $\theta = r/2L$ where $L = 78(\mp 2) \times 10^{-3} \text{ m}$ is the sample to detector distance and $r = \sqrt{(y - y_0)^2 + (z - z_0)^2}$ is the distance between a spot position at (y, z) and the incident beam position at (y_0, z_0) . The energy profile of each spot is fitted by a Gaussian in order to find the exact E , and its FWHM, ΔE . The Laue patterns from the bulk part were used to calibrate the experimental setup parameters, specifically, the relation between the sample and detector coordinates as frames of reference. After calibration, the first part of data analysis procedure

(indexation and grain identification) was applied. Knowing E and θ one can determine the d-value from the Bragg equation:

$$d_{hkl} = \frac{hc}{2E \sin \theta}, \quad (4.1)$$

where h is the Planck's constant and c the speed of light. Since the lattice parameter, a , of cubic Nickel is known ($a = 3.52 \text{ \AA}$) and d-value has been found, the square of Miller indices can be found:

$$H^2 = h^2 + k^2 + l^2 = \left(\frac{a}{d_{hkl}}\right)^2. \quad (4.2)$$

Once H^2 is determined, all possible combinations of hkl for each reflection can be listed taking into account the fcc structure of Nickel in which the three indices should be all even or odd. In order to find which Miller indices from the listed combinations is the correct, and to which grain each reflection belongs, the angle ϕ_{ij} between two different reflections i and j should satisfy the relation:

$$\cos(\phi_{ij}) = \frac{h_i h_j + k_i k_j + l_i l_j}{\sqrt{h_i^2 + k_i^2 + l_i^2} \sqrt{h_j^2 + k_j^2 + l_j^2}}. \quad (4.3)$$

This procedure was applied to the 38 Bragg reflections measured leading to an indexation and identification of 29 reflections classified to nine grains. As an example, peaks numbered by 7, 35 and 38 correspond to Miller indices $(-2 \ 0 \ 2)$, $(-1 \ 1 \ -3)$ and $(4 \ 0 \ 0)$ are generated by grain 4. All identified spots with their energies, Bragg angles and the corresponding grains are listed in the

first four columns of table 4.1. The numbers used to identify the spots in column 2 are the same in figure 4.2. The obtained interplanar distances, d , as well as the Miller indices hkl of all identified reflections are also listed in columns 5 and 6, respectively. The highest Schmid factor in each grain is also shown in the last column. The calculation procedure of the Schmid factor will be shown in the next section.

Grain	Spot number	E (keV)	Θ (deg)$\pm 0.03^\circ$	$d(\text{\AA})$	Index hkl	Max. Schmid factor(m)
1	1	55.45(24)	6,05	1,061(2)	-3 -1 -1	0.419
	13	67.81(31)	4,1	1,272(3)	-2 0 -2	
	33	53.63(23)	5,2	1,275(3)	-2 -2 0	
	36	39.09(20)	8,95	1,021(2)	1 1 -3	
2	2	55.81(24)	4,9	1,292(3)	-2 -2 0	0.403
	6	56.63(25)	6,15	1,021(2)	-1 -1 3	
	32	58.90(25)	6,67	0,903(2)	0 4 0	
3	3	81.33(34)	5,2	0,841(2)	2 -4 0	0.401
	15	53.52(21)	4,17	1,595(3)	0 -2 0	
	31	80.91(35)	5,29	0,831(2)	4 -2 0	
4	7	60.52(21)	4,71	1,654(3)	-2 0 2	0.372
	35	68.34(26)	5,25	0,990(2)	-1 1 -3	
	38	92.16(37)	4,51	0,855(2)	4 0 0	
5	8	66.33(25)	3,05	1,750(4)	-2 0 0	0.418
	11	67.07(27)	4,25	1,245(3)	-2 -2 0	
	14	64.46(25)	3,22	1,712(4)	2 0 0	
	27	64.23(24)	4,38	1,261(3)	2 0 2	
6	9	77.14(31)	2,7	1,710(4)	0 0 2	0.402
	20	48.87(23)	5,75	1,264(3)	-2 0 -2	
	22	48.41(23)	5,71	1,285(2)	2 0 2	

7	12	93.21(37)	2,21	1,725(4)	-2 0 0	0.438
	17	81.97(33)	3,51	1,231(3)	-2 0 -2	
	21	91.25(36)	3,1	1,250(3)	-2 2 0	
8	16	90.43(35)	3,84	1,021(3)	-1 1 3	0.465
	28	43.62(22)	4,69	1,735(4)	0 -2 0	
	34	77.91(28)	5,13	0,881(2)	0 4 0	
9	18	46.32(23)	4,5	1,702(4)	-2 0 0	0.428
	24	51.31(24)	4,05	1,711(3)	2 0 0	
	30	69.82(26)	6,31	0,803(2)	1 -3 -3	

Table 4.1: Classification of 29 Laue spots in 9 grains (columns 1 and 2). The Bragg energy, Bragg angle and the interplanar distances for each spot are shown in columns 3, 4 and 5, respectively. The calculated Miller indices are shown in column 6 while in column 7 the maximum Schmid factor for each grain is presented.

4.3 Determination of grain orientation and Schmid factors

After verification of the lattice parameters of a particular grain the respective reciprocal basis vectors are calculated in two coordinate systems, namely the laboratory (lab) and the crystal coordinate system (cry). In the crystal coordinate system, the reciprocal lattice vector G_{hkl} is

$$\vec{G}_{hkl} = h\vec{b}_1 + k\vec{b}_2 + l\vec{b}_3, \quad (4.4)$$

where b_1 , b_2 and b_3 are the basic vectors of reciprocal lattice. Taking the geometry shown in figure 4.1 into account, wave vectors of incident and diffracted beam are defined as:

$$\vec{k}_i = \frac{2\pi}{\lambda} \begin{pmatrix} -1 \\ 0 \\ 0 \end{pmatrix} \quad (4.5)$$

$$\vec{k}_f = \frac{2\pi}{\lambda} \begin{pmatrix} x'/s \\ y'/s \\ z'/s \end{pmatrix} \quad (4.6)$$

where s is distance between a position of Laue reflection with spatial coordinate (x', y', z') and a coordinate origin (y_0, z_0) , i.e. $s = \sqrt{x'^2 + r^2} = \sqrt{x'^2 + y'^2 + z'^2}$ with $y' = L$, $y' = y - y_0$ and $z' = z - z_0$. The scattering vector in lab coordinate system is defined as

$$\vec{Q}_{lab} = (q_x, q_y, q_z) = \vec{k}_f - \vec{k}_i = \vec{G} \quad (4.7)$$

Substituting equation (4.4) in (4.7):

$$\begin{pmatrix} q_{1x} & q_{2x} & q_{3x} \\ q_{1y} & q_{2y} & q_{3y} \\ q_{1z} & q_{2z} & q_{3z} \end{pmatrix} = \begin{pmatrix} h_1 & h_2 & h_3 \\ k_1 & k_2 & k_3 \\ l_1 & l_2 & l_3 \end{pmatrix} \begin{pmatrix} b_{1x} & b_{2x} & b_{3x} \\ b_{1y} & b_{2y} & b_{3y} \\ b_{1z} & b_{2z} & b_{3z} \end{pmatrix} \quad (4.8)$$

As the \vec{q} vectors for any reflection can be calculated from the experiment geometry (equations 4.5-4.7) and the Laue pattern at this stage is already indexed, the reciprocal lattice vectors \vec{b}_1, \vec{b}_2 and \vec{b}_3 can be determined by solving equation (4.8) using three Laue reflections of a selected grain. Consequently, the real lattice vectors \vec{a}_1, \vec{a}_2 and \vec{a}_3 and their orientations in lab coordinate system could be found using the standard relations between the real and reciprocal vectors. As an example, here we show the deduced orientation matrix of unit cell for grain 4:

$$\vec{a}_1, \vec{a}_2, \vec{a}_3 = \begin{pmatrix} 1.89 & 2.60 & -1.37 \\ -2.12 & -0.05 & -2.87 \\ -2.09 & 2.29 & 1.49 \end{pmatrix}$$

The evaluated lattice parameters: $|\vec{a}_1|, |\vec{a}_2|, |\vec{a}_3| = (3.526, 3.465, 3.512) \text{ \AA}$ and angles $(\alpha, \beta, \gamma) = (89.02^\circ, 88.24^\circ, 90.03^\circ)$ with an error of less than 2%. are in good agreement with the literature values for cubic lattice of Nickel. Similarly, the lattice vectors and their orientations have been found for all other obtained grains.

In order to determine the slip systems which may be excited during uniaxial load, we used the approach introduced by Schmid [75]. The Schmid factor defined as $m = \cos k \times \cos \lambda$ has been calculated for the various slip planes for the selected grains, where k and λ are the angles between the load axis and the slip plane and between the load axis and the slip direction, respectively.

Following Schmid's law $\tau = \sigma \times m$ (τ is the resolved shear stress and σ is the applied external force), the slip system with the highest Schmid factor is activated first followed by slip systems with slightly lower Schmid factors when the resolved shear stress exceeds the critical shear stress τ_c . The slip planes and slip directions which are respectively, $\{111\}$ and $\langle 110 \rangle$ for FCC materials are defining the possible slip systems. In order to estimate the actual angles between the applied stress and the slip plane directions and subsequently the Schmid factors one needs to transform the particular grain from crystal coordinate system into the lab coordinate system where the direction of applied force is defined. Hence, the Euler transformation matrix has to be calculated for every grain such that:

$$\begin{pmatrix} a_{1x} & a_{2x} & a_{3x} \\ a_{1y} & a_{2y} & a_{3y} \\ a_{1z} & a_{2z} & a_{3z} \end{pmatrix}_{lab} = Euler. \begin{pmatrix} a_{1x} & a_{2x} & a_{3x} \\ a_{1y} & a_{2y} & a_{3y} \\ a_{1z} & a_{2z} & a_{3z} \end{pmatrix}_{cry} \quad (4.9)$$

The detailed procedure to determine the Euler transformation matrix can be found in *Abboud et. al 2017* [4].

4.4 Grain selective structural changes under a tensile load

Once the Laue spots indices were found and grains were identified, the response of each grain has been studied individually. As an example, the analysis of the three Laue spots from grain 4 (spots 7, 35 and 38 in figure 4.2) is presented. Based on the procedure discussed in section 4.3, the Schmid factors of the 12 possible slip systems of grain 4 were calculated and shown in table 4.2.

Slip system	1	2	3	4	5	6
Plane	(111)	(111)	(111)	($\bar{1}11$)	($\bar{1}11$)	($\bar{1}11$)
Direction	[$\bar{1}01$]	[$0\bar{1}1$]	[$\bar{1}10$]	[101]	[$0\bar{1}1$]	[110]
Schmid factor	-0.015	0.384	-0.399	0.014	0.006	0.008
Slip system	7	8	9	10	11	12
Plane	($\bar{1}\bar{1}1$)	($\bar{1}\bar{1}1$)	($\bar{1}\bar{1}1$)	(11 $\bar{1}$)	(11 $\bar{1}$)	(11 $\bar{1}$)
Direction	[011]	[110]	[$\bar{1}01$]	[$\bar{1}10$]	[101]	[011]
Schmid factor	0.413	0.472	-0.013	-0.022	0.043	0.023

Table 4.2: Schmid factors of 12 slip systems for grain 4

While spots 7 ($\bar{2}02$) and 38 (400) are spatially confined (figure 4.6 a, b) with one energy peak, reflection 35 ($\bar{1}1\bar{3}$) is streaked, extending spatially over a 2θ range [0.083 0.102] radians (figure 4.6 c). At different positions along the streak a unique energy spectrum is calculated and a different lattice d-spacing is found as the case shown in figure 4.5 (b). Streaking of the Laue spots indicate the onset of lattice rotation governed by the rotation of the grain under constrained tensile loading. Examining the streak spectral distribution (E vs θ) one can determine whether lattice rotation takes place while the lattice spacing remains constant or not. Changes in the grain orientation and lattice spacing is facilitated by the activation of particular slip plane with maximum resolved shear

stress. In case of two or more competing slip systems, the peak generally follows the resultant path.

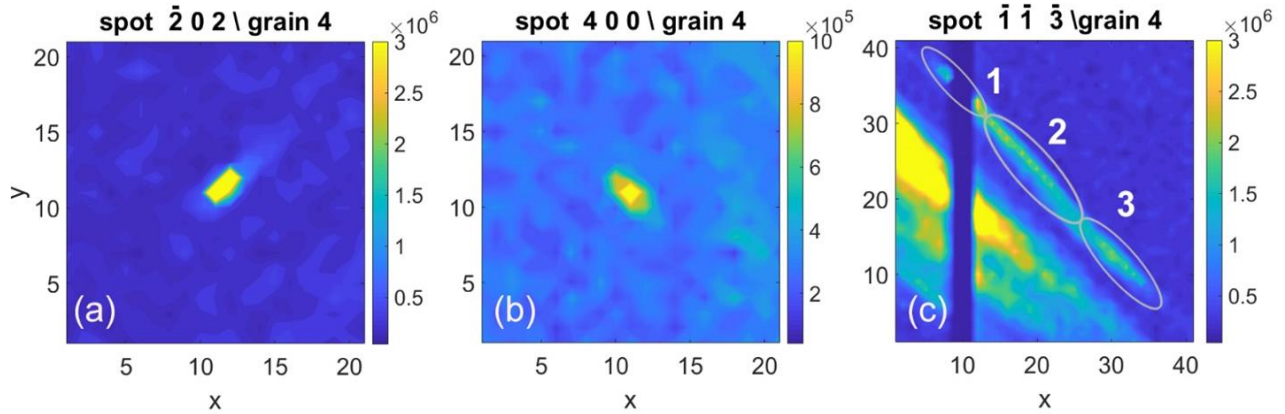


Figure 4.6: 3 Laue spots from grain 4. The $(\bar{2}02)$ (a) and (400) (b) spots are sharp with a single energy peak, while the $(1\bar{1}\bar{3})$ (c) spot is streaking with a distribution of energy along its length and different value of lattice spacing d .

Based on the orientation of grain 4 and the external load direction the Schmid factor with the highest value corresponds to the $(1\bar{1}1)$ slip plane in the $[110]$ slip direction with a value of 0.472. Figure 4.7 shows a sketch of the unit cell, the measured diffraction planes and the slip plane with the highest Schmid factor $(1\bar{1}1)$. The pronounced streaking seen in the Laue spot of plane $(\bar{1}\bar{1}\bar{3})$ can be attributed to its relative orientation with respect to the slip plane. While plane $(\bar{1}\bar{1}\bar{3})$ makes an acute angle ($\sim 30^\circ$) with respect to the slip plane, both the $(\bar{2}02)$ and (400) planes are $\sim 90^\circ$ and $\sim 60^\circ$ respectively, making them resist slipping.

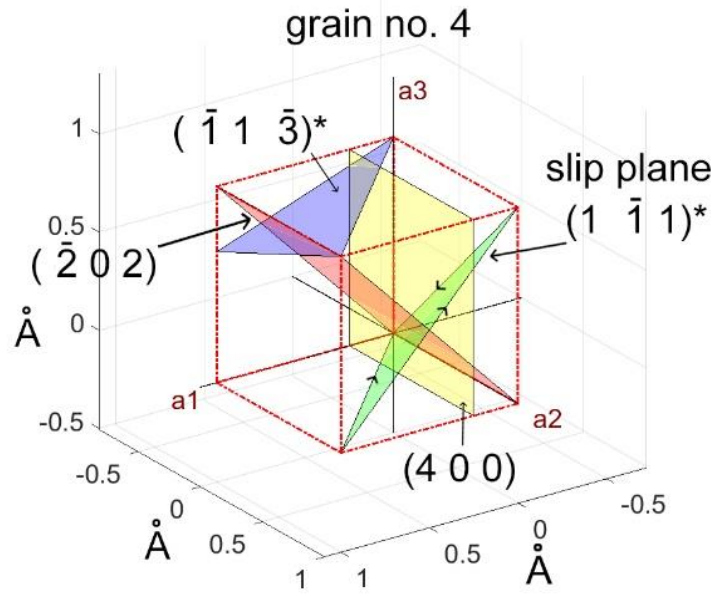


Figure 4.7: Schematic drawing of grain 4 unit cell with the planes corresponding to the three collected reflections plotted alongside the most probable slip plane $(1\bar{1}1)^*$. This figure shows graphically that the plane $(\bar{1}1\bar{3})^*$ is easier to slide given the slip plane is activated.

The sample has been exposed to tensile loading with displacements of 0, 40, 80, 120 and 200 μm corresponding to 0, 0.2, 0.4, 0.6 and 1% engineering strain along the Ni wire main axis. The Laue patterns after each stretch are shown in figure 4.8 (a). This deformation procedure caused the Laue spots to streak. Before applying any load, the Laue spots show a distribution of streak length magnitudes. Figure 4.8 (b) shows that the majority of spots have streaked by less than 0.0087 rad (first bin). At 40 μm and above, the average streak length increases (first bin counts drop) and the distribution starts to “spread” to higher bins. At this point, and independent from the spectral distribution of the spots, one can say that, the spread indicates the presence of lattice rotation.

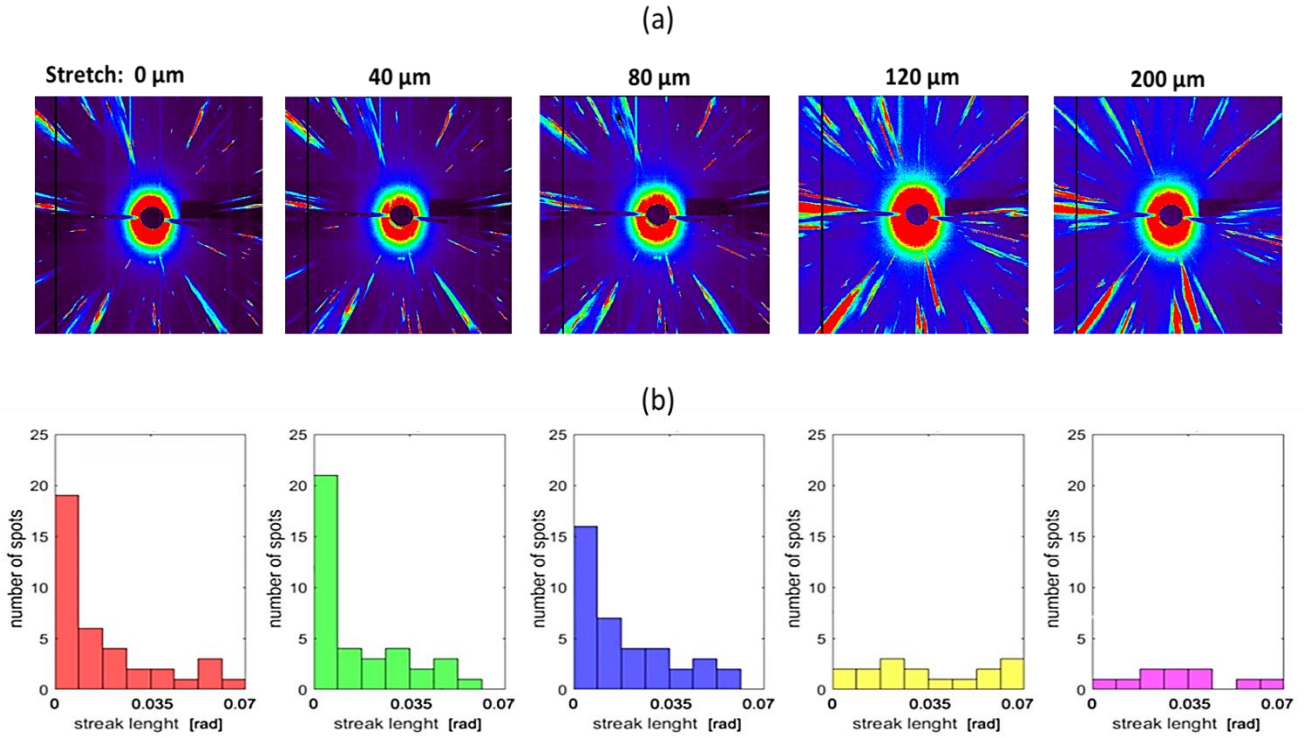


Figure 4.8: (a) Laue pattern from the gauge section of the nickel wire as function of external stretch. (b) Histogram of streak length in radians for all collected spots at 5 different tensile strain steps. The streak length increases with larger strains.

For every pair of (E, θ) along the streak a lattice spacing value can be calculated according to Bragg's Law. The distribution of d along the Laue spot length is plotted in figure 4.9 for reflections $(\bar{1}1\bar{3})$ (grains 4) at each stretching step. The distribution of d along the streak length attributes to strain inhomogeneity within a grain. In term of d -distribution, two regions can be distinguished: the edges of the streak and its center. At the edges, maximum deviation from a mean value of d is detected. During deformation the internal of the grain is more stable as the mean value does not change much in comparison with the edges.

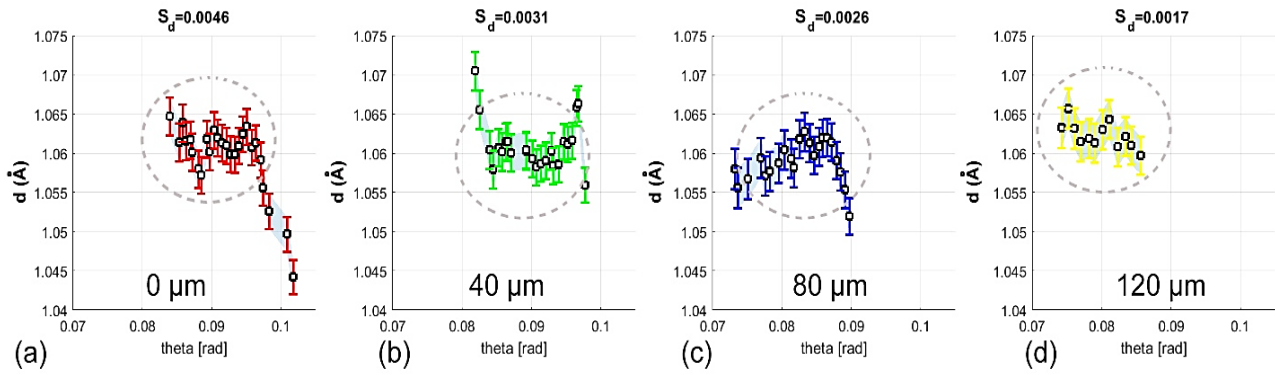


Figure 4.9: changes in the lattice spacing of $(\bar{1}1\bar{3})$ planes of grain 4 at sample elongations 0 to 120 μm . Above each figure the distribution width S_d is seen to decrease with each elongation step. Maximum variation of the change is visible at the edges of the Laue spot.

The standard deviation S_d measures the spread of d from the mean value. During deformation, S_d drops from 0.0046 to 0.0017 \AA , almost 3 times indicating a relaxation process. The used standard deviation formula in terms of lattice spacing is given by:

$$S_d = \sqrt{\frac{\sum (d - \bar{d})^2}{n}} \quad (4.10)$$

where n is the number of measured points along a streak. The mechanics of deformation is a combination of rotational motion (change in the position of the reflection) and strain (change in the lattice spacing). Different lattice spacings along a single streak are attributed to an inhomogeneous lattice strain across the grain.

The same analysis was performed on all 38 reflections. The $(E, \theta)_{hkl}$ relation was calculated and the $(d, \theta)_{hkl}$ as well. The distribution of the d -values was found from S_d . At each loading step, the histogram of S_d was calculated and the results are summarized in figure 4.10. The decaying histogram, seen as a spread of the S_d to larger values, indicates higher variations in internal grain strain. For the 120 and 200 μm deformation plots, Laue spots become large and start to overlap

making it hard to distinguish single peaks. In contrast to the average response of the measured volume, the plane $(\bar{1}1\bar{3})$ shows an opposite response. At higher loading steps, S_d decreases (figure 4.11). In fact, the mean value of d remains the same but the standard deviation is reduced. This response shows that the local change of particular planes may differ significantly from the average response of the material depending on local conditions.

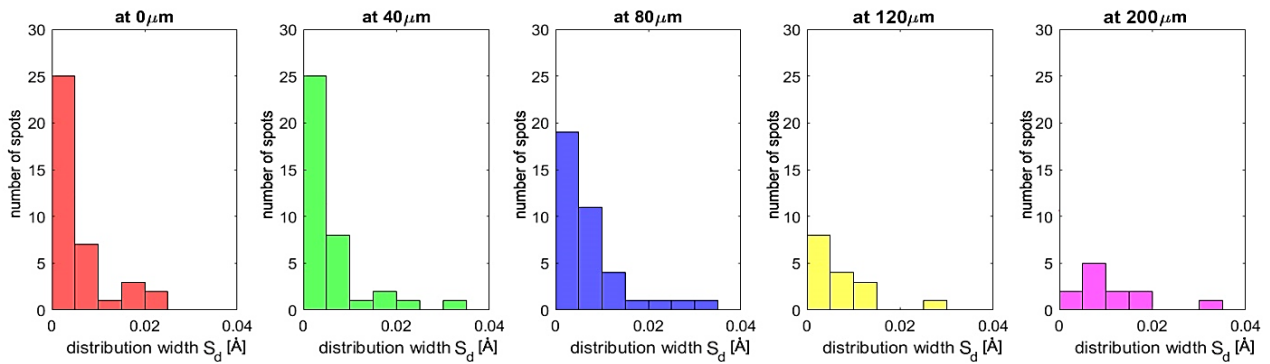


Figure 4.10: Distribution of S_d [Å] at each loading step for all 38 reflections. As the external loading increase, the spread of d increases

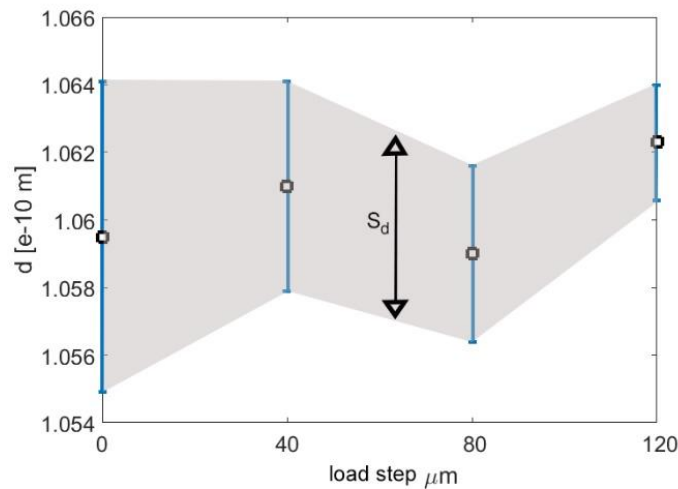


Figure 4.11: Distribution of S_d at each loading step for spot 35 $(\bar{1}1\bar{3})$. With loading step the spread of d decreases. This behaviour is opposite to the average response of the measured volume of the sample shown as in figure

4.5 Discussion

The initial state of the Ni sample already indicates plastic deformation probably caused by sample preparation and sample mounting. This is of course not an ideal initial state to analyze deformation mechanisms under external perturbation, however, the sample still serves the intended purpose to show the capability of the technique. Hence, the aim of the work shown in this chapter is rather to introduce to the huge power of the energy-dispersive Laue technique than thorough analysis of the deformation behavior of the particular Nickel microwires.

In the as-prepared state, Laue peak streaking towards the center of the detector is observed. This can well be explained by the used energy and transmission geometry, favoring streaking towards the direct beam. The observed streaking is different than the one observed in standard micro Laue diffraction setups [76-79]. A standard analysis of spot streaking directions is therefore not useful here.

In contrast, the spectral analysis of the Laue spot energy offers unprecedented opportunities in data treatment. We exploit this energy resolution by measuring the local lattice spacing (hence, strain) and lattice strain distributions. First, we follow the lattice spacing of one specific Laue streak. It indicates local elastic strain inhomogeneity along the Laue peak. To further discuss the origin of the local variations in lattice spacing it is important to note, that the diffraction signal measured at the detector stems from the entire illuminated grain. Hence, the inhomogeneous lattice spacing as shown in figure 4.9 is representative for the inhomogeneous distribution of lattice strains across a single grain in the polycrystalline matrix. Such strain inhomogeneities arise from the local environment, e.g. neighboring grains and their orientation, phases, triple junctions, twins and *et cetera* [80-82]. Since the technique provides Laue diffraction spots of many grains simultaneous the described technique allows for a high throughput characterization tool which can be used to calibrate material models used for instance in crystal plasticity and finite element modelling [83]. The advantage of this technique is that the single grain properties of a severely deformed crystallite embedded in the often-complex matrix can be used for calibration. Within this study we used a relatively large x-ray beam which prevents an analysis of the local grain environment. However, with smaller x-ray beam sizes we will be able to identify the local environment as well.

Due to its high throughput capability the technique can easily be used to scan an entire sample and analyze the lattice strain distribution across the entire sample. At low applied deformation (40 μ m and lower), the samples clearly show a small variation in observed lattice strains. However, during ongoing deformation the lattice strain distribution spreads. The spread can be explained by the random orientation of grains and measured reflections – which in some cases are aligned perpendicular to the straining axes and in others parallel. Hence, an overall increase of lattice strain distribution can be observed. Due to the full crystallographic information the method can provide orientation dependent strain distributions, which might be very beneficial to directly measure the strain heterogeneity of materials with huge anisotropy (e.g. hexagonal materials like Mg).

5 PnCCD coupled to CsI(Tl) scintillator

Most charge coupled devices (CCDs) are made of silicon (Si) with typical active layer thicknesses of several microns. In case of a pnCCD detector the sensitive Si thickness is 450 μm . However, for silicon-based detectors the quantum efficiency for hard X-rays drops significantly for photon energies above 10 keV. This drawback can be overcome by combining a pixelated silicon-based detector system with a columnar scintillator. In this chapter we report on the characterization of a low noise, fully depleted 128x128 pixels pnCCD detector with $75 \times 75 \mu\text{m}^2$ pixel size coupled to a 700 μm thick columnar CsI(Tl) scintillator in the photon range between 1 to 130 keV. The excellent performance of this detection system in the hard X-ray range is demonstrated in a Laue type X-ray diffraction experiment performed at EDDI beamline of the BESSY II synchrotron taken at a set of several GaAs single crystals irradiated by white synchrotron radiation. With the columnar structure of the scintillator, the position resolution of the whole system reaches a value of less than one pixel. Using the presented detector system and considering the functional relation between indirect and direct photon events Laue diffraction peaks with X-ray energies up to 120 keV were efficiently detected. As one of possible applications of the combined CsI-pnCCD system we demonstrate that the accuracy of X-ray structure factors extracted from Laue diffraction peaks can be significantly improved in hard X-ray range using the combined CsI(Tl)-pnCCD system compared to a bare pnCCD.

5.1 Spectroscopic imaging of hard X-rays

Imaging of high energy X-ray photons in astronomy, medicine, crystallography and other applications requires imaging systems with high detection efficiency. The proper choice of a particular detector system depends on the energy range of interest, expected signal and background levels, required energy and spatial resolution, and other factors. Silicon (Si) and Germanium (Ge) are examples of 2D solid state detectors with excellent energy resolution and charge transport properties. However, their low quantum efficiency at high energy photons limits their application

for hard X-ray and γ -ray detection (above 10 keV) because of the relatively low atomic number ($Z=14$ for Si and $Z=28$ for Ge) [84]. Furthermore, the small band gap E_{gap} of these two semiconductors – especially Ge with $E_{\text{gap}}=0.68$ eV requires detector operation at low temperatures. Other materials with high atomic number such as Cadmium Telluride (CdTe) and Cadmium Zinc Telluride (CdZnTe) have been considered as promising semiconductors for hard X-ray and γ -ray detection with high quantum efficiency, typically in the range between 10 and 200 keV [80]. A large band-gap energy ($E_{\text{gap}}=1.44$ eV) allows for operation at room temperature. However, the crystal quality of these materials is far below the level achieved with silicon. Problems and the status of development of these compound semiconductor detectors were reviewed in [85]. The quantum efficiency (QE) of a 450 μm thick Si-based detector system reduces to about 1% at 100 keV. A novel X-ray imaging system has been developed recently by PNSensor GmbH in Munich. It is based on a combination of a micro-columnar Thallium doped Cesium Iodide (CsI(Tl)) scintillator with a silicon pnCCD detector [86]. CsI scintillators doped with Thallium (Tl) has a high stopping power for γ – rays compared to Si and Ge due to its high mass density of 4.5 g/cm^3 and high atomic number of $Z_{\text{Cs}} = 55$ and $Z_{\text{I}} = 53$. It has a high light yield of about 60 photons/keV [87] and its emission spectrum is in the visible range with a peak maximum located at about 550 nm [46]. Figure 5.1 shows the QE of a pnCCD (Si) and for CsI(Tl), each having a thickness of 450 μm and 700 μm , respectively. It becomes obvious that the combination of both materials will enlarge the usable range of high QE towards 100 keV and beyond.

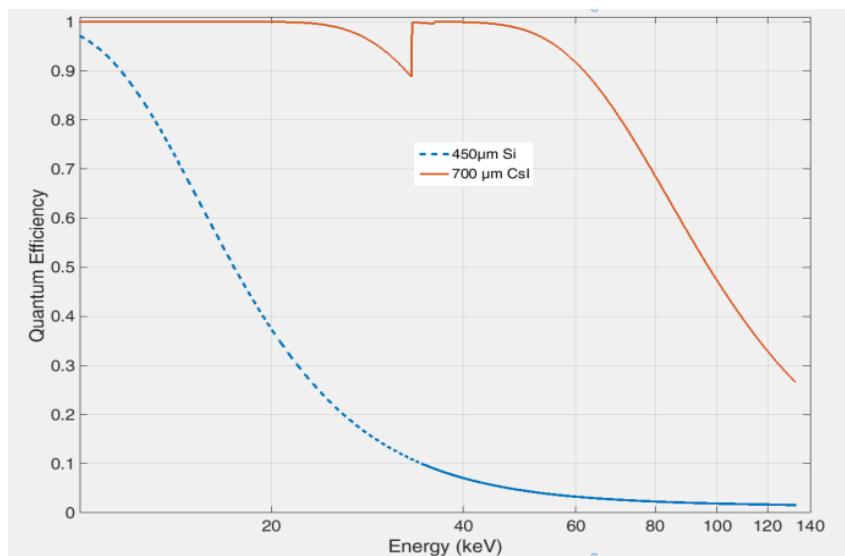


Figure 5.1: Quantum efficiency of a 450 μm Si, and for 700 μm of CsI(Tl).

5.2 Configuration of the combined system and the detection process

The growth of large area micro-structured Cesium Iodide scintillators has been improved over the past years. They are commercially available from various vendors with active areas up to $40 \times 40 \text{ cm}^2$. The columnar CsI scintillator utilized in this chapter originates from Hamamatsu [88]. With its structure, columnar CsI scintillator has the capability to channel scintillation light towards the exit surface through total internal reflections, reducing the divergence of visible photons emitted from the scintillator back to the silicon photon detector. In addition, this structure helps to reduce the depth of interaction dependent blurring, and results in a narrow spatial resolution. As schematically shown in figure 5.2, the scintillator with a size of $10 \times 10 \times 0.7 \text{ mm}^3$ is attached to the back side of a $450 \mu\text{m}$ thick pnCCD through a $50 \mu\text{m}$ thin silicone protection pad covered with an optical grease.

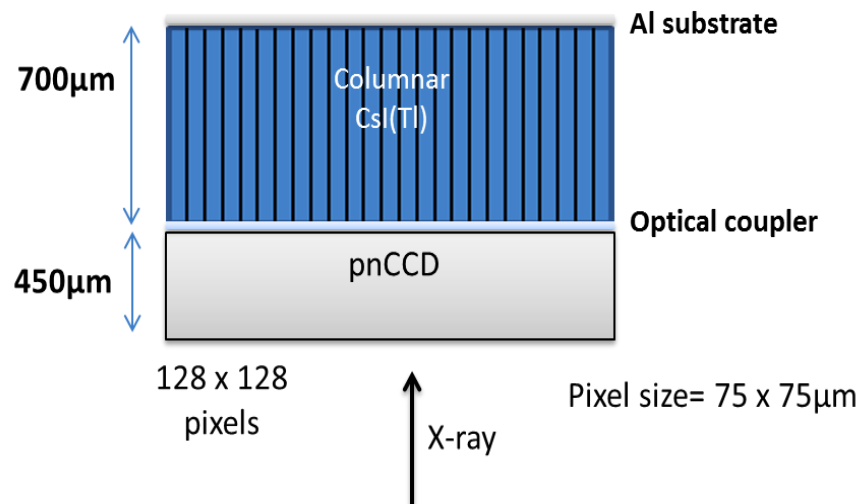


Figure 5.2: The structure of the detection system. In this configuration the detector is front illuminated (pixels side), the low energetic photons below 15 keV are almost totally absorbed by the CCD. X-rays with higher energies are stopped by scintillator

The fully depleted pnCCD operates by front side illumination through the shift register structure, while the scintillator is coupled to the non-structured, homogeneously sensitive back side of the pnCCD. The back-illumination geometry of the system gives the pnCCD a high capability to absorb all incident photons with energies between 0.5 and 15 keV within the silicon chip “direct”,

whereas X-ray photons of higher energy traverse the silicon and reach the CsI(Tl) layer, generating optical photons where a significant number is back reflected and absorbed by the silicon sensor and allow for “indirect” X-ray detection. In our synchrotron experiments we used a test pnCCD with 128x128 pixels operated in a frame store three-phase transfer mode. Structure and function of the system were tested by radioactive sources and the results are discussed in details in [86].

When X-rays impinge on the pnCCD they convert their total energy to free charge carriers and heat. As mentioned in chapter 1, although the band gap energy of Silicon is $E=1.12$ eV, the mean energy needed to generate an electron-hole pair is 3.67 eV. The generated electrons are directly guided to a low capacitance readout node. This leads to a lower physical limit of the measurable energy resolution in Silicon at 10 keV to be $\text{FWHM} = 153$ eV (at noise threshold $\sigma=5.5 e^-$).

At the scintillator level, X-rays hitting the CsI material are equally exciting electrons from the valence to the conduction band or to the activator states of the dopants, here Tl. They recombine through the activator levels in forbidden band gap emitting a photon with a wavelength of 550 nm [10]. The photons are isotropically radiated from their position of generation but a significant number of them is back reflected towards the silicon photo-detector. Those photons that do not reach directly the photo-detector and do not match the total reflection conditions of the scintillator-pnCCD system are lost. The quantum efficiency for the optical photons in the radiation entrance window of the pnCCD, including the absorption in the separating silicon pad and the optical grease is approximately 85% for photons coming from the scintillator.

Comparing the two detection processes of pnCCD and CsI(Tl) one can conclude that: (1) 273 signal electrons per keV photon energy deposited in the silicon of the pnCCD are delivered while (2) we get 51 (experimental value in this work is 47) electrons per keV from the CsI signal, at the same incident energy. The direct conversion in the Silicon leads to a 5.4 (experimental value in this work is 5.8) times higher output signal compared to the indirect signal from the CsI [86]. But the very important difference between the two detection schemes for our application in crystallography is the 45% quantum efficiency at 100 keV of the CsI(Tl) compared to less than 1% for silicon. In this sense the physical properties of CsI and Silicon as hard X-ray detectors are complementary and extend the excellent performance of bare silicon towards hard X-ray range.

5.3 Laue Diffraction Experiment

The number of the signal electrons generated by the direct and indirect events as well as the energy resolution of the system will be investigated in this section by means of an energy-dispersive Laue type diffraction experiment. Aiming to produce multiple monochromatic X-ray sources illuminating the detector in a single measurement, multiple randomly oriented GaAs [111] wafers with thickness of 300 μm were attached together and illuminated by a white spectrum of high energy X-ray radiation. Due to their random orientation, it produces a large number of Laue spots of very different photon energy simultaneously. Figure 5.3 shows the setup of the experiment performed at the EDDI beamline of the storage ring BESSY II in Berlin. The beamline provides white synchrotron radiation ranging from 1 up to about 130 keV (see section 4.1). Two perpendicular slits allow for collimating the beam to a size of $100 \times 100 \mu\text{m}^2$. The bunch of GaAs samples were mounted at a distance of 20 mm apart from the sensitive area of pnCCD and were kept at a room temperature. In order to operate the detector in the so called single photon counting mode [53], the primary beam was attenuated by 11 cm of Aluminum (Al) to reduce the X-ray flux.

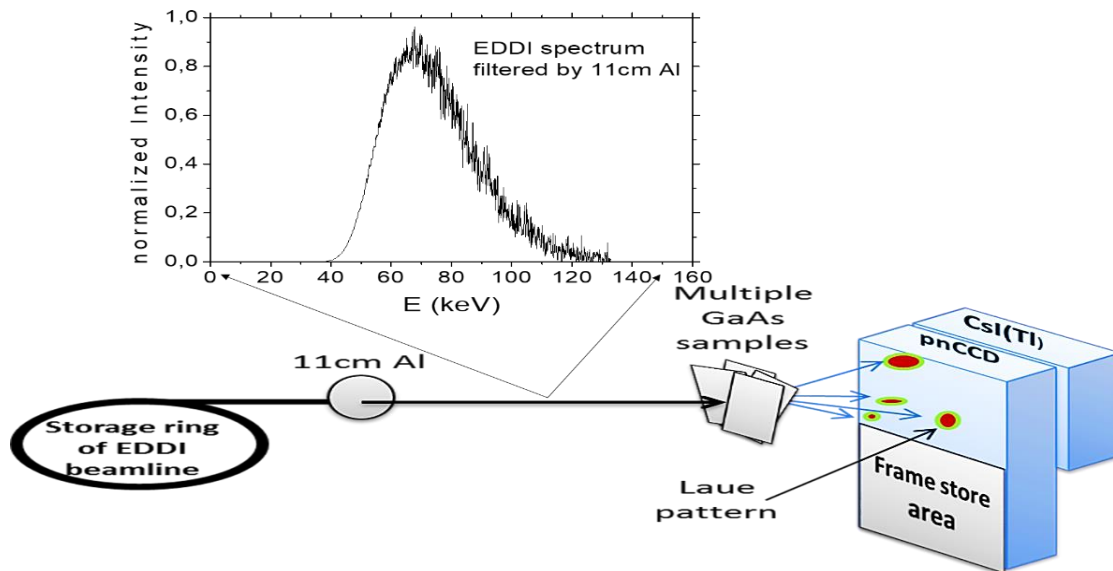


Figure 5.3: Laue diffraction experiment setup at EDDI beamline of the storage ring BESSY II in Berlin. The white spectrum used for the experiment is tailored by setting a 11cm thick Al absorber in front of the sample.

In this setup the average count rate was about 33,300 events /s recorded with a frame rate of 370 Hz. The presence of the Al absorber cuts off the low energetic photons of the incident beam generating an incident spectrum ranging from 40 to 140 keV. The energies of Cs and I K- $\alpha_{1,2}$ lines were used to calibrate the pnCCD channels from analog to digital unit (ADU) to energies. More details about the calibration will be discussed later in section 5.4. The photon events were extracted from the raw data using an event detection threshold of 4σ , where $\sigma=5.5 e^-$ is the equivalent noise charge in the selected gain mode of the detector including thermal and electronic noise components.

5.4 Detection and conversion efficiency of X-rays in Si and CsI(Tl)

According to the discussion in section 3.3.1, the signal charges generated by the directly detected photons are collected by the pnCCD either in one pixel (single pixel events) or distributed over neighboring pixels (double, triple and quadruple pixel events). These split events occur if the landing point of the generated electron cloud with respect to the pixel boundaries is located close to the corner of a pixel. Below 10 keV the charge cloud radius generated by a single X-ray photon is in the order of 10 μm (r.m.s). However, in the indirect detection case, the cloud is the sum of many scintillation photons detected as one event, resulting in cloud size that typically spreads over more than 10 pixels. The different signal cloud radius can be used to distinguish between direct and indirect events.

The complete direct and indirect Laue patterns of GaAs samples recorded by the pnCCD are shown in figure 5.4. Both of the intensity images shown are results of integration of over 10^6 single frames allowing for the spectral analysis of all spots based on sufficient photon statistics. The conversion homogeneity of the detector area was tested by tracking a single pattern over the whole sensitive area. It has been shown that the same signal value fluctuates at each scan step with an average standard deviation of 0.3% for the direct signal and 1.5% for the indirect signal where the largest deviation of the indirect signal is found near the boundaries of the detector (5 pixels beside the boundaries). The latter is due to the fact that a part of the scintillation photons can escape the CsI-pnCCD interface which is reducing the size of the photon cloud measured in the pnCCD. In the blue marked areas of the images shown in figure 4, air has been trapped between the pnCCD and

the optical pad, so that the transmission of scintillation photons through the interface into the pnCCD is reduced to $\sim 70\%$ compared to the remaining parts of the interface. This air inclusion disappeared after two days of vacuum of 10^{-6} mbar. Because of the different energy and the different pixel size covered by the clouds of direct X-ray photons on one hand and indirect scintillator photons on the other hand one can create separate Laue pictures of direct (a) and indirect (b) events. As shown in figure 5.4, most of the spots are detected directly and indirectly at the same time. Nevertheless, some other spots cannot be identified properly in the direct Laue pattern because of the low QE of Si above 90 keV (QE about 1%) but they clearly appear in the indirect event pattern

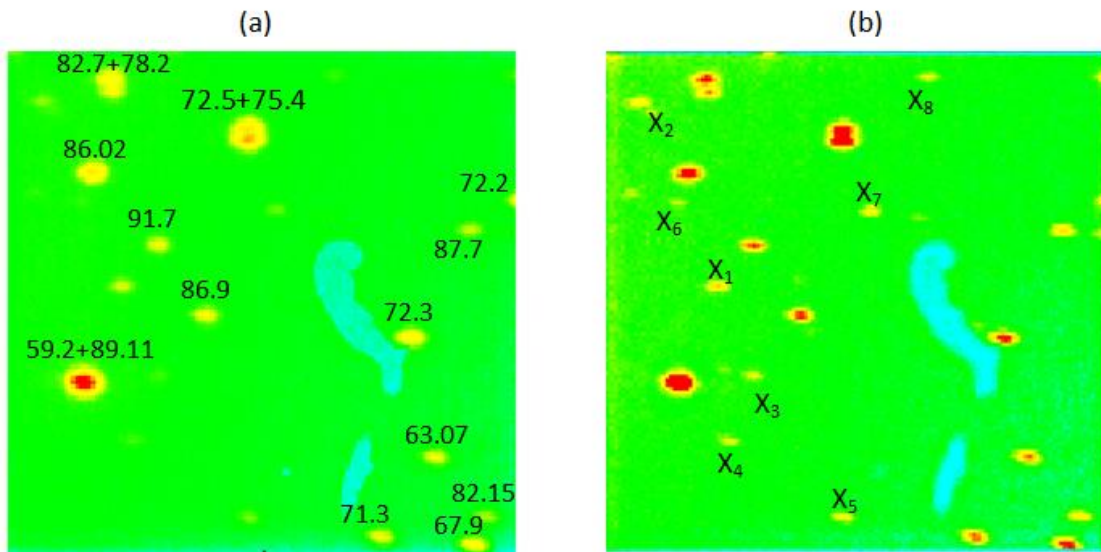


Figure 5.4: Integrated intensity image from the detector system (128x128 pixels) including Laue spots with their (a) direct and (b) indirect energies.

Few high energy spots denoted by “ X_i ” in figure 5.4 (b) could not be detected directly by the pnCCD or they were detected but with very low count rate which is not sufficient for accurate analysis. However, as discussed in section 5.2, these high energy photons transmit through the silicon chip and interact with CsI(Tl) and the scintillation photons are then detected by pnCCD with a QE of about 45% at an X-ray energy of 100 keV.

In order to determine the energy of the incoming photons that detected indirectly, one needs to find the relation between the generated indirect signal and the incoming energy. The mean number of signal electrons, \bar{N}_e , generated by an incident X-ray photon with energy, E, after an interaction in Si or in CsI(Tl) is given by [50]:

$$\bar{N}_e^{dir} = \frac{E}{w_{Si}} \quad (5.1)$$

for Si, and

$$\bar{N}_e^{indir} = \frac{E}{w_{CsI}} \cdot \bar{T} \cdot \bar{\eta} = \bar{N}_{eh} \cdot \bar{T} \cdot \bar{\eta} \quad (5.2)$$

For CsI (Tl). Here $w_{Si} = 3.67$ eV is energy required to create the electron-hole pair in Si, $w_{CsI} = 14$ eV is the mean energy to create an eh-pair in CsI, \bar{N}_{eh} is the mean number of eh-pairs created in CsI, \bar{T} is the mean conversion efficiency of eh-pairs inside the scintillator into scintillation photons and $\bar{\eta}$ is the mean conversion efficiency of scintillation photons into signal electrons.

The values of \bar{N}_e^{dir} and \bar{N}_e^{indir} were calculated from equations 5.1 and 5.2 for the energy range of 35 keV up to 130 keV where $T = L \times w_{CsI} = 60$ photons/keV \times 14 eV = 0.84, where L is the light yield of CsI(Tl), and $\eta = 0.78$ [16]. The calculated values of N_e were plotted with the measured values at several energies ranging between 57 and 90 keV shown in figure 5.5.

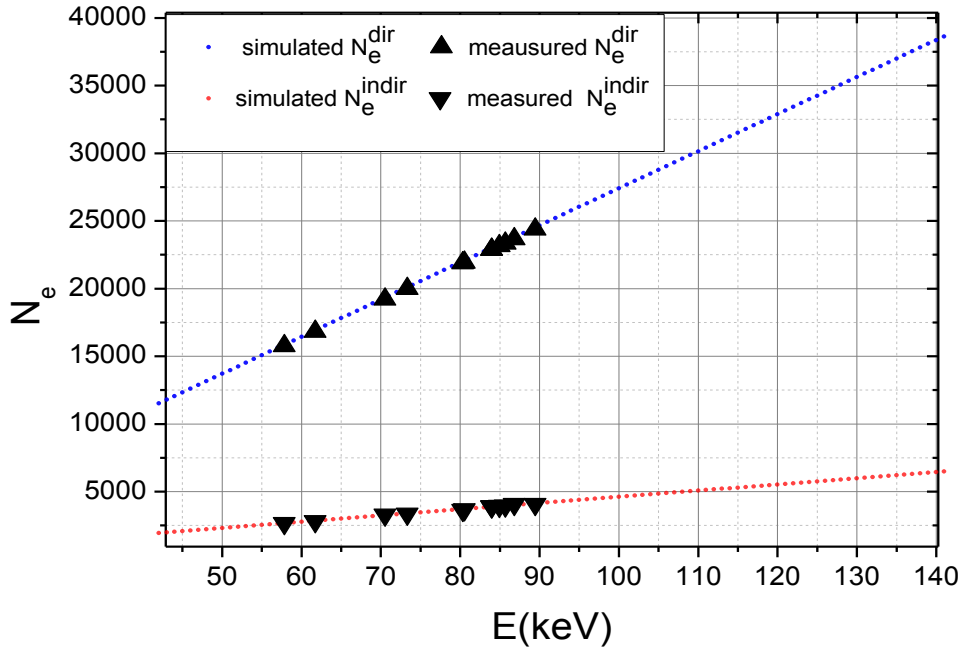


Figure 5.5: Number of signal electrons generated by direct and indirect event for several X-ray energies. The measured values are also linear fits to the measured data

In contrast to the low QE of Si in the hard X-ray energy range, the conversion of the X-ray energy into signal electrons is more efficient in Si compared to CsI(Tl). This circumstance leads to a higher “signal to noise” ratio, and hence a better energy resolution for directly detected X-rays inside the pnCCD.

As the number of the generated indirect signal electrons per keV is known (fig. 5.5), A linear relation between the measured indirect ADU signal and incident energy can be extracted. For example, if two spots are detected directly at energies of 61.7 and 73.3 keV and at the same time they create 2806 and 3358 electrons respectively as indirect signals, these

<i>Spot X_i</i>	<i>Incident energy (keV)</i>
X_1	99.78
X_2	126.54
X_3	111.7
X_4	107.53
X_5	95.56
X_6	117.39
X_7	112.46
X_8	107.6

Table 5.1: Energies of the spots X_i (detected indirectly) shown in figure 5.4 (b)

values can be used to define a relation between the measured indirect signal and the corresponding direct energy. Subsequently, any indirect signal can be referred to its corresponding incident photon energy even if the direct signal is not detected. By this way the incident energies of the spots marked in Fig.5.4 (b) by X_i has been found and listed in table 5.1.

5.5 Energy Resolution for direct and indirect events

The photons registered in the pnCCD can be approximated by a Gaussian energy distribution with a FWHM defined in equation (3.8), while for the indirect signal from CsI(Tl) scintillator the relative energy resolution is given by [50]:

$$R = \frac{FWHM}{E} = 2.35\sqrt{v(N_e)} \approx 2.35 \sqrt{\frac{F_{CsI}}{\bar{N}_{eh}} + v(T) + v(\eta) + \frac{1 - \bar{T}\bar{\eta}}{\bar{N}_e} + \frac{ENC_{el}^2}{\bar{N}_e^2}} \quad (5.3)$$

where $v(N_e)$ is the relative variance of the measured signal electrons, $F_{CsI} = 0.28$ is the Fano factor in CsI, $v(T)$ and $v(\eta)$ are the variances of the efficiencies T and η respectively.

For large bulk CsI(Tl) scintillators the relative energy resolution can be approximated by $R = R_T(E = 50 \sim 200 \text{ keV}) \approx 2.35\sqrt{v(T)} = 0.08$ [50]. The FWHM(E) can be determined by $FWHM(E) = R \times E$. Because of the spread of the indirect events over more than 10 pixels, the noise threshold should be as low as possible to prevent the loss of scintillation photons at the event boundaries. In order to determine the direct and indirect FWHM(E) of a Laue spot, direct and indirect events are separated by their event size. In addition, there is a background generated by X-rays, which are Compton scattered in the sample. These Compton scattered X-rays are homogeneously distributed over the pnCCD. The background could be determined by taking a spectrum of an area where no Laue spots are involved and subtracting it from the recorded spot spectrum. Both areas should be of the same size.

An example of a spectrum inside a Laue spot is shown in figure 5.6 (a) (in ADU units), where the indirect peak is located at low ADU channel numbers (low energy) next to its escape peak, while the direct peak is located close to the ADU channel 15,500. Since the whole events with sizes between 1x1 and 10x10 pixels are counted in this spectrum, both direct and indirect events are included. The K- α CsI(Tl) fluorescence peaks each hold two energy lines, K- α_1 and K- α_2 . The iodine peak at 5155 ADU contains signals from the direct conversion of photons with energies of 28.32 keV and 28.61 keV. The cesium fluorescence peak at 5635 ADU holds signals from of 30.63 keV and 30.97 keV photons [89]. These direct fluorescence lines are served for the calibration of the channel numbers for the direct events (from ADU to eV). Figure 5.6 (b) displays the calibrated indirect Bragg peak at 83 keV with FWHM of 14.3 keV (17%) (see inset), whereas the FWHM for the direct peak is equal to 670eV (0.79%) determined by Gaussian fit to the measured intensities.

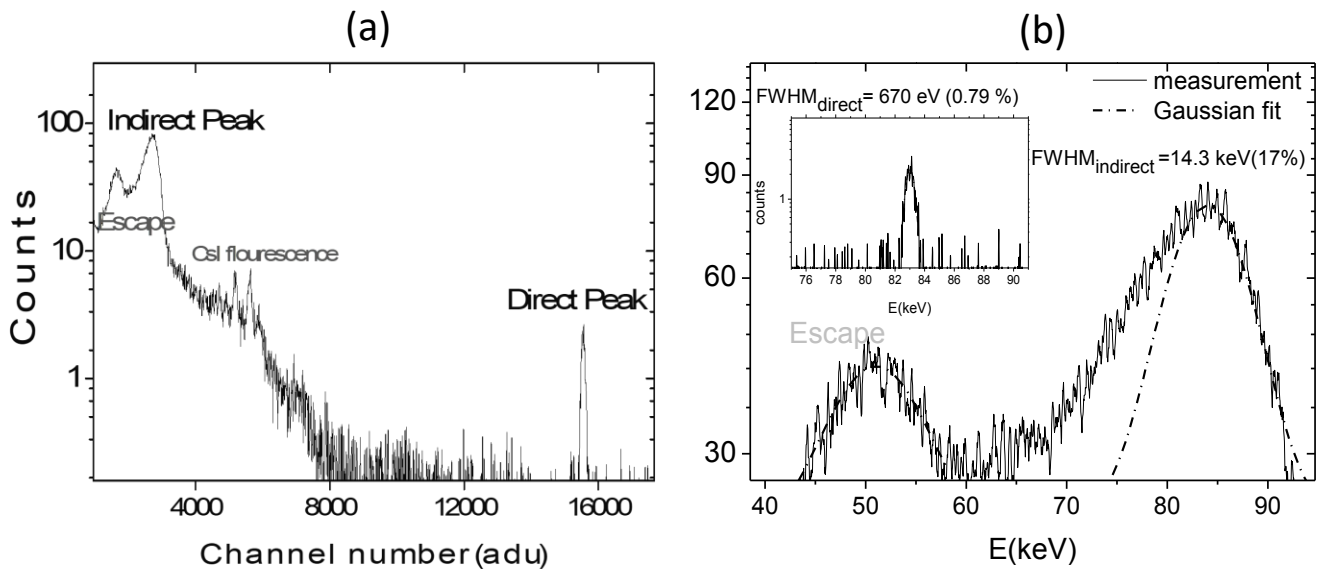


Figure 5.6: (a) Non-calibrated spectrum of a Bragg peak containing direct and indirect peaks in ADU unit (b): calibrated indirect spectrum with the photo peak at 83 keV of the spot with a FWHM of 15.3keV and a noise threshold of 4σ with $\sigma=5.5 e^-$. The FWHM of the direct peak for the same spot is 670 eV.

Several spots with energies between 57 and 90 keV were selected and their FWHM of respective direct and indirect peaks have been determined and shown in figure 5.7. The experimental values (red and blue dots) are compared to values calculated by eqs. 3 and 4 (black dots).

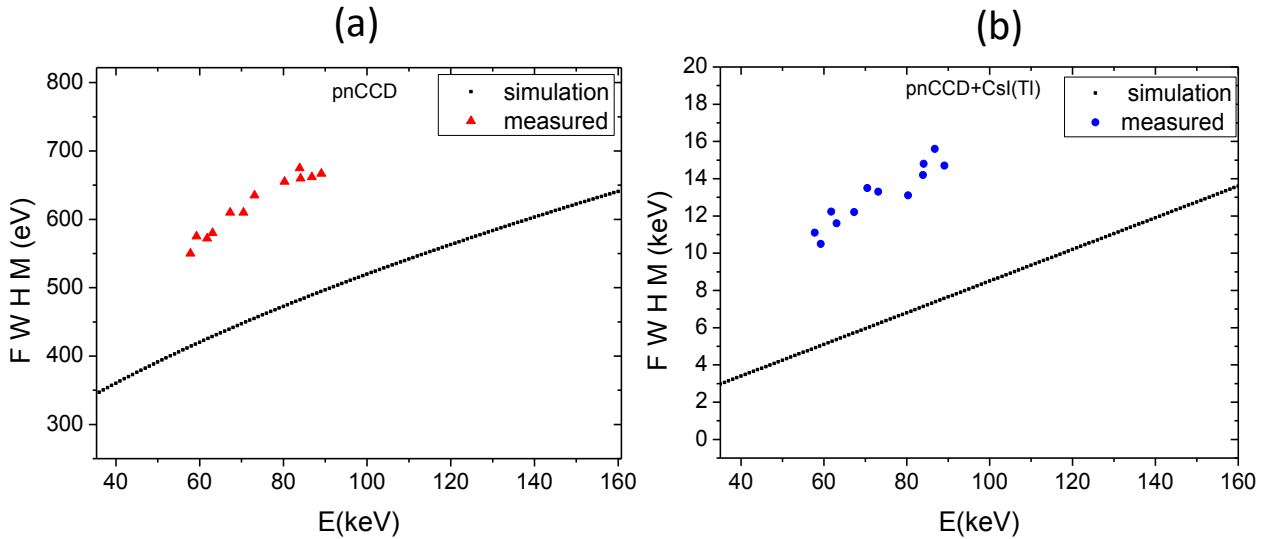


Figure 5.7: Measured FWHM and calculated physical limit of the energy resolution from equations 3.8 and 5.3 for directly (a) and indirectly (b) detected X-rays, respectively.

Figure 5.7 shows the measured FWHM in the energy range between 57 and 90 keV. The energy resolution of directly detected events is between 550 eV (0.9%) and 675 eV (0.7%). For indirect events, the FWHM is between 10.5 keV (18.5%) and 14.8 keV (16.5%). The signal threshold of 4 ENC was used for the data analysis where ENC is $\sigma=5.5 e^-$ (r.m.s). For directly detected X-rays, the difference between the measured FWHMs to the calculated values (determined by equation 3.8) in figure 5.7 (a) originates mainly from an imprecise gain correction. The gain and cte (charge transfer efficiency) values have been determined in a previous measurement with a radioactive source with known X-ray energies. In case of indirectly detected X-rays, there is an additional intrinsic contribution of the CsI(Tl) columns to the energy resolution (compared to the calculated values using equation 5.3 in figure 5.7 (b) for a bulk CsI(Tl) scintillator), due to an increase of surface effects at the CsI columns, such as a decrease of light yield close to the boundaries, because of a larger surface to volume ratio compared to bulk CsI(Tl).

5.6 Potential of pnCCD + CsI(Tl) for hard X-ray structure analysis

The use of hard X-rays for energy-dispersive Laue diffraction offers several advantages for structure analysis. The Ewald sphere is essentially flat over the solid angle covered by the detector allowing for access to a larger reciprocal space volume [90]. Therefore, comparing with experiments in 10 keV range the density of Laue spots significantly enhanced within a relatively small detector area. Moreover, owing to the increased attenuation length, samples of millimeters thickness can be probed, which increases the scattering volume, facilitates sample preparation and provides true bulk sensitivity. In order to demonstrate the potential of our approach for structure analysis using hard X-rays, we performed a transmission Laue diffraction experiment under the same experimental conditions as shown in section 5.3 and calculated the structure factor F_{hkl} which is an essential quantity for structure determination and refinement.

Here we used a single GaAs [111] sample instead of multiple wafers used before. 40 Laue spots have been recorded by taking detector frames at several positions around the incident beam center in order to virtually simulate a larger detector window. All recorded spots are shown in figure 5.8.

As a first step of data analysis for this experiment, the theoretical values of the structure factors moduli, $|F_{hkl}^{theo}|$, will be calculated for some Bragg reflections. Later on, the experimental values of these structure factors moduli, $|F_{hkl}^{exp}|$, will be determined from the measured intensities, once from the direct detection and another from the indirect detection of these spots. Finally, the experimental and theoretical values have to be compared in order to determine the achieved accuracy in structure factor determination using the new approach.

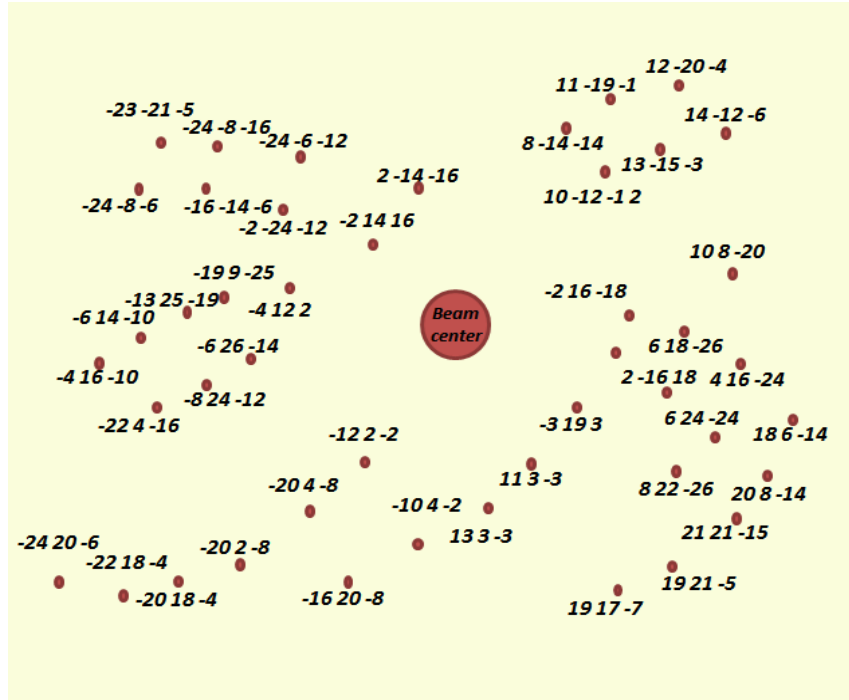


Figure 5.8: Laue pattern of a GaAs single crystal with their corresponding Miller indices. The Laue spot energies were detected between 42keV and 95keV.

Since the Miller indices of the Bragg peaks can be determined from measured Bragg angles and Bragg peak energies the structure factor can be determined from Bragg peak intensities. In order to index a certain spot, an energy spectrum of the Laue spot within an area of 10 x 10 pixels is extracted and the Bragg angle is determined based on scattering geometry. The interplanar distance d can be calculated using Bragg law (equation (4.1)) as the Bragg angle θ and diffraction energy E_{hkl} are known. At the same time, it is a function of the Miller indices hkl and the lattice parameter a , and so from equation (4.2) the value of $h^2 + k^2 + l^2$ can be calculated as well. In order to determine the correct signs of Miller indices of any Bragg reflection hkl in relation to all other reflections, we measured the angular relations between neighbored reflections. On the other hand, in a cubic system the angle between every two Miller planes $h_i k_i l_i$ and $h_j k_j l_j$ is determined by equation (4.3). Using this equation, the correct signs of all measured hkl are obtained by comparing all inter-planar angles of the measured reflections determined geometrically from experiment. The obtained indices of all measured Bragg reflections are shown in figure 5.8.

For zinc-blende structure, F_{hkl}^{theo} is given by:

$$F_{hkl}^{theo} = 4[f_{Ga}T_{Ga} + f_{As}T_{As}e^{i(\pi/2)(h+k+l)}] \quad (5.4)$$

where f_{Ga} and f_{As} denote the atomic form factors of a stationary Ga and As atom which can be found in the international Tables for Crystallography (2004, Vol. C) [91]. T_{Ga} and T_{As} are the temperature-dependent Debye-Waller factors of Ga and As , respectively. For a given atom, j , the Debye-Waller factor T_j is given by:

$$T_j = e^{-B_j \sin^2 \theta / \lambda^2}, \quad (5.5)$$

with λ being the wavelength of the diffracted spot, θ is the Bragg angle and B_j is the so-called temperature factor. Assuming that B_j is the same for all atoms in the crystal, $B_j \approx B$, B is usually determined from the plot of $\ln(\bar{I}_{hkl} / \overline{\sum_j f_j^2})$ against $\sin^2 \theta / \lambda^2$ commonly called the Wilson plot [92-94] with \bar{I}_{hkl} denoting the mean intensity of the of all measured reflections in the shell with the midpoint $\sin^2 \theta / \lambda^2$ and $\overline{\sum_j f_j^2}$ has to be understood as the respective average values evaluated at the mean of the upper and lower limits of the considered resolution shell.

Therefore, reflections appear if h, k and l are all even or odd. Considering the summation of h, k and l , one finds three different sets of structure factors, $|F_{hkl}^{theo}|$

$$|F_{hkl}^{theo}|^2 = \left\{ \begin{array}{l} 16(f_{Ga}T_{Ga} + f_{As}T_{As})^2 \text{ for } h + k + l = 4n \\ 16(f_{Ga}T_{Ga} - f_{As}T_{As})^2 \text{ for } h + k + l = 4n + 2 \\ 16(f_{Ga}^2T_{Ga} + f_{As}^2T_{As}) \text{ for } h + k + l = 4n + 1 \text{ or } 4n + 3 \end{array} \right\} \quad (5.6)$$

where n is an integer. It can be seen from equations (5.6) that planes with $h + k + l = 4n$ have stronger reflections over those with summation of $4n + 1$, $4n + 3$ or $4n + 2$.

Experimentally, the structure factor depends on the intensity of the Bragg peak and other factors as shown in the equation below:

$$|F_{hkl}^{exp}|^2 = \frac{I_{hkl}}{CI_0LPA} \quad (5.7)$$

where C denotes a scale factor, I_0 the intensity of the incident white X-ray beam at the diffraction wavelength, $I_{hkl} = I/\varepsilon$ the intensity of the Bragg peak with I being the measured integrated intensity of this reflection and ε the energy- and angular-dependent quantum efficiency of the interacting medium. L is the Lorentz factor takes into account that in real X-ray diffraction experiments, the Bragg condition cannot only be fulfilled by one specific wavelength λ and one single incident angle θ , but within narrow wavelength and angular bands enclosing these values. In our case of a spatially fixed crystal exposed to white X-rays is defined as [95],

$$L = \left(\frac{\lambda}{\sin\theta} \right)^2. \quad (5.8)$$

P is the polarization factor arises from the polarization effect associated with the nature of the incident beam that can be written as [57]:

$$P = \frac{1}{2}(1 + \cos^2 2\theta) - \frac{1}{2}\tau \cos 2\rho \sin^2 2\theta. \quad (5.9)$$

While the first term of equation (5.9) denotes the contribution of an unpolarized X-ray beam, the second term describes the attenuation of the scattered intensity due to the polarization of the synchrotron radiation. τ is the degree of polarization given by the ratio of the difference between the parallel and perpendicular components of polarization direction (relative to the plane of the electron orbit in storage ring) to their summation:

$$\tau = \frac{I_{par} - I_{per}}{I_{par} + I_{per}}. \quad (5.10)$$

However, the perpendicular component I_{per} is almost vanished for bending magnet radiation and hence $\tau \approx 1$. The angle ρ denotes the position of the Laue spot on the detector plane such that:

$$\rho = \arctan \frac{z}{x}. \quad (5.11)$$

In our detection range the applied polarization factors have values between 0.9 and 1. The last term in (5.9) A takes into account the absorption effect along the path of the diffracted beam inside the crystal.

In order to normalize the experimental values to the respective $|F_{hkl}^{theo}|$ the incident beam profile was considered for the calculation of I_0 and the scale factor C was defined by means of a least-squares method taking into account only strong reflections. The diffraction intensity I_{hkl} integrated either from the direct peak of the spots or from the indirect peak is corrected by $I_{hkl} = I/QE_{ph}$, where I is the measured intensity of the spot, and QE_{ph} is the photoelectric contribution of the quantum efficiency of Si and CsI(Tl) for the direct and indirect detection, respectively. The integration of each Bragg spot has been performed within a detector area of 10x10 pixels including the intensities of pile-ups and the escape peaks, while the Compton and the background events

were excluded. However, this calculation contains systematical and statistical errors, σ_{sys} and σ_{stat} respectively such that:

$$\sigma_{sys} = \frac{I}{QE_{ph}^2} \times \sigma_{QE_{ph}} \text{ and } \sigma_{stat} = \frac{\sqrt{I}}{QE_{ph}} \quad (5.12)$$

where $\sigma_{QE_{ph}}$ is the error in QE_{ph} which is calculated from the respective attenuation coefficients of Si and CsI(Tl).

Since the quantum efficiency of Si in hard X-ray range is very low compared to photons from CsI(Tl) registered in low energy range, both systematical and statistical errors of the direct peak intensities are much larger compared to the errors determined for the indirect peaks. As shown in figure 5.9, the total error in the direct peak intensities is between 19% for 42keV spot and 40% for 95keV whereas the intensities calculated from the indirect Bragg peak are in the range between 1% and 2.2% in the same energy range

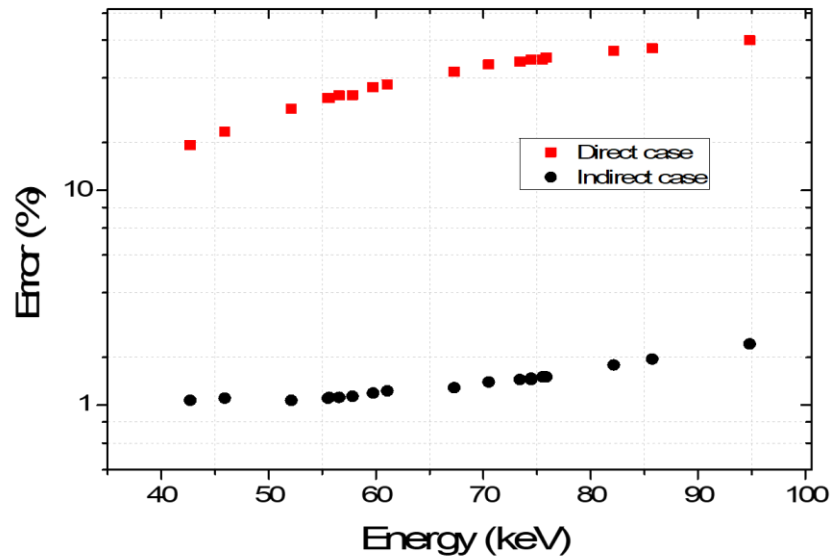


Figure 5.9: Total error propagation for primary intensity of Laue spots calculated from direct peak (black squares) and from indirect peaks (red dots). For the direct detection case, the error reaches a value of 40% at 95 keV, while for the indirect case it doesn't exceed 2.2% at the energy.

The comparison between all 19 evaluated experimental and theoretical structure factor magnitudes is visualized in Figure 4.10. It can be seen that the agreement depends on the type of the considered Bragg peak: structure factor moduli. For strong reflections fulfilling $h + k + l = 4n$, $4n + 1$ or $4n + 3$ the agreement between both is approximately 18% using the direct peak intensities and around 3% using the indirect intensities.

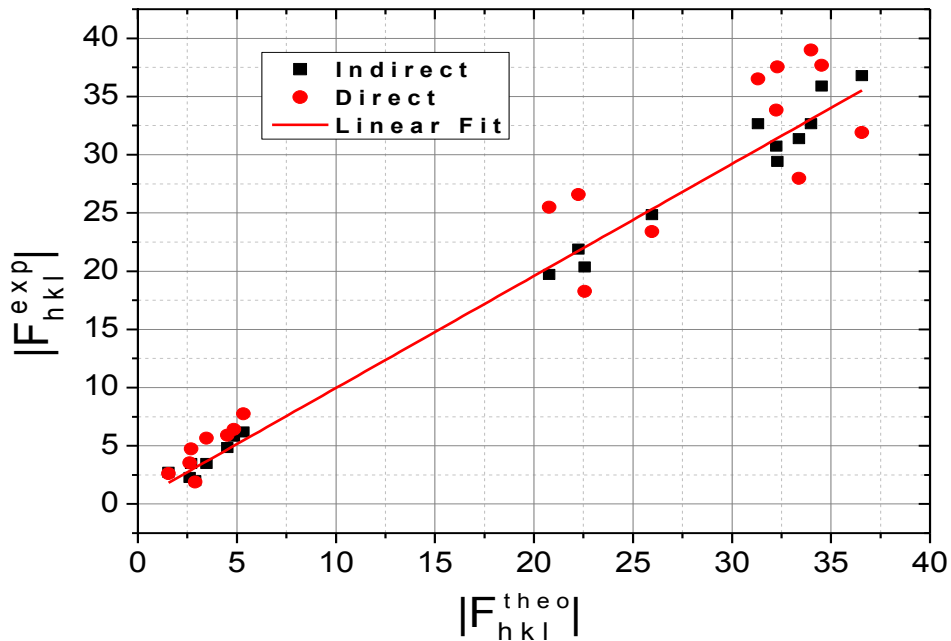


Figure 10: Experimental structure factor calculated from the intensity of the direct peaks (black dots) and from indirect peaks (red dots) V.s. theoretical values extracted from hkl values of the spots.

For the weak reflections with $h + k + l = 4n + 2$, the deviation for the direct case is in the order of 35% using the direct energies and 15% for the indirect case. This improvement in accuracy of structure factor determination is mainly caused by the much higher quantum efficiency of silicon in the energy range of indirect counting. Therefore, using the pnCCD with CsI(Tl) the accuracy of structure factor determination in hard X-ray range can be as good as in low energy range close to 15 keV

6 Structure analysis of SrLaAlO₄ by means of EDLD using ultra high x-ray radiation

In the previous chapter it has been shown that the energy resolution of the directly detected Laue peaks with energies ranging between 40 and 90 keV is in the order of 0.7% and 0.9% while the energy resolution of the indirect detection of these peaks is between of 16.5% and 18.5%. Furthermore, the scattering intensities of these peaks were determined from their indirect detection with an error of less than 1.5%. This achievement makes the combined system favorable for structure analysis in hard X-ray range.

Using energy-insensitive area detectors and pink X-ray beams, the structure analysis in macromolecular crystallography [96, 97] and Laue micro-diffraction of inorganic samples [98, 99] is possible only with considering prior knowledge of the material. On the other hand, energy-dispersive point detectors (EDDs) enable measurement of a complete energy spectra but detection of different Laue spot positions requires detector movement along the plane of detection in order to detect the spots sequentially. This strategy is generally time consuming. Other detectors like the PILATUS or XPAD detector do not perform a precise measurement of the X-ray signal amplitude, but they count the number of measured signal amplitudes above a given discriminator threshold [100, 101]. In a white X-ray spectrum or in a spectrum with several X-ray lines they cannot be used as a reliable, simultaneous energy dependent X-ray counter. Simultaneous indexation of several Laue reflections is impossible. In contrast, pnCCDs allow for an efficient combination of two-dimensional position and energy resolution of incident X-rays. So far, the pnCCD has been used for crystal structure analysis in the energy range between 5-35 keV except in [67] where the structure of GaAs has been determined using pnCCD without scintillator in hard X-ray energy up to 130 keV. In addition to well-detected low energetic spots the high energy Laue spots could be detected with a very low counting statistic. At the end the structure factors of the high energetic reflections were calculated with an average deviation more than 11% compared to the theoretical values. However, it has been shown in [13] that this accuracy can be improved to less than 1.5% when the structure factor determination is mainly based on the indirect detection of the peaks when the pnCCD is coupled to CsI(Tl) scintillator. The use of hard X-rays for Laue diffraction

experiments profits from the fact that the part of the Ewald sphere that is cut by the detection plane is rather flat, accessing a large reciprocal-space volume simultaneously [2, 102]. In this way, the density of Laue spots to be collected by the relatively small pnCCD detector area is significantly enhanced compared to previous experiments. Furthermore, the lower photoelectric interaction at the hard X-ray leads to less radiation damage in crystalline materials [103].

The solid state physics group of University of Siegen is equipped with a frame store module pnCCD combined with a CsI(Tl) scintillator with the specifications shown in chapter 5 and the camera is used for hard X-ray applications such as crystal structure determination, single grain analysis of polycrystalline samples and texture analysis. In this chapter we show the determination of unit cell parameters and orientation of tetragonal SrLaAlO₄ crystal without any prior information by means of energy dispersive Laue diffraction experiment using the pnCCD + CsI(Tl) detector system and white X-ray energy ranging between 40 and 130 keV. It will be demonstrated that the spatial resolution and spectroscopic performance of the indirect detection of this hybrid detector in this energy range is sufficient for precise determination of unit cell parameters and lattice vectors orientation. For fast data analysis, a GPU-based algorithm was applied which executes all recorded reflections in parallel and in real time [104].

6.1 Experiment setup and data collection

The investigated crystal with orientation [001] was fixed in front of the detector and illuminated by a 100x100 μm^2 wide beam provided by EDDI beamline (see section 5.3) such that the experiment has been performed in a transmission geometry. In this setup, the direction of the beam toward the sample is considered as the ($-y$) direction, whereas the plane containing the detector is taken as the x, z plane. In order to avoid radiation damage, the detector was operated in the single photon counting mode. The primary white X-ray beam with energy range [1-130 keV] was attenuated by means of 1 cm thick of aluminum plate. The presence of the Al absorber in front of the sample cuts off the photons with energy below 40 keV. In order to simulate a larger detector window virtually, an area of 5 x 3 cm^2 of the x - z plane at a distance $L=6$ cm in front of the sample has been scanned by the detector. The average count rate was about 33000 events/s within the entire sensitive area such that the detector was operated at a frame rate of 400 Hz. The event

detection threshold was set to 4σ where $\sigma = 5.5 e^-$ is the equivalent noise charge in the selected gain mode of the detector including thermal and electronic noise components.

A scheme of the collected Laue pattern is shown in figure 6.1 in which about 130 spots have been recorded. Generally, Laue spots with energies less than about 90 keV were detected directly by pnCCD. In contrast, spots with energies higher than 90 keV cannot be directly detected by the pnCCD due to the low quantum efficiency but they are detected indirectly after interaction with the scintillator. Once a photon interacts directly with pnCCD and converts to an electron cloud, it can be collected as single pixel event or distributed over neighbor pixels (double, triple or quadruple pixel event) depending on the cloud size (proportional to the photon energy) and conversion position (see section 3.3.1). However, when the photon is detected indirectly, the generated electron cloud is a result of the sum of many scintillation photons which typically spread over more than 10 pixels. The widespread and the high statistic of the indirect event gives rise to a well-defined peak center.

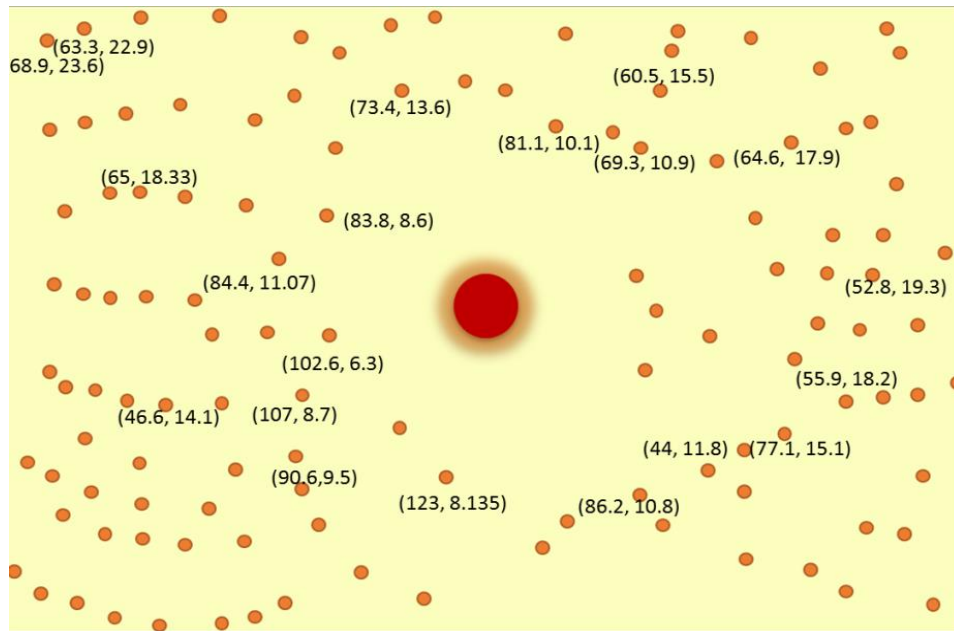


Figure 6.1: Laue pattern generated by SrLaAlO₄ crystal recorded by the pnCCD + CsI(Tl). Some of the Bragg reflections were detected directly and indirectly at the same time, while some others with higher energies were just detected indirectly. The Energy and Bragg angle ($E(\text{keV}), 2\theta$) are shown beside some spots.

6.2 Spectral analysis

The spectrum integrated over all events is shown in figure 6.2 in ADU units. It contains the direct detections of K- α and K- β emission lines of Sr and La (elements of the illuminated crystal) located at 1793, 2010, 4252, 4830 and 4950 ADU corresponding to 14.1, 15.8, 33.2, 37.8 and 38.7 keV, respectively. The spectrum includes also the K- α and K- β lines of I and Cs (elements of the scintillator) located at 3647, 4125, 3950 and 4472 ADU corresponding to 28.4, 30.7, 32.2 and 34.9 keV, respectively.

These direct peaks were resolved with an energy resolution between 0.75% and 0.9% at the selected gain of the detector and they have been served for the calibration of the channel numbers (from ADU to eV) while the peak between 250 and 750 ADU is the result of the convolution of their indirect peaks.

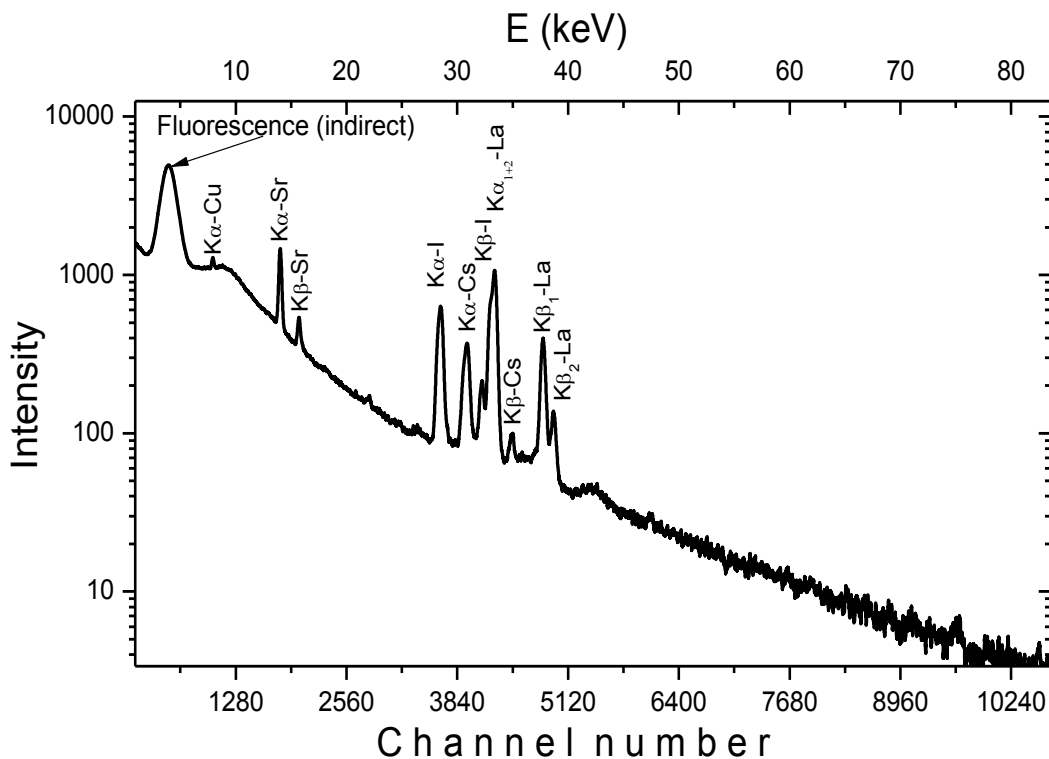


Figure 6.2: Spectrum of all direct and indirect events.

In order to identify the Bragg energies, the spectra of all detected spots were extracted from an area of 5x5 pixels around the center of each spot. In case the Laue spot is detected directly and indirectly at the same time, the respective spectrum will contain two Bragg peaks, one at the energy corresponds to the direct detection of the spot, and another peak at lower energy (typically between 1 and 35 keV) corresponding to the indirect detection. After calibration the peak positions can be converted to the corresponding incoming photon energy. Figure 6.3 shows two examples of the recorded spectra of two different types of spots, where (a) is the spectrum of a spot detected directly, and (b) for another spot detected indirectly. The events with size between 1x1 and 10x10 pixels (non-recombined events) measure the direct and the indirect events, respectively. The Bragg peak from the direct detection in (a) is located at energy 66.9 keV with a FWHM of 539 eV, while the peak referring to the indirect detection is located at 10.42 keV with a FWHM of 2.07 keV represented in the energy scale of the direct events.

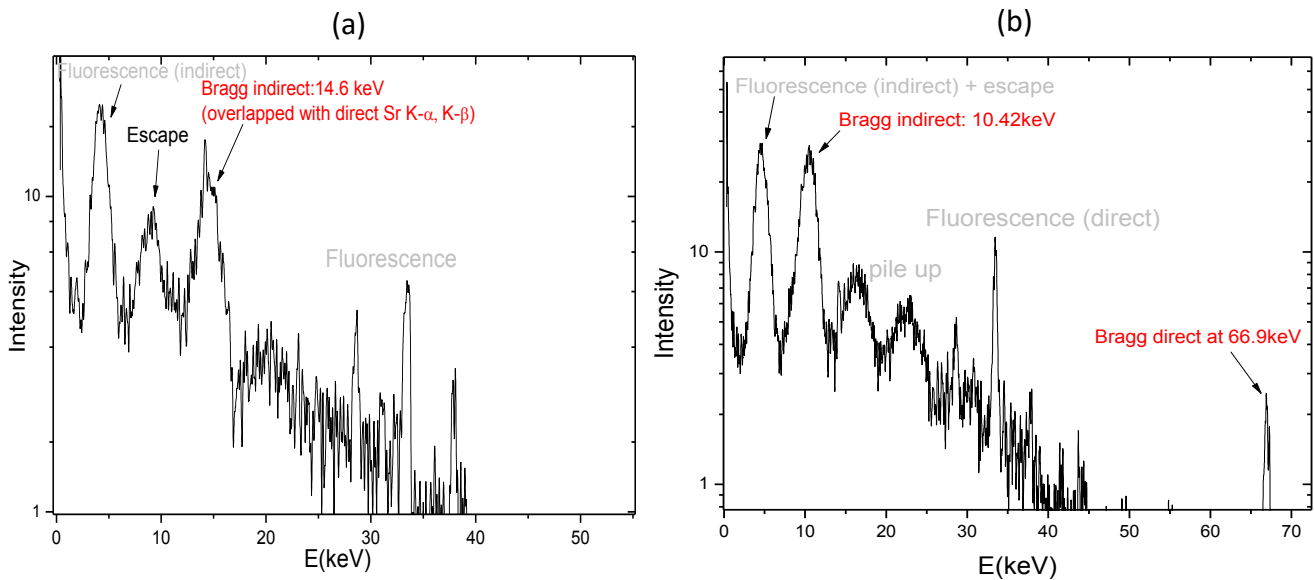


Figure 6.3: spectra of two Laue spots given by pnCCD, where (a) was detected directly and indirectly at the same time while (b) was just detected indirectly.

Figure 6.3 (b) is an exemplary spectrum of the indirectly-detected spots. This spectrum does not contain the direct peak due to its high energy while its indirect peak appears at energy of 14.6 keV. This peak is overlapping with K- α and K- β lines of Sr at 14.1 and 15.8 keV, respectively. The spectrum also contains the indirect fluorescence peak at 4.2 keV followed by escape peak from the

indirect Bragg peak at 8.99 keV. The direct peaks of the fluorescence lines between 27 and 37 keV are also visible in this spectrum. The energy of the indirect Bragg peak is proportional to the energy of the incident photon and hence one need to find the relation between the incident photon energy (direct energy) and the indirect energy which is usually depend on the selected gain of the detector. The energies of all spots that are detected directly and indirectly at the same time, like the case of (a), are used to find the functional relation. The direct energies of all indirectly-detected spots then can be identified and the intensities of these spots can be calculated from the indirect peaks taking into account the quantum efficiency of CsI(Tl) at the incident energy as well the escape and pile up peaks. As example, the direct photon energy of the spectrum shown in (b) was determined to be 92.5 keV. It is noteworthy that no Compton events are involved in the indirect spectra since Compton electrons can't spread over more than 1 pixel whereas only events with size larger than 10 pixels are included in these spectra.

6.3 Calculation of lattice parameters

As soon as the spots energies are identified, a scattering vector \vec{q} for each Bragg reflection can be assigned by the difference between the outgoing and incoming wave vectors:

$$\vec{q} = \vec{k}_f - \vec{k}_i \quad (6.1)$$

such that

$$|\vec{k}_f| = |\vec{k}_i| = 2\pi/\lambda = E/\hbar c \quad (6.2)$$

where λ is the wavelength of the spot, E its energy, \hbar is the Plank constant and c is the speed of light. Every Laue spot collected by the detector is characterized by the intensity, I, energy, E, and three dimensional coordinates, x, y and z

$$\hbar c \vec{q} = \hbar c \begin{pmatrix} q_x \\ q_y \\ q_z \end{pmatrix} = \frac{E}{s} \begin{pmatrix} x \\ y - s \\ z \end{pmatrix}, \quad (6.3)$$

with s being the distance between the sample and the Laue spot at the detector plane:

$$s = \sqrt{x^2 + y^2 + z^2}. \quad (6.4)$$

In our experiment the measured part of the reciprocal lattice of the crystal is confined in a cuboid with ranges $-13 \leq q_x \leq 13 \text{ \AA}^{-1}$, $-4 \leq q_y \leq 0 \text{ \AA}^{-1}$ and $-8 \leq q_z \leq 8 \text{ \AA}^{-1}$. The error $\delta \vec{q}$ depends on the precision of position and energy of the spot such that:

$$\delta q_x = \frac{|x| \delta E}{s \hbar c} + \frac{E}{s^3 \hbar c} [(y^2 + z^2) \delta x + |xy| \delta y + |xz| \delta z], \quad (6.5)$$

$$\delta q_y = \frac{(s - y) \delta E}{s \hbar c} + \frac{E}{s^3 \hbar c} [(x^2 + z^2) \delta y + |yx| \delta x + |yz| \delta z], \quad (6.6)$$

$$\delta q_z = \frac{|z| \delta E}{s \hbar c} + \frac{E}{s^3 \hbar c} [(x^2 + y^2) \delta z + |zx| \delta x + |zy| \delta y], \quad (6.7)$$

The energy of the reflections has been resolved with a standard deviation ranging between 0.6 and 0.8% considering the Gaussian fit to the measured Bragg peak energy. The high intensities of the reflections due to the indirect detection improve the spatial uncertainty to less than one pixel size. Consequently, using equations (6.5), (6.6) and (6.7), the components of the scattering vector \vec{q} associated with the reflections could be resolved with absolute accuracies of $\delta q_x < 0.15 \text{ \AA}^{-1}$, $\delta q_y < 0.08 \text{ \AA}^{-1}$ and $\delta q_z < 0.15 \text{ \AA}^{-1}$. The scattering vector corresponding to the evaluated peak centers in terms of position and energy is equal to a reciprocal lattice vector of the sample as shown in equation (4.4).

In order to find the lattice constants of SrLaAlO₄, we applied the method used in [105] in which the Minkowski-reduced basis [106] of the measured reciprocal lattice has been computed by crystallographic reduction [107, 108] and least-square refinement of sets of three non-collinear scattering vectors $\{\vec{q}_1, \vec{q}_2, \vec{q}_3\}$ providing a complete indexation of all recorded reflections. Because of the large number of events included in each reflection which requires a relatively long execution time, a new GPU-based algorithm has been developed and used for the computing of this method [109]. Depending on the parallel computation technique, a speed-up factor up to 4 comparing with the serial algorithm. This algorithm has the Single Instruction Multiple Threads (SIMT) style [110] and consists of two stages: (1) Parameters calculations: in which the essential parameters (e.g. energy, diffraction angle, d-spacing, possible Miller indices list etc.) for each localized reflection are calculated. Each thread processes a single reflection saving the final output in a data container for further calculations. (2) The main core: in which the main method is applied. The localized reflections are divided into threefold subsets covering all possible mutations. Using the output generated by the previous stage, each subset is processed by a single thread. The reciprocal basis vectors are then obtained:

$$\vec{b}_1 = \begin{pmatrix} 1.51 \\ 0.16 \\ -0.73 \end{pmatrix} \text{Å}, \quad \vec{b}_2 = \begin{pmatrix} 0.34 \\ 1.29 \\ 1.01 \end{pmatrix} \text{Å}, \quad \vec{b}_3 = \begin{pmatrix} 0.19 \\ -0.31 \\ 0.33 \end{pmatrix} \text{Å}$$

and hence the basis vectors in the real crystallographic axes can be calculated:

$$\vec{a}_1, \vec{a}_2, \vec{a}_3 = \begin{pmatrix} 3.34 & 0.78 & 4.98 \\ 0.38 & 2.91 & -7.93 \\ -1.61 & 2.25 & 8.45 \end{pmatrix}$$

Subsequently, the lattice constants and the enclosed angles of the crystal are defined:

$$|\vec{a}_1| = 3.73 \text{ \AA} \quad \alpha_1 = 89.64^\circ$$

$$|\vec{a}_2| = 3.76 \text{ \AA} \quad \alpha_2 = 90.21^\circ$$

$$|\vec{a}_3| = 12.61 \text{ \AA} \quad \alpha_3 = 89.98^\circ$$

The evaluated data are in good agreement with the literature values of the tetragonal structure of SrLaAlO₄ with a standard deviation of 0.1, 0.2 and 0.7% for the lattice constants and of 0.02, 0.23 and 0.4% for the enclosed angles, respectively. This accuracy is better than that obtained previously in [105] where white synchrotron radiation with energy less than 35 keV was used. This improvement can be correlated to the higher number of Laue spots detected within a wide range of energy and the improved count rate of these spots due to the improvement of the detector quantum efficiency. Once the lattice parameters have been determined, the Laue pattern can be indexed entirely by projecting the measured \vec{q}_i vector of each reflection onto the basis vectors \vec{a} using Laue equations:

$$h_i = \frac{\vec{q}_i \cdot \vec{a}_1}{2\pi}, \quad k_i = \frac{\vec{q}_i \cdot \vec{a}_2}{2\pi}, \quad l_i = \frac{\vec{q}_i \cdot \vec{a}_3}{2\pi} \quad (6.8)$$

The obtained Miller indices of some selected spots are shown later in table 6.1. Some spots spectra contain two peaks at energies E and 2E corresponding to the first and second orders reflections. In this case only the first order reflection has been taken into account and the Miller indices are calculated based on this energy. However, in case E is less than 40 keV (the lower limit of the incident energy), only the second order reflections (2E) can be scattered from the crystal as E has been absorbed by Al absorber. This leads to a second order Miller indices. For example, spot (-6 4 -6) has an energy of 63.3 keV appeared at angle 22.9° instead of (-3 2 -3) reflection at the same angle with an energy 31.65 keV as this energy is not included in the used energy range.

6.4 Structure factor

As discussed previously, the magnitude of the structure factors F_{hkl} can be calculated experimentally with a relatively high accuracy when the intensities of the reflections are extracted from the indirect peaks rather than the direct peaks. It's challenging to calculate the structure factors experimentally with an error as low as possible. It can be seen from equation (5.7) that the error in the structure factor calculation of a given hkl reflection is strongly depending on the error propagation from the intensity calculation. This includes the systematical and statistical errors in equation (5.12). The relative error to the calculated diffracted intensity I_{hkl} can be written as:

$$\frac{\sigma_{I_{hkl}}}{I_{hkl}} = \frac{\frac{I_{hkl} \cdot E}{E^2} \times \sigma_E + \frac{\sqrt{I_{hkl} \cdot E}}{E}}{I_{hkl}} = \frac{\sigma_E}{E} + \frac{1}{\sqrt{I_{hkl} E}} \quad (6.9)$$

Which makes the quantum efficiency is the main factor affects the precision of I_{hkl} calculation and subsequently the accuracy of structure factor determination.

Table 6.1 shows a list of the recorded reflections with their Miller indices, Bragg angles, Bragg peak energies, interplanar distances and the experimental structure factors with their standard deviations. As discussed before, the standard deviation, σ_F depends on the deviation in the intensity calculation which itself strongly depends on the quantum efficiency of the detection material as well on the intensity of the spot (equation 6.9) such that the higher efficiency and higher intensity leads to higher precision. For the aim of having the best possible accuracy in the calculation of the structure factors, the diffracted intensities I_{hkl} have been extracted from the indirect peaks where the detected intensities, I , are much higher than those found in the direct peaks. The results show that σ_F (%) doesn't exceed a value of 2,5%. The precision of F_{hkl} increases as the Bragg peak energy get higher reaching a value of 0,9% for the reflection -3 1 -4 at $E= 41,7$ keV but 2,5% for reflection -1 -5 0 at $E= 129,1$ keV. The obtained accuracy is much better than those obtained by similar experiments using bare pnCCD [67, 68, 105] and is in good agreement

with the results obtained in [13] where pnCCD + CsI(Tl) detector system has been used for the structure analysis of GaAs.

h k l	$2\theta^\circ$	E(keV)	d(Å)	F_{hkl}	$\sigma_F(\%)$
-6 4 -6	22,9	63,3	0,49	22,1	1,4
-7 4 -7	23,6	68,9	0,44	1,9	1,5
-5 3 -6	18,3	65	0,60	14,5	1,2
-4 2 -6	11,07	84,4	0,76	31,2	2,0
-3 -1 -4	14,1	46,6	1,08	27,9	1,1
-1 5 0	13,6	73,4	0,71	24,6	1,6
-2 3 -3	8,6	83,8	0,98	24,1	1,8
-3 0 -5	6,3	102,6	1,10	22,9	2,1
-4 -2 -6	8,7	107	0,76	31,6	2,0
-3 -3 -4	9,5	90,6	0,82	21,8	1,7
-1 -5 0	8,13	122,9	0,71	25,7	2,4
2 -3 5	6,6	113,8	0,94	19,7	2,3
2 -4 6	10,8	86,2	0,76	32,4	1,6
-3 1 -4	15,7	41,7	1,08	28,2	0,9
2 -1 5	11,8	43,9	1,37	27,5	1,1
3 -2 7	7,6	106,8	0,88	7,25	2,2
5 -1 12	11,1	108,7	0,59	1,1	2,1
5 3 12	11,7	112,7	0,53	0,9	2,2
4 4 10	12,5	99,2	0,57	3,8	1,9
4 3 9	8,5	129,1	0,64	2,6	2,5
4 3 11	17,8	64,6	0,62	21,6	1,3
4 -1 11	18,2	55,9	0,68	25,9	1,2
4 -3 11	15,1	77,1	0,60	21,7	1,6
4 1 11	19,3	52,7	0,70	25,1	1,2
6 -5 17	16,1	112,7	0,39	10,3	2,3
6 5 17	19,0	95,4	0,4	11,1	2,0
-6 -4 -6	19,8	73,1	0,48	21,5	1,5
-4 1 -5	18,2	47,1	0,84	17,9	1,1
4 5 11	14,7	89,9	0,51	15,9	1,9
-4 -1 -5	17,0	50,4	0,83	18,5	1,1
6 -1 15	13,5	108,7	0,48	8,4	2,2

Table 1: Miller Indices, Bragg angles, energies, interplanar distances and the experimental structure factors with their percent standard deviations of the detected reflections

7 Summary and Conclusion

In this thesis few applications of pnCCD using white hard X-ray synchrotron radiation have been demonstrated. The presented results are based on two major innovations:

- i. Considering the 4-dimensional data volume of the detector the characterization of several single grains in the polycrystal is possible at their same time and can be analyzed under external load. The deformation process of a polycrystalline nickel wire under an external tensile loading has been investigated by means of energy-dispersive Laue diffraction (EDLD) experiment using white hard X-ray synchrotron radiation and energy-dispersive pnCCD detector.
- ii. Coupling of a columnar CsI(Tl) scintillator with pnCCD silicon detector extends the detectable energy range towards 100 keV which is very attractive for the analysis of metals and other technical materials. The performance of pnCCD coupled to columnar structured CsI(Tl) scintillator in the hard X-ray range was tested. The quantum efficiency and energy resolution of the combined system have been found showing an extreme improvement of the efficiency at the hard X-ray energy range comparable to the case of bare pnCCD. This enhancement was employed in structure analysis of single crystals in which the Lattice parameters, unit cell orientation and the structure factor moduli were determined with a high accuracy relative to the expected values.

Advances in 2DED X-ray detectors make it possible to exploit the complete polychromatic spectrum of high-brightness synchrotron sources in the development of energy dispersive and spatially resolved X-ray techniques. In chapter 4 we have described the applicability of EDLD in the characterization of polycrystalline materials. In a single shot experiment, Laue diffraction images are analyzed to obtain the crystal symmetry, lattice orientation and lattice strain distribution at the sub-grain level. The fact that, this technique does not require sample rotations in order to probe different lattice planes is a great advantage whenever high spatial resolution is required or the sample crystal structure is not known.

In situ tensile loading was applied to investigate the deformation behavior of a group of 9 grains. Spatial elongation, i.e. streaking of the Laue spots was observed and linked to gradual rotation of the lattice planes. The streaking magnitude differs between lattice planes depending on the orientation of the grain and hence the slip system. As an example, from grain 4, the planes that is close to being parallel to the slip system shows the largest streaking. While other 2 lattice planes from the same grain show confined spatial distribution. By analyzing the energy profile of the streak, we could determine the change in the lattice spacing d , and the distribution width of d . The results document that EDLD is a powerful technique to study heterogeneities in applied material systems.

The constraint of using silicon-based detectors for hard X-ray applications due to their low quantum efficiency for high energetic photons (above 10 keV) could be overcome by combining a pixelated silicon-based detector system with a columnar scintillator. In chapter 5 the characterization and performance of pnCCD coupled to columnar structured CsI(Tl) scintillator in the hard X-ray range have been investigated. The main advantage of this combination over the bare pnCCD is the improvement of the quantum efficiency for hard X-rays. It has been increased from 1% at 100 keV for the naked pnCCD to about 45% at the same energy using the new combined system. Performing a Laue type diffraction experiment, using multiple GaAs samples many Laue spots were generated. Following the Bragg equation these spots appear at different energies ranging between 55 and 120 keV. Spots with energy larger than 90 keV could be identified properly only from the indirect signal because of the high QE of CsI compared to Si. The energy resolution of the system for different peaks within this energy range was investigated. For the direct peaks the resolution was found in the order of 0.7% and 0.9%, while for their corresponding indirect peaks the resolution was found between 16.5% and 18.5%. The combined detector shows a high potential for hard X-ray structure analysis compared to the bare pnCCD. The errors in the intensities calculation from the direct peaks were between 19% and 40% in the energy range from 42 to 95 keV, whereas the error decreased to the order of 1.5% when the intensities were calculated from the indirect peaks in the same energy range. The structure factors of several high energetic reflections from a single GaAs wafer were determined using both direct and indirect signals from the respective Bragg peaks. In the indirect case, the deviation of experimental structure factors from theoretical ones was in the order of 3% for the strong

reflections and 15% for the weak reflections in contrast to 18% and 35% in the case of direct detection.

In chapter 6 we demonstrated the structural analysis of SrLaAlO₄ using ultra high white X-ray energy ranging between 40 and 130 keV using pnCCD detector coupled to CsI(Tl) scintillator. The analysis was performed without any prior information. After a scan of an area of 5x3 cm² around the beam center, about 130 Laue spots have been detected. Reflections with energies higher than 90 keV were detected indirectly while those with lower energies could be detected directly and indirectly at the same time. Using the advantages of detecting spots at high energies with high intensity and with high position resolution the lattice parameters of the tetragonal unit cell could be determined with accuracy better than 0.7% for the basis vectors and less than 0.4% for the enclosed angles. Subsequently the Laue pattern could be indexed and the structure factors have been determined from the integrated intensities of the indirect peaks with a standard deviation between 0.9% and 2.5% for the spots in the energy range [40-130] keV. The achieved results of this work constitute a promising base for further crystallographic applications and structure analysis at ultra-high X-ray energies using the pnCCD coupled to columnar structure CsI(Tl) scintillator.

Bibliography

- [1] Klaus-Dieter Liss, Arno Bartels, Andreas Schreyer, and Helmut Clemens. High-energy x-rays: a tool for advanced bulk investigations in materials science and physics. *Textures and Microstructures*, 35(3-4):2192-52, 2003.
- [2] Y.-H. Wu, Y.-Y. Chang, Y.-W. Tsai, and S.-L. Chang. Theoretical considerations in the construction of hard x-ray resonators at inclined incidence with ultra-high efficiency and resolution. *Journal of Applied Crystallography*, 49(5):1653-1658, Oct 2016.
- [3] Jean Jakoncic, Marco Di Michiel, Zhong Zhong, Veijo Honkimaki, Yves Jouanneau, and Vivian Stojano_. Anomalous di_raction at ultra-high energy for protein crystallography. *Journal of Applied Crystallography*, 39(6):8318-41, Dec 2006.
- [4] Abboud A, Kirchlechner C, Keckes J, et al. Single-shot full strain tensor determination with microbeam X-ray Laue diffraction and a two-dimensional energy-dispersive detector. *J Appl Crystallography*, 50(Pt 3):901–908. 2017
- [5] Phillips M.A., Spolenak R., Tamura N., Brown W.L., MacDowell A.A., Celestre R.S., Padmore H.A., Patel J.R. X-ray microdiffraction: Local stress distributions in polycrystalline and epitaxial thin films *Microelectronic Engineering*, 75 (1) , pp. 117-126, 2004.
- [6] Choi, W.J., Lee, T.Y., Tu, K.N., Tamura, N., Celestre, R.S., MacDowell, A.A., Bong, Y.Y., & Nguyen, Luu. Tin whiskers studied by synchrotron radiation scanning X-ray micro-diffraction. *Acta Materialia*, 51(20), 6253-6261, 2003.
- [7] R. I. Barabash, G. E Ice, W. Liu and O. M Barabash. Polychromatic microdiffraction characterization of defect gradients in severely deformed materials. *Micron*, 40(1), pp. 28-36, 2008.
- [8] G.E Ice and R.I. Barabash. White Beam Microdiffraction and Dislocations Gradients. Nabarro, F.R.N. and Hirth, J.P. (eds). *Dislocations in Solids Elsevier, Vol. 13, Chapter 79*, pp. 500–601, 2007.
- [9] J. D. Budai, W. Liu, J.Z. Tischler, Z.W. Pan, D.P. Norton, B.C. Larson, W. yang and G.E. Ice. Polychromatic X-ray micro- and Nano diffraction for spatially-resolved structural studies. *Thin Solid Films*, 516(22), pp. 8013-8021, 2008.

- [10] D.M. Schlosser, R. Huth, M. and Hartmann, A. Abboud, T. Send, S. and Conka-Nurdan, M. Shokr, U. Pietsch, and L. Strder. Direct and indirect signal detection of 122 keV photons with a novel detector combining a pncd and a csi(tl) scintillator. *Nuclear Instruments and Methods in Physics Research Section A: Accelerators, Spectrometers, Detectors and Associated Equipment*, 805:55-62, Jan 2016.
- [11] James K. Walker Won Y. Choi Zhenxue Jing, Walter Huda. Detective quantum efficiency of a csi:tl scintillator-based scanning slot x-ray detector for digital mammography, *Proc. SPIE 3336, Medical Imaging 1998: Physics of Medical Imaging*, July 1998.
- [12] V. V. Nagarkar, T. K. Gupta, S. R. Miller, Y. Klugerman, M. R. Squillante, and G. Entine. Structured csi(tl) scintillators for x-ray imaging applications. *IEEE Transactions on Nuclear Science*, 45(3):492-496, June 1998.
- [13] M. Shokr, D. Schlosser, A. Abboud, A. Algashi, A. Tosson, T. Conka, R. Hartmann, M. Klaus, C. Genzel, L. Strder, and U. Pietsch. Applications of a pncd detector coupled to columnar structure csI(Tl) scintillator system in ultra high energy x-ray Laue diffraction. *Journal of Instrumentation*, 12(12):P12032, Dec 2017.
- [14] C. Kittel. Introduction to solid state physics. *Hoboken, NJ: Wiley*, 2005.
- [15] Claude Leroy and Pier-Giorgio Rancoita. Principles of Radiation Interaction in Matter and Detection. *Milan U. & INFN, Milan*, 2011.
- [16] A. M. Fox. Optical properties of solids, 2nd edition. *Contemporary Physics*, 52(6):612-613, 20011.
- [17] W. Heitler, The Quantum Theory of Radiation, 3rd edition. *Oxford University Press*, 1957.
- [18] W. Leo, Techniques for Nuclear and Particle Physics Experiments, 2nd Edition, *Springer-Verlag, New York, Berlin, Heidelberg*, 1994.
- [19] J.H. Hubbell. Photon Cross Sections, Attenuation Coefficients and Energy Absorption Coefficients from 10 keV to 100 GeV. *NSRDS-NBS 29, U.S. Department of Commerce, National Bureau of Standards*, 1969.
- [20] K. Kleinknecht, Detectors for Particle Radiation, 2nd edition. *Cambridge University Press, Cambridge*, 0521640326, 1998.

- [21] K. Debertin and R. G. Helmer. Gamma- and X-Ray Spectrometry with Semiconductor Detectors, *North-Holland*, 1988.
- [22] Berger, M. J., & Hubbell, J. H. *XCOM*: Photon cross sections on a personal computer (No. NBSIR-87-3597). *National Bureau of Standards, Washington, DC (USA). Center for Radiation Research*. 1987.
- [23] A. Owens, M. Bazdaz, S. Kraft, A. Peacock, S. Nenonen, and H. Andersson. The hard X-ray response of epitaxial GaAs detectors. *Nuclear Instruments and Methods in Physics Research, A*, 442 , 360-363, 2000.
- [24] M. C. Veale, S. J. Bell, L. L. Jones, P. Seller, M. D. Wilson, R. C. Cernik, J. Kalliopuska, H. Pohjonen, H. Andersson, S. Nenonen, and V. Kachkanov, Characterization of Edgeless CdTe Detectors for use in Hard X-Ray Imaging Applications. *IEEE Transactions on Nuclear Science* 59, 1536-1543, 2012.
- [25] C. Grupen and B. Shwartz, Particle Detectors, 2nd edition, *Cambridge University Press, Cambridge, New York*, 0521187958, 2008.
- [26] K. P. O'Donnell and X. Chen, Temperature dependence of semiconductor band gaps. *Applied Physics Letters* 58, 2924-2926, 1991.
- [27] Kane, Evan O. "Electron scattering by pair production in silicon. *Physical Review* 159.3: 624, 1967.
- [28] D. A. Neamen. Semiconductor Physics and Devices - 3rd Edition, *Tata McGraw-Hill Science, New Delhi*, 2002.
- [29] G. Lutz. Semiconductor Radiation Detectors. *Springer-Verlag, Berlin, Heidelberg*, 3540648593, 1999.
- [30] P. Lautenschlager, M. Garriga, L. Vina, M. Cardona. Temperature dependence of the dielectric function and inter-band critical points in silicon, *Phys. Rev. B*, 36 4821, 1987.
- [31] M. N. Mazziotta, Electron-hole pair creation energy and Fano factor temperature dependence in silicon. *Nuclear Instruments and Methods in Physics Research A* 584, 436-439, 2008.
- [32] G.F. Knoll. Radiation Detection and Measurement - 3rd Edition, *John Wiley & Sons, New York*. 1999.

- [33] R. Leo, William. *Techniques for Nuclear and Particle Physics Experiments* (2nd ed.). Springer, 1994.
- [34] R. K. Swank. Characteristics of scintillators. *Annual review of nuclear science* 4.1- 111-140. 1954.
- [35] Pochodzalla, Josef, et al. "Two-particle correlations at small relative momenta for induced 40 reactions on Au 197 at E/A= 60 MeV." *Physical Review C* 35.5 (1987): 1695.
- [36] Viesti, G., Prete, G., Fabris, D., Hagel, K., Nebbia, G., & Menchaca-Rocha, A. The response of a CsI (Tl) scintillator with photodiode readout to light particles and heavy ions. *Nuclear Instruments and Methods in Physics Research Section A: Accelerators, Spectrometers, Detectors and Associated Equipment*, 252(1), 75-79. 1986.
- [37] Kreutz, P., Kühmichel, A., Pinkenburg, C., Pochodzalla, J., Guo, Z. Y., Lynen, U., ... & Trockel, R. (). Photodiode readout and pulse shape analysis of CsI (Tl) scintillator signals. *Nuclear Instruments and Methods in Physics Research Section A: Accelerators, Spectrometers, Detectors and Associated Equipment*, 260(1), 120-123. 1987.
- [38] Bird, A. J., Carter, T., He, Z., Dean, A. J., & Ramsden, D. Pulse shape analysis of signals from a CsI (Tl)/photodiode detector. *Nuclear Instruments and Methods in Physics Research Section A: Accelerators, Spectrometers, Detectors and Associated Equipment*, 353(1-3), 46-49, 1994.
- [39] Gong, W. G., Kim, Y. D., Poggi, G., Chen, Z., Gelbke, C. K., Lynch, W. G., ... & Kwiatkowski, K. Resolution tests of CsI (Tl) scintillators read out by pin diodes. *Nuclear Instruments and Methods in Physics Research Section A: Accelerators, Spectrometers, Detectors and Associated Equipment*, 268(1), 190-199. 190, 1988.
- [40] Blucher, E., Gittelmann, B., Heltsley, B. K., Kandaswamy, J., Kowalewski, R., Kubota, Y., ... & Bean, A. . Tests of cesium iodide crystals for an electromagnetic calorimeter. *Nuclear Instruments and Methods in Physics Research Section A: Accelerators, Spectrometers, Detectors and Associated Equipment*, 249(2-3), 201-227, 1986.
- [41] Leroy, C. and Rancoita, P.G. Physics of cascading shower generation and propagation in matter: principles of high-energy, ultrahigh-energy and compensating calorimetry, *Rep. Prog. in Phys.* 63, no. 4, Institute of Physics Publishing, 505-606, 2000.

- [42] E. V. D. van Loef, P. Dorenbos, C. W. E. van Eijk, K. W. Kramer, H. U. Gudel, Scintillation properties of $\text{LaBr}_3:\text{Ce}^{3+}$ crystals: fast, efficient, and high-energy resolution scintillators, *Trans. Nucl. Sci* 486 254–258, 2002.
- [43] P. Lecoq, Inorganic Scintillators for Detector Systems. *Springer-Verlag Berlin Heidelberg*, 2006.
- [44] J. G. Sole, L. E. Bausa, D. Jaque (Eds.), An Introduction to the Optical Spectroscopy of Inorganic Solids, *John Wiley & Sons*, 2005.
- [45] V. Nagirnyi, A. Stolovich, S. Zazubovich, V. Zepelin, E. Mihokova, E. Nikl, G. P. Pazzi, L. Salvini, Peculiarities of the triplet relaxed excited-state structure and luminescence of a CsI:Tl crystal, *J. Phys.: Condens. Matter* 7 (18) 3637–3653, 1995.
- [46] <https://www.crystals.saint-gobain.com>
- [47] M. Balkanski, R. F. Wallis, Semiconductor Physics and Applications, *Oxford University Press*, 2000.
- [48] M. A. Green and M. J. Keevers, Optical properties of intrinsic silicon at 300 K, *Prog. Photovolt.: Res. Appl.* 3 (3) 189–192, 1995.
- [49] M. Balkanski, A. Aziza, E. Amzallag, Infrared absorption in heavily doped n-type Si, *Phys. Stat. Sol.* 31 323–330, 1969.
- [50] D. Schlosser, Response of high resolution silicon photodetectors coupled to CsI(Tl) or $\text{LaBr}_3(\text{Ce})$. *PhD thesis*, 2014.
- [51] R. Hartmann, K.-H. Stephan, L. Strüder, The quantum efficiency of pndetectors from the near infrared to the soft X-ray region. *Nucl. Instr. and Meth. A* 439 216–220, 2000.
- [52] Sebastian Ihle, Robert Hartmann, Marc Downing, Lothar Strüder, Sebastian Deiries, Hubert Gorke, Sven Hermann, Gottfried Kanbach, Janis Papamastourakis, Heike Soltau, and Alexander Stefanescu. Optical test results of fast pnCCDs. *IEEE Nuclear Science Symposium Conference Record*, 3351 - 3356. 10.1109, 2008.
- [53] S. Send, A. Abboud, R. Hartmann, M. Huth, W. Leitenberger, N. Pashniak, J. Schmidt, L. Strüder, and U. Pietsch. Characterization of a pnCCD for applications with synchrotron radiation. *Nuclear Instruments and Methods in Physics Research A* 711 132-142, 2013.

- [54] A. Abboud, S. Send, N. Pashniak, W. Leitenberger, S. Ihle, M. Huth, R. Hartmann, L. Strüder, and U. Pietsch, Sub-pixel resolution of a pnCCD for X-ray white beam applications. *Journal of Instrumentation*, P05005, 2013.
- [55] E. Pinotti, H. Bräuninger, N. Findeis, H. Gorke, D. Hauff, P. Holl, J. Kemmer, P. Lechner, G. Lutz, W. Kink, N. Meidinger, G. Metzner, P. Predehl, C. Reppin, L. Strüder, J. Trümper, C. von Zanthier, E. Kendziorra, R. Staubert, V. Radeka, P. Rehak, G. Bertuccio, E. Gatti, A. Longoni, A. Pullia, and M. Sampietro, The pn-CCD on-chip electronics. *Nuclear Instruments and Methods in Physics Research A*, 326, 85-91, 1993.
- [56] N. Meidinger, S. Bonerz, H. W. Braeuninger, R. Eckhardt, J. Englhauser, R. Hartmann, G. Hasinger, P. Holl, N. Krause, G. Lutz, E. Pfeffermann, R. H. Richter, H. Soltau, L. Strüder, and J. E. Trümper, Frame store PN-CCD detector for the ROSITA mission, *Proceedings of SPIE* 4851, 1040-1047, 2002
- [57] S. Send. Utilization of a frame store pnCCD for energy-dispersive Laue diffraction with white synchrotron radiation, *PhD thesis*, 2013.
- [58] M. Porro, S. Herrmann, and N. Hörnel, Multi correlated double sampling with exponential reset. *IEEE Nuclear Science Symposium Conference Record*, 291-298, 2007.
- [59] N. Kimmel, J. S. Hiraga, R. Hartmann, N. Meidinger, and L. Strüder. The direct measurement of the signal charge behavior in pnCCDs with subpixel resolution. *Nuclear Instruments and Methods in Physics Research A* 568, 128-133, 2006.
- [60] L. Strüder, High-resolution imaging X-ray spectrometers; *Nucl. Instr. Meth.*, 454, 73. 2000.
- [61] P. Lechner. Pair creation energy and Fano factor of silicon in the energy range of soft X-rays. *Nucl. Instr. Meth.*, A377,206-209, 1996.
- [62] N. Meidinger, L. Strüder, P. Holl, H. Soltau, and C. von Zanthier. Analysis of trapping effects on charge transfer in proton irradiated pnCCDs. *Nuclear Instruments and Methods in Physics Research A* 377, 298-311, 1996.
- [63] Van Boxel, S., Schmidt, S., Ludwig, W., Zhang, Y., Sørensen, H. O., Pantleon, W., & Juul Jensen, D. Monitoring grain boundary migration during recrystallisation using topotomography. *Risoe International Symposium on Materials Science. Proceedings*, 31, 449-456, 2010.
- [64] Mika, D. P., & Dawson, P. R., Effects of grain interaction on deformation in polycrystals. *Materials Science and Engineering: A*, 257(1), 62-76, 1998.

- [65] Wang, L., Li, M., Almer, J., Bieler, T., & Barabash, R., Microstructural characterization of polycrystalline materials by synchrotron X-rays. *Frontiers of Materials Science*, 7(2), 156-169, 2013
- [66] A. King, G. Johnson, D. Engelberg, W. Ludwig, and J. Marrow. Observations of intergranular stress corrosion cracking in a grain-mapped polycrystal. *Science*, 321(5887):382–385, 2008
- [67] Send, S., Abboud, A., Wiesner, N., Shokr, M., Klaus, M., Genzel, C., ... & Strüder, L., Application of a pnCCD for energy-dispersive Laue diffraction with ultra-hard X-rays. *Journal of Applied Crystallography*, 49(1), 222-233, 2016.
- [68] Send, S., Abboud, A., Leitenberger, W., Weiss, M. S., Hartmann, R., Strüder, L., & Pietsch, U., Analysis of polycrystallinity in hen egg-white lysozyme using a pnCCD. *Journal of Applied Crystallography*, 45(3), 517-522, 2012.
- [69] Chen, X., Tamura, N., MacDowell, A., & James, R. D., In-situ characterization of highly reversible phase transformation by synchrotron X-ray Laue microdiffraction. *Applied Physics Letters*, 108(21), 211902, 2016.
- [70] Liu, W., & Ice, G. E. X-ray Laue diffraction microscopy in 3D at the Advanced Photon Source. In *Strain And Dislocation Gradients From Diffraction: Spatially-resolved Local Structure And Defects* pp. 53-81, 2014.
- [71] Budai, J. D., Liu, W., Tischler, J. Z., Pan, Z. W., Norton, D. P., Larson, B. C., ... & Ice, G. E. Polychromatic X-ray micro- and nanodiffraction for spatially-resolved structural studies. *Thin Solid Films*, 516(22), 8013-8021, 2008.
- [72]. Andritschke, R., Hartner, G., Hartmann, R., Meidinger, N., & Struder, L. Data analysis for characterizing pnCCDs. In *2008 IEEE Nuclear Science Symposium Conference Record* (pp. 2166-2172). IEEE, 2008.
- [73]. Abboud, A., Kirchlechner, C., Send, S., Micha, J. S., Ulrich, O., Pashniak, N., ... & Pietsch, U. (2014). A new method for polychromatic X-ray μ Laue diffraction on a Cu pillar using an energy-dispersive pn-junction charge-coupled device. *Review of Scientific Instruments*, 85(11), 113901.
- [74] Kirchlechner, C., Keckes, J., Micha, J. S., & Dehm, G. (2011). In Situ μ Laue: Instrumental Setup for the Deformation of Micron Sized Samples. *Advanced Engineering Materials*, 13(8), 837-844.

- [75] Schmid, E., & Boas, W. (1935). Kristallelastizität. In *Kristallplastizität* (pp. 15-24). Springer, Berlin, Heidelberg.
- [76] Barabash, R. I., Ice, G. E., Larson, B. C., & Yang, W. (2002). Local Dislocation Structure from Laue Diffraction. In *From Semiconductors to Proteins: Beyond the Average Structure*(pp. 49-66). Springer, Boston, MA.
- [77] Barabash, R. I., Ice, G. E., Liu, W., & Barabash, O. M. (2009). Polychromatic microdiffraction characterization of defect gradients in severely deformed materials. *Micron*, 40(1), 28-36.
- [78] Maass, R., Van Petegem, S., Grolimund, D., Van Swygenhoven, H., & Uchic, M. D. (2007). A strong micropillar containing a low angle grain boundary. *Applied Physics Letters*, 91(13), 131909.
- [79] Kirchlechner, C., Imrich, P. J., Grosinger, W., Kapp, M. W., Keckes, J., Micha, J. S., ... & Dehm, G. (2012). Expected and unexpected plastic behavior at the micron scale: An in situ μ Laue tensile study. *Acta Materialia*, 60(3), 1252-1258.
- [80] Britton, T. B., & Wilkinson, A. J. (2011). Measurement of residual elastic strain and lattice rotations with high resolution electron backscatter diffraction. *Ultramicroscopy*, 111(8), 1395-1404.
- [81] Meyers, M. A., Mishra, A., & Benson, D. J. (2006). Mechanical properties of nanocrystalline materials. *Progress in materials science*, 51(4), 427-556.
- [82] Ohashi, T., Barabash, R. I., Pang, J. W. L., Ice, G. E., & Barabash, O. M. (2009). X-ray microdiffraction and strain gradient crystal plasticity studies of geometrically necessary dislocations near a Ni bicrystal grain boundary. *International Journal of Plasticity*, 25(5), 920-941.
- [83] Roters, F. (2005). Application of crystal plasticity FEM from single crystal to bulk polycrystal. *Computational materials science*, 32(3-4), 509-517.
- [84] Eisen, Y., & Shor, A. (1998). CdTe and CdZnTe materials for room-temperature X-ray and gamma ray detectors. *Journal of crystal growth*, 184, 1302-1312.

- [85] Del Sordo, S., Abbene, L., Caroli, E., Mancini, A. M., Zappettini, A., & Ubertini, P. (2009). Progress in the development of CdTe and CdZnTe semiconductor radiation detectors for astrophysical and medical applications. *Sensors*, 9(5), 3491-3526.
- [86] Schlosser, D. M., Hartmann, R., Kalok, D., Bechteler, A., Abboud, A., Shokr, M., ... & Strüder, L. (2017). A new spectroscopic imager for X-rays from 0.5 keV to 150 keV combining a pnCCD and a columnar CsI (Tl) scintillator. *Journal of Instrumentation*, 12(04), P04009.
- [87] Valentine, J., Moses, W. W., Derenzo, S. E., Wehe, D. K., & Knoll, G. F. (1992, December). Temperature dependence of CsI (Tl) gamma-ray scintillation decay time constants and emission spectrum. In *Gamma-Ray Detectors* (Vol. 1734, pp. 32-44). International Society for Optics and Photonics.
- [88] Hamamatsu Photonics, PATENT, Japan: 1832818, 3126715, 3566926.
- [89] X-ray Data Booklet; Lawrence Berkeley National Laboratory, 2009.
- [90] H. Reichert, A new X-ray transmission-reflection scheme for the study of deeply buried interfaces using high-energy microbeams; *Physica*, (2003), B, 336, 46–55.
- [91] Brown, P. J., Fox, A. G., Maslen, E. N., O'Keefe, M. A., & Willis, B. T. M. (2006). Intensity of diffracted intensities. *International tables for crystallography*.
- [92] Wilson, A. J. C. (1942). Determination of absolute from relative X-ray intensity data. *Nature*, 150(3796), 152..
- [93] Menon, E. S. K., and A. G. Fox. "On the determination of the Debye-Waller factor and structure factors of NiAl by X-ray powder diffraction." *Acta materialia* 44.6 (1996): 2547-2555.
- [94] Steeple, H. (1952). The crystal structure of the cadmium–magnesium alloy, CdMg. *Acta Crystallographica*, 5(2), 247-249.
- [95] Lange, J. (1995). The Lorentz factor for the Laue technique. *Acta Crystallographica Section A: Foundations of Crystallography*, 51(4), 559-565.
- [96] Helliwell, J. R. (1984). Synchrotron X-radiation protein crystallography: instrumentation, methods and applications. *Reports on Progress in Physics*, 47(11), 1403.

- [97] Cornaby, S., Szebenyi, D. M., Smilgies, D. M., Schuller, D. J., Gillilan, R., Hao, Q., & Bilderback, D. H. (2010). Feasibility of one-shot-per-crystal structure determination using Laue diffraction. *Acta Crystallographica Section D: Biological Crystallography*, 66(1), 2-11.
- [98] Dejoie, C., McCusker, L. B., Baerlocher, C., Kunz, M., & Tamura, N. (2013). Can Laue microdiffraction be used to solve and refine complex inorganic structures?. *Journal of Applied Crystallography*, 46(6), 1805-1816.
- [99] Hofmann, F., Song, X., Abbey, B., Jun, T. S., & Korsunsky, A. M. (2012). High-energy transmission Laue micro-beam X-ray diffraction: a probe for intra-granular lattice orientation and elastic strain in thicker samples. *Journal of synchrotron radiation*, 19(3), 307-318.
- [100] Kraft, P., Bergamaschi, A., Broennimann, C., Dinapoli, R., Eikenberry, E. F., Henrich, B., ... & Schmitt, B. (2009). Performance of single-photon-counting PILATUS detector modules. *Journal of synchrotron radiation*, 16(3), 368-375.
- [101] Medjoubi, K., Thompson, A., Bérrar, J. F., Clemens, J. C., Delpierre, P., Da Silva, P., ... & Hustache, S. (2012). Energy resolution of the CdTe-XPAD detector: calibration and potential for Laue diffraction measurements on protein crystals. *Journal of synchrotron radiation*, 19(3), 323-331.
- [102] Liss, K. D., Bartels, A., Schreyer, A., & Clemens, H. (2003). High-energy X-rays: a tool for advanced bulk investigations in materials science and physics. *Texture, Stress, and Microstructure*, 35(3-4), 219-252.
- [103] Jakoncic, J., Di Michiel, M., Zhong, Z., Honkimaki, V., Jouanneau, Y., & Stojanoff, V. (2006). Anomalous diffraction at ultra-high energy for protein crystallography. *Journal of applied crystallography*, 39(6), 831-841.
- [104] Alghabi, F., Send, S., Schipper, U., Abboud, A., Pashniak, N., Pietsch, U., & Kolb, A. (2014). Fast GPU-based spot extraction for energy-dispersive X-ray Laue diffraction. *Journal of Instrumentation*, 9(11), T11003.
- [105] Send, S., Von Kozierowski, M., Panzner, T., Gorfman, S., Nurdan, K., Walenta, A. H., ... & Strüder, L. (2009). Energy-dispersive Laue diffraction by means of a frame-store pnCCD. *Journal of Applied Crystallography*, 42(6), 1139-1146.
- [106] Hermann Minkowski. ber die positiven quadratischen formen und ber kettenbruchhnliche algorithmen. *Journal fr die Reine und Angewandte Mathematik*, (1891) 107:278-29.

- [107] Delaunay, B. (1933). Neue darstellung der geometrischen kristallographie. *Zeitschrift für Kristallographie-Crystalline Materials*, 84(1-6), 109-149.
- [108] Carl F. Gauss, W.C. Waterhouse, Arthur A. Clarke, J. Brinkhuis, and C. Greiter. *Disquisitiones Arithmeticae*, (1986) *Springer, New York*.
- [109] Tosson, A., Shokr, M., Abboud, A., Bebawy, Y., Algashi, A., Hartmann, R., ... & Pietsch, U. (2019). EDLD-Tool: A real-time GPU-based tool to stream and analyze energy-dispersive Laue diffraction of BIG Data sets collected by a pnCCD. *Journal of Instrumentation*, 14(01), P01008.
- [110] Lindholm, E., Nickolls, J., Oberman, S., & Montrym, J. (2008). NVIDIA Tesla: A unified graphics and computing architecture. *IEEE micro*, 28(2), 39-55.

Acknowledgments

Finally, I would like to thank all my colleagues who contributed to the success of this thesis and all the people who supported me during this time:

- I am grateful to Prof. Dr. Ullrich Pietsch for the guidance through the last years and the permanent encouragement and support of the related research projects.
- I am very thankful to Prof. Dr. Lothar Strüder for the assessment of this thesis and fruitful discussions concerning pnCCD-specific topics.
- I give thanks to Dr. Ali Abboud for his support in all kinds of scientific discussions and technical questions.
- I give thanks to Amir Tosson who spent a lot of long days with me during the beamtimes and the help in the programming issues.
- Many thanks to Dr. Tuba Çonka for her helpful ideas and productive discussions concerning the research projects.
- I would like to acknowledge PNSensor GmbH and in particular Dr. Dieter Schlosser and Robert Hartmann for the establishment of the pnCCD systems and for the support in all kinds of technical questions.
- I am grateful to Prof. Dr. Christoph Genzel and Dr. Manuela Klaus for the experimental assistance at EDDI beamline and many helpful ideas and discussions.
- I would like to express my deepest appreciation to my family and my parents for the never-ending support.

This work was supported by the Bundesministerium für Bildung und Forschung (BMBF) under grant 05KS7PSA and 05K10PSB.